Universidade de Aveiro Departamento de Geociências

Universidade do Porto Faculdade de Ciências

Ano 2016

Omar Benazzouz

Novas ferramentas para imagiologia sísmica 3D de subsuperficie, usando *Nodes*: aplicações na prospecção petrolífera

New tools for subsurface imaging of 3D seismic Node data in hydrocarbon exploration

Universidade de Aveiro Departamento de Geociências

Universidade do Porto Faculdade de Ciências

Ano 2016

Omar Benazzouz

Novas ferramentas para imagiologia sísmica 3D de subsuperficie, usando *Nodes*: aplicações na prospecção petrolífera

New tools for subsurface imaging of 3D seismic Node data in hydrocarbon exploration

Tese apresentada à Universidade de Aveiro para cumprimento dos requisitos necessários à obtenção do grau de Doutor em Geociências, realizada sob a orientação científica do Doutor Luis Menezes Pinheiro, Professor do Departamento de Geociências da Universidade de Aveiro, e do Dr. Daniel Herold, Vice Presidente Executivo da Parallel Geoscience Corporation, USA.

To God be the glory, for great things He has done, to allow me health and prosperity to finish this work.

To my parents, brothers, sisters, and friends. All I have and will accomplish is only possible due to your endless love and support.

o júri

presidente

Prof. António Manuel Melo de Sousa Pereira
professor Catedrático do Departamento de Eletrónica, Telecomunicações e Informática da Universidade de Aveiro.

Prof. Luis Manuel Henriques Marques Matias
professor associado com Agregação do Instituto Geofísico do Infante D. Luiz, Faculdade de Ciências da Universidade de Lisboa.

Prof. Luis Felipe Fuentefria de Menezes Pinheiro - Orientador
professor associado do Departamento de Geociências da Universidade de Aveiro.

Prof. Rui Miguel Marques Moura
professor Auxiliar do Departamento de Geologia, Ambiente e Ordenamento do Território da Faculdade de Ciências da Universidade do Porto.

Prof. Leonardo Azevedo Guerra Raposo Pereira
professor Auxiliar do Departamento de Engenharia Civil, Arquitetura e Georrecursos da Instituto Superior Técnico da Universidade de Lisboa.

Prof. Maria da Conceição Lopes Videira Louro Neves
professora Auxiliar do Departamento de Ciências do Mar e do Ambiente da Faculdade de Ciências e Tecnologia da Universidade de Algarve.

Prof. Alexandra Afilhado
professora Adjunta do Departamento de do Engenharia Civil do Instituto Superior de Engenharia de Lisboa.

Dr. Daniel Herold – Co-orientador (Especialista)
Especialista (Orientador), Executive Vice President and Managing Director of Parallel Geoscience Corporation, USA.

Acknowledgment agradecimentos

The completion of this undertaken could not have been possible without the participation and assistance of so many people whose names may not all be enumerated. Their contributions are sincerely appreciated and gratefully acknowledged.

I extend my deepest gratitude to my supervisors; Prof. Luis Menezes Pinheiro and Mr. Daniel Herold, for the support they extended to me during the course of this thesis. Their dedication and thoroughness is something that has inspired me, and their example will serve me all my life in whatever I do. I greatly appreciate the unwavering time and energy dedicated to aiding my work.

I would like to thank Parallel Geoscience Corporation for funding and supporting this work, and the Marine Geology and Geophysics Laboratory of the Geosciences Department of the University of Aveiro for hosting me during this time.

palavras-chave

Reflexão sísmica 3D, OBS, Node, deriva de relógio, posicionamento por multilateração, modelo de velocidade, ray-tracing, eikonal, imagiologia sísmica, migração, prestack, Kirchhoff.

resumo

A aquisição de dados sísmicos de reflexão multicanal 3D/4D usando Ocean Bottom NODES de 4 componentes constitui atualmente um sector de importância crescente no mercado da aquisição de dados reflexão sísmica marinha na indústria petrolífera. Este tipo de dados permite obter imagens de sub-superfície de alta qualidade, com baixos níveis de ruído, banda larga, boa iluminação azimutal, offsets longos, elevada resolução e aquisição de tanto ondas P como S. A aquisição de dados é altamente repetitiva e portanto ideal para campanhas 4D. No entanto, existem diferenças significativas na geometria de aquisição e amostragem do campo de ondas relativamente aos métodos convencionais com streamers rebocados à superfície, pelo que é necessário desenvolver de novas ferramentas para o processamento deste tipo de dados. Esta tese investiga três aspectos do processamento de dados de OBSs/NODES ainda não totalmente resolvidos de forma satisfatória: a deriva aleatória dos relógios internos, o posicionamento de precisão dos OBSs e a implementação de algoritmos de migração pre-stack 3D em profundidade eficientes para obtenção de imagens precisas de subsuperfície. Foram desenvolvidos novos procedimentos para resolver estas situações, que foram aplicados a dados sintéticos e a dados reais. Foi desenvolvido um novo método para detecção e correcção de deriva aleatória dos relógios internos, usando derivadas de ordem elevada. Foi ainda desenvolvido um novo método de posicionamento de precisão de OBSs usando multilateração e foram criadas ferramentas de interpolação/extrapolação dos modelos de velocidades 3D de forma a cobrirem a extensão total área de aquisição. Foram implementados algoritmos robustos de filtragem para preparar o campo de velocidades para o traçado de raios e minimizar os artefactos na migração Krichhoff pre-stack 3D em profundidade. Os resultados obtidos mostram um melhoramento significativo em todas as situações analisadas. Foi desenvolvido o software necessário para o efeito e criadas soluções computacionais eficientes. As soluções computacionais desenvolvidas foram integradas num software standard de processamento de sísmica (SPW) utilizado na indústria, de forma a criar, conjuntamente com as ferramentas já existentes, um workflow de processamento integrado para dados de OBS/NODES, desde a aquisição e controle de qualidade à produção dos volumes sísmicos migrados pre-stack em profundidade.

keywords

3D Seismic reflection, OBS, Node, clock drift, multilateration positioning, velocity model, ray-tracing, eikonal, seismic imaging, migration, prestack, Kirchhoff.

abstract

Ocean bottom recording of 3D/4D multichannel seismic reflection data using 4 component Nodes is a recent and growing major segment in the marine seismic acquisition market in the oil and gas industry. These data provide high quality subsurface imaging with low ambient noise levels, broad bandwidth, wide azimuth illumination, long-offset, high resolution, and recordings of both P and S waves. In addition, data acquisition is highly repeatable and therefore ideal for 4D surveys. However, there are significant differences in acquisition geometry and wavefield sampling, compared to the conventional towed streamer data, which require new tools to be developed for data processing. This thesis investigates three key issues in OBS/NODE data processing that have not yet been satisfactorily fully solved: random clock drifts, accurate OBS positioning and efficient 3D pre-stack depth migration algorithms for accurate subsurface imaging. New procedures were developed to tackle these issues and these were tested on synthetic and real datasets. A new method for random clock drift was created using high order derivatives to detect and correct these residual drifts. A new accurate OBS/NODE positioning algorithm, using multilateration was developed. Tools were created for interpolation/extrapolation of 3D velocity functions across the full extent of the acquisition survey, and robust smoothing algorithms were used to prepare the velocity field to be used for ray tracing and pre-stack 3D Kirchhoff depth migration, so as to minimize migration artifacts. The results obtained show a clear improvement in all situations analyzed. Dedicated software tools were created and computationally efficient solutions were implemented. These were incorporated into an industry standard seismic processing software package (SPW), so as to provide, together with the already existing tools, a fully integrated processing workflow for OBS/NODE data, from data acquisition and quality control, to the production of the final pre-stack depth migrated seismic volumes.

Table of contents

List of Figures

Chapter 1

Introduction

The seismic acquisition method is based on the analysis of measurements from ground motion and/or water pressure detectors (receivers), which measure and sample the wavefield originating from either passive or active sources. In marine seismic acquisition, the source is generally a towed airgun system. When an airgun is triggered, it releases a tremendous amount of pressurized air creating a seismic wave. The downgoing wavefield propagates through the water column and the subsurface geological layers. At each change of acoustic impedance (product of sound wave velocity by density) between two subsurface layers, part of the wavefield energy reflects and propagates upward to be recorded by the receivers. The receivers are either a surface towed streamer containing multiple hydrophones or Ocean Bottom Seismometers (OBSs). The seismic wavefield is either recorded as source gathers (generally the case with streamer data) or as receiver gathers (generally the case with OBS data). A large number of these records are used to create a highly accurate image of the subsurface through a method called migration.

1.1. Ocean bottom seismometers

The first use of OBSs dates back to the 1930s for geological studies and earthquakes monitoring. An early patent on such method applied to the oil and gas industry stems from Flude, who used bulky waterproofed seismometers, each connected by a cable to the recording device on a vessel (Flude 1942). Although the OBS technology preceded streamer surveying, the use of these recording devices was long restricted to academia due to the limited recording capabilities. In the 1980s, geophones and hydrophones were fitted together into a single unit, which gave birth to the subsea multicomponent technique.

Barr and Sanders introduced in 1989 the concept of upgoing and downgoing wavefield separation by combining these geophone and hydrophone data (Barr and Sanders 1989). The progress of the OBS techniques eventually led to the deployment of permanent Ocean Bottom Cables (OBC) for 4D surveying and reservoir monitoring on the Foinaven Field, west of Shetland, in 1995 (De Kok 2012). Nowadays, OBSs normally used in oil and gas industry exploration surveys usually consist of a three-component geophone, recording ground motion velocity in three perpendicular directions, and a hydrophone recording water pressure.

There are two main types of ocean bottom recording systems (Fig. 1):

1) Ocean Bottom Cables (OBC) in which cables with embedded multicomponent sensors are deployed from a boat using an umbilical connection, with typical inline receiver spacing similar to that of a towed streamer.

2) Ocean Bottom NODES (also often called simply OBSs) in which a number of multicomponent units are deployed individually with typically larger receiver spacing. In this thesis we will use the terms Node and OBS interchangeably when referring to individual units deployed at the seafloor.

OBSs can be either deployed to the seafloor using a remotely operated vehicle (ROV) or dropped from the sea surface and allowed to sink to the seafloor. OBS acquisition tends to be preferred for very deep-water surveys where the cost of cable deployment becomes prohibitive and also in the presence of sea-bottom obstructions such as pipelines and exploitation platforms at production sites.

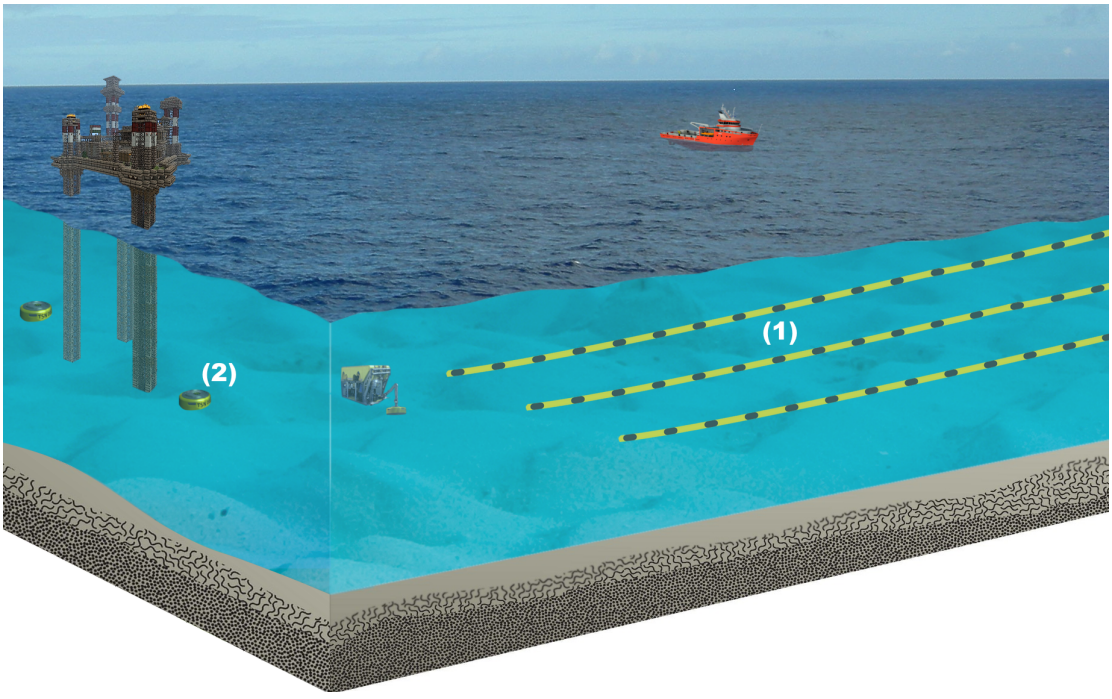

Figure 1 - Two types of ocean bottom recording systems: (1) Ocean Bottom Cables, generally connected to a buoy or directly to the vessel for timing and communications; (2) standalone Ocean Bottom Seismometers.

Multiple highly desirable properties arise from the fact that OBSs are designed to operate on the seafloor:

1) The recording environment in the seafloor is usually much quieter with less ambient noise originating from waves, wind, boats, etc. (at least an order of magnitude lower then noise levels at the sea surface (De Kok 2012), which allows recording of broader bandwidth data with a higher signal to noise (S/N) ratio;

2) The vessel operating the seismic source may move freely without having to tow long streamers. This decoupling of the source and the receivers allows shooting of data with long offset and wide azimuthal illumination providing a true 3D recording geometry (Bouska 2008);

3) With these recording systems, data acquisition may be highly repeatable;

4) The possibility to record pressure and shear wave energy.

Reasons for using such acquisition systems include the following: (1) the presence of surface obstructions, such as operating platforms and rigs in production areas where 4D acquisition is of the utmost importance, which would make streamer acquisition difficult; (2) the need to image deep structures, which is only possible with large offset data; (3) the presence of complex structures such as salt where wide azimuthal illumination is required; (4) very rough sea conditions, such as the case in the North Sea, which makes streamer acquisition very noisy; (5) the need to image under gas clouds, in this case the S waves recorded by the three component geophone provides valuable insight.

Compared to towed streamer surveys, however, the differences in acquisition geometry and wavefield sampling are very significant and therefore new tools for data processing are needed. OBS recordings are a recent development in the oil and gas industry, and many problems related to the acquisition and processing of these data are not yet fully solved. Some of these problems are related to the hardware itself (e.g. time drifts of clocks, efficient coupling), others are related to the survey parameters and/or survey strategy (e.g. receiver positioning, sparse receivers, water velocity), and others are related to the geometry of the acquired data and processing routines and algorithms (e.g. non-hyperbolic moveout, velocity analysis, datuming and migration algorithms).

1.2. OBS versus streamer data acquisition

In conventional multichannel acquisition (Fig. 2b), a boat tows a streamer (2D) or a swath of streamers (3D) at the sea surface, while continuously shooting seismic signal from a towed airgun array at the sea surface. This results in a nearly symmetric raypath from the source to the subsurface point then back to the surface. In OBS surveys however (Fig. 2a), the receivers are deployed to the seafloor, and a boat is shooting seismic signal from a towed airgun at the surface. Especially in deeper water, this results in an asymmetric raypath. As a result, many processing techniques optimized for processing streamer-acquired data (Velocity analysis, NMO, DMO, migration...) cannot handle OBS data. Moreover, because the receivers (OBSs) are now on the seafloor instead of at the sea surface, there is no possible communication with the receivers. This means that until the end of the survey, the recorded data cannot be accessed and thus there is no possible real-time processing or quality control. Also if the OBSs were not deployed by an ROV, their exact positions are unknown.

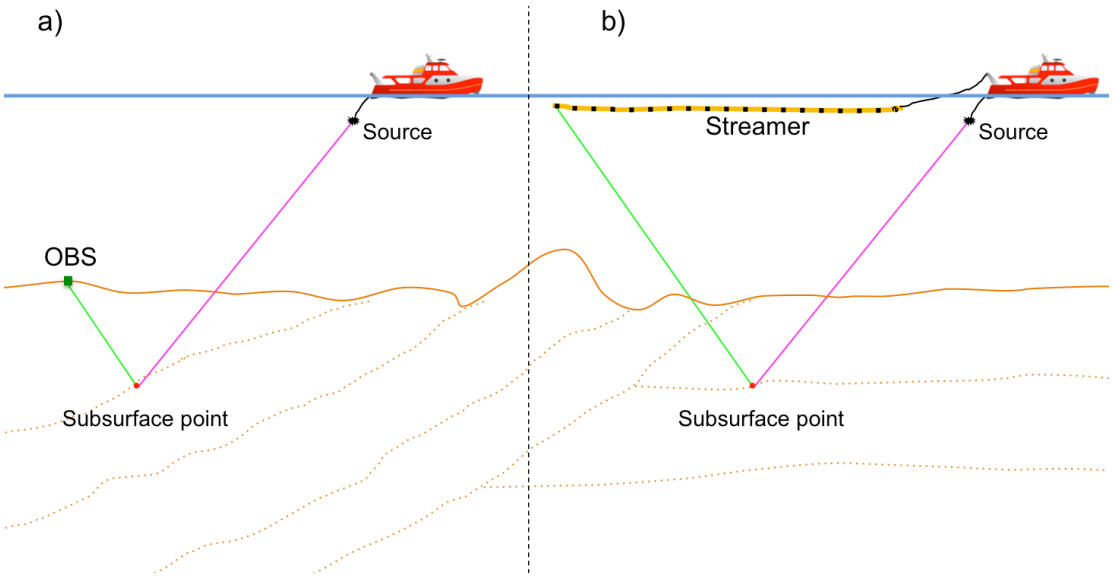

Figure 2 - Comparison of source and receiver positions both towed-streamer versus OBS surveys.

As a consequence of towing the receivers in fixed positions relative to the source, even 3D towed-streamer conventional surveys typically have a narrow source to receiver azimuths (±15°), and the offset range of the data is limited by the length of the streamer(s) (Bouska 2008). Recording wide azimuth data with a towed-streamer is nevertheless achievable though, by either acquiring overlapping surveys in multiple directions, coil shooting, or by

using several shooting boats, however these solutions are relatively expensive (De Kok 2012). On the other hand, OBS 3D acquisition uses stationary receivers with a decoupled mobile source, which inherently allows wide ranges of source to receiver offsets and azimuths. Also, as the most significant cost in OBS acquisition is the receivers, the receiver spacing is usually much larger than the source spacing. Using this acquisition style, the recorded data has to be processed in the receiver domain to avoid spatial aliasing. Each receiver station is therefore usually processed as an independent 3D receiver gather.

1.3. Pre-migration standard seismic processing

Once the seismic data is recorded, a geophysicist uses a sequence of processing steps to eventually construct a faithful image of the earth interior, which normally involves a prestack processing flow. The first steps are the assignment of geometry information to the recorded seismic traces and quality control of the data. The next step is to filter out undesirable noise. Noise may be generated by ocean currents, wind, swell, the vessel's engine, streamer's movement, or other natural and man-made sources. Also, if reflection multiples are not going to be used in later processes, multiples are usually considered as noise and are removed using radon transforms or other multiple modeling and subtraction techniques. Noise may be classified as coherent noise or random noise. Sometimes the noise has a frequency content different from the desired signal (*e.g.* low frequency noise from the streamer), in this case a low cut Band Pass or a Butterworth filters would be used, but if the noise has frequency content within the frequency range of the desired signal such as the case of electrical noise (usually at 50 Hz) a notch filter or other filtering techniques would be used. The F-K filter, utilizing a two-dimensional Fourier transform over time and space, is often used to eliminate coherent noise such as ship noise. There are multiple other types of filters, each designed to remove specific types of noise. The recorded data also needs to be compensated for energy dissipation, which causes loss of signal amplitude. Amplitude recovery processes include among others, spherical correction, gain scaling with time or depth, and automatic gain control. Once the data is filtered and corrected for amplitude, usually a deconvolution is applied, which increases the signal to noise ratio and broadens the frequency bandwidth of the signal thereby improving the vertical resolution. The above processing sequence is a normal basic pre-migration flow; however, depending

on the quality of the data other processes may be applied. Prior to migration, a velocity analysis should be carried out utilizing one of the many existing methods, as an accurate velocity model is essential for good migration results. The next step is migration; a brief description of the different migration algorithms is presented in the next section.

1.4. Seismic migration

Migration is one of the oldest seismic processing techniques, with several pre-digital incarnations; the early graphical implementation date back to the 1920s (Gray et al. 2001). The migration process aims to translate the source/receiver gathers into an image of the subsurface structure by "migrating" the recorded energy to it correct position, taking dip into account. Figure 3 describes the role of migration.

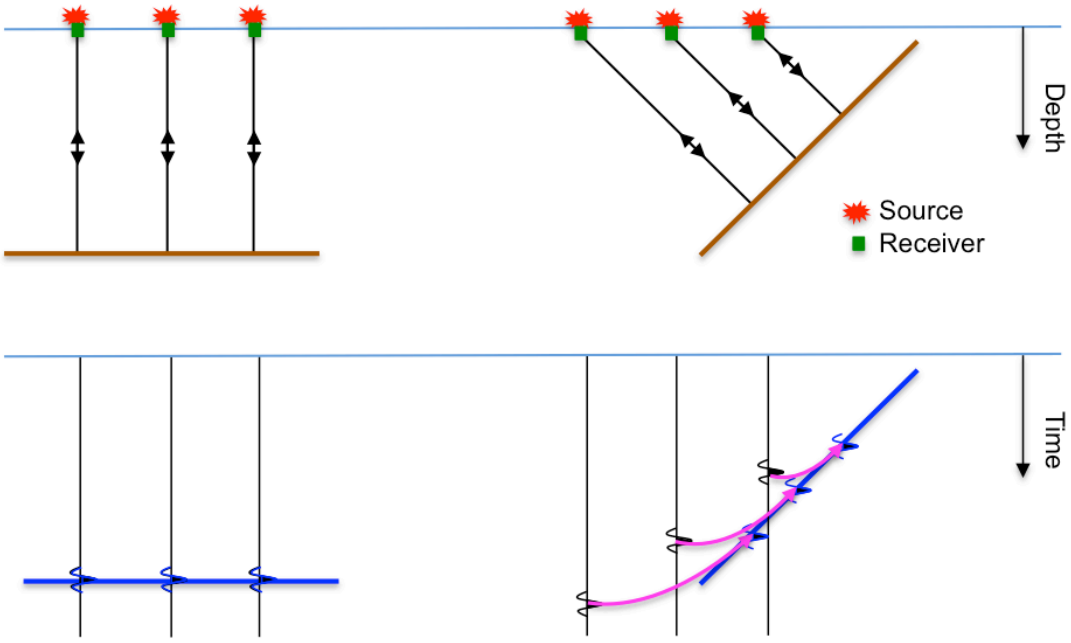

Figure 3 - Illustration of migration concepts with, on top "zero-offset acquisition" with linear and inclined reflectors; on the bottom are the corresponding seismic sections, in black; the migration operation is shown in pink and the migrated sections in blue.

In the above illustration, although not possible in practice, for simplicity coincident source and receiver were used to build a zero-offset section. The migration process (the pink arrow) is shown as an operator, which moves energy in space (between traces) and in time to their true corrected subsurface location. The migration process also altered the dip angle

of the event in the recorded seismic section to match the real reflector position. In early days, the goal of migration was (as shown in Figure 3) to laterally position reflectors accurately enough for drilling exploration wells. Now, migration results go beyond just structural imaging and incorporate velocity and amplitude analysis producing a 3D quantitative model of the subsurface.

Migration methods are divided into three major categories: 1) integral summation also known as Kirchhoff migration; 2) a Fourier-type migration often called F-K migration or Stolt migration; and 3) wave equation migration (Bancroft, 2013). Kirchhoff migration sums energy along diffraction hyperbolas and the summed value becomes the amplitude value at an output location; F-K migration performs a 2D Fourier transform to the data, applies a migration operator in the Fourier domain then performs an inverse Fourier transform to get the resulting migrated seismic section. Wave equation migration uses various solutions to the wave equation to propagate the wavefield upward or downward such as finite-difference, phase shift, or other, leading to the construction of the migrated section. Each migration method has limitations compared to an ideal migration (ability to fully handle variable velocities, maximum properly migrated dip, possibility to attenuate evanescent energy, amplitude preservation, sensitivity to velocity errors, migration noise, etc.) (Robinson et al. 1983) and interestingly, the earth and the structures we want to image are varied enough that, so far, no single migration technique has dominated practical applications (Etgen et al. 2009).

1.5. Scope and Main Objectives of this thesis

Ocean bottom recording of 3D multichannel seismic reflection data is a recent and growing major segment in the marine seismic acquisition market in the oil and gas industry, given the significant improvement in subsurface imaging they can provide. Previously, OBSs were mainly used for 2D refraction and wide-angle reflection studies. Because of the differences in acquisition geometry and wavefield sampling in these recordings compared to the conventional towed streamer data (see Section 1.2), new tools for data processing are needed. In this thesis we analyze some of the current key problems in OBS data processing and focus on the development of new solutions and the adaptation of some of existing ones

to handle issues that are specific to OBS data and have not yet been fully solved. We implement the necessary software to handle these issues and incorporate them into an industry standard software (SPW). We focus essentially on the problems related to OBS clock drifts, accurate OBS positioning and efficient 3D prestack migration for better subsurface imaging. Standard seismic processing steps such as deconvolution, filtering, multi-component rotation, etc. will not be discussed here, as they are common practice.

Specific objectives of this thesis are: 1) to develop and implement a new random clock drift correction algorithm for OBS data, since this is a crucial issue and many times the internal clocks of the OBSs have a random drift that can not be removed with traditional approaches; 2) to develop and implement a new accurate OBS positioning algorithm using solely the recorded seismic energy; 3) to implement an efficient tool for interpolating, extrapolating, and smoothing velocity picks into a regular grid covering all source and receiver positions, to be used for travel-time computation and pre-stack migration; 4) to implement efficient 2D and 3D travel-time computation techniques; and 5) to implement a versatile 2D and 3D Kirchhoff migration scheme that can handle OBS data, but also streamer and land data and make it computationally efficient.

Each of the developed algorithms has been implemented as part of the Seismic Processing Workshop (SPW) software, from Parallel Geoscience Corporation

1.6 Development platform

The algorithms developed in the scope of this thesis are focused on the processing of OBS data, but are not necessary valid only for OBS acquisition (e.g. 2D and 3D travel-times computation, Prestack Time/Depth migrations, etc.). All of these algorithms were translated into a set of tools and processing steps, and were directly implemented in the SPW system, which is the main product of Parallel Geoscience Corporation (PGC) and has been in use commercially and academically since 1988 on all five continents. The current version of the software is written in the low level object-oriented programming language "C++", resulting in very fast code, especially as the code is compiled using the state of the art, highly optimized compiler, Microsoft Visual Studio. The user interface is written using the "Qt" framework. "Qt" is a leading independent technology for cross-platform

development, resulting in high performance native application, which can be built for a variety of operating systems (e.g. Windows, Linux, OS X, 32 or 64 bit version).

The SPW system, in its current version 3.x, is a project-based acquisition quality control and seismic processing software composed of a single interface (Fig. 4), which encompasses tools for Input/Output (IO), Quality Control (QC), Processing, and Visualization.

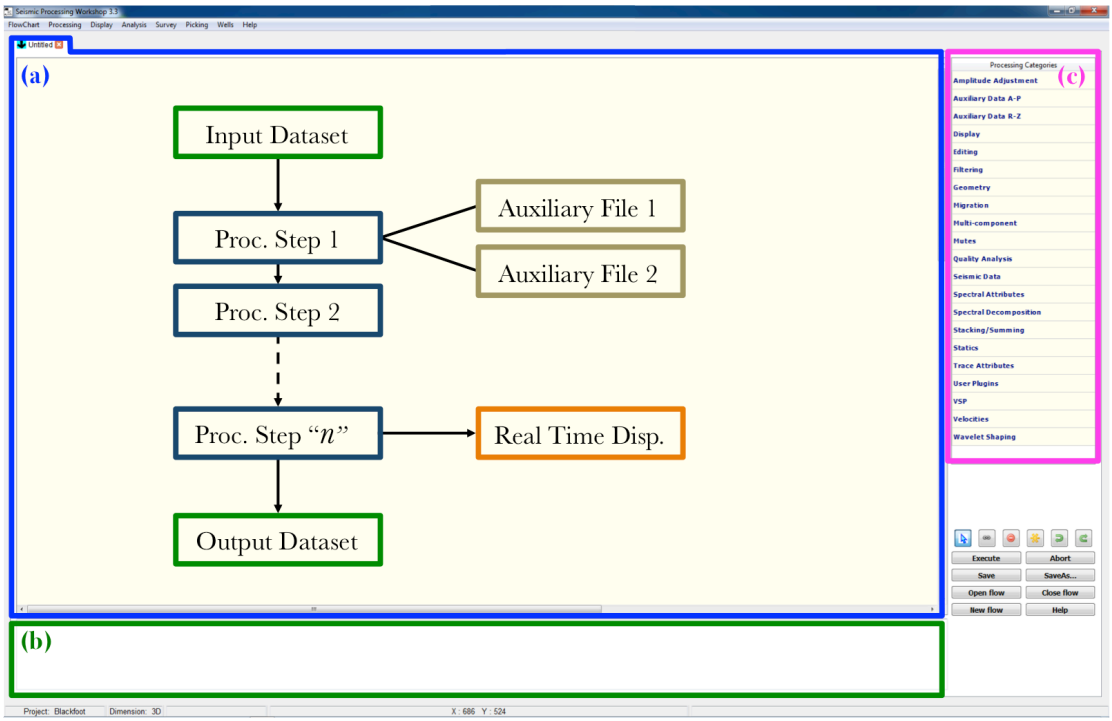

Figure 4 - The main window of the Seismic Processing Workshop (SPW) system. a) The flow area with a typical flow diagram; b) console area; c) processing tool organized by categories - each category contains multiple tools.

In the main window (Fig. 4), the area "a" is the workflow zone. Users may create and open as many workflows as required. Each workflow is built as a piped flowchart, composed of an optional input dataset connected to one or multiple processing steps with or without auxiliary files and an output dataset. IO utilities are mostly built within the input dataset steps. Data may be input from multiple supported file format (tape, SEG-Y, SEG-D, SEG-2, etc.) or using a real time input step, and then proceed to analyzing the file(s) if desired by utilizing one of the available tools (e.g. SEGY Analyzer). These tools allow the users to look at binary dumps of the file, header information in multiple byte-words configurations, sample format, spectral/histogram analysis and many other useful QC tools. Some flows may not need an input dataset, as is the case of a flow for generating synthetic seismograms.

Processing steps may be a simple trace header editor or a more complicated surface consistent deconvolution or 3D prestack migration, all based on the needs of the user. Some of the steps may require auxiliary files. Auxiliary files may be ASCII text datasets (card data) containing geometry information or mute picks or many other data types or may be an auxiliary seismic file containing a wavelet estimate for example. Other steps do not require auxiliary files at all. At the end of each flow is the output dataset, into which the final processed seismic data is written. The area "b" is the console, where messages are generally communicated to the user. These messages can be informative, warnings, or error messages. The area "c" is where all the processing categories are listed; under each category is a list of processing steps. Some of the categories are actually IO related and others are related to visualization and displays.

Visualization tools include a standard seismic data display (Fig. 5), a real time display of seismic data, and attribute map displays (mainly for QC) of geometry, fold coverage, etc.

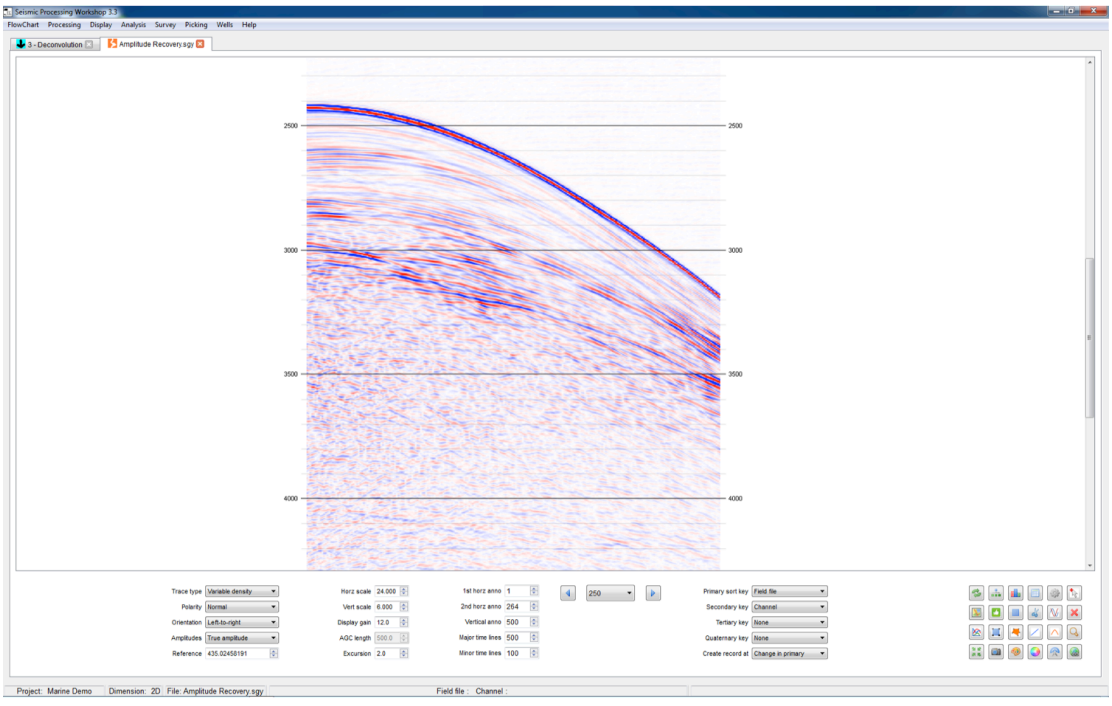

Figure 5 - Standard seismic viewer of SPW displaying a common shot-gather.

The standard seismic display in SPW offers a variety of tools such as spectral analysis, velocity estimate, interactive processing analysis, etc.; it also offers tiled displays with the

capability to synchronize display parameters for comparing multiple seismic data files at various stages of the processing sequence.

Older versions of SPW used to use proprietary seismic format for internal usage. The current version of the software uses instead the standard SEGY file format with an auxiliary "index" file; the index file stores sorting order, header information, and seismic trace byte positions for fast access to the data. Similarly for flowchart and format description files, the current version of the software uses standard XML files instead of proprietary format, making it more transparent to the user. The pick files and the card data files are all column oriented ASCII text format files.

Most of the heavy processing steps are implemented in SPW with parallel computation capabilities in mind. The user can turn on/off the multithreading or cluster processing capabilities, and decide on the number of threads/CPUs to use. These options and others may be configured in the Processing preferences dialogue (Fig. 6).

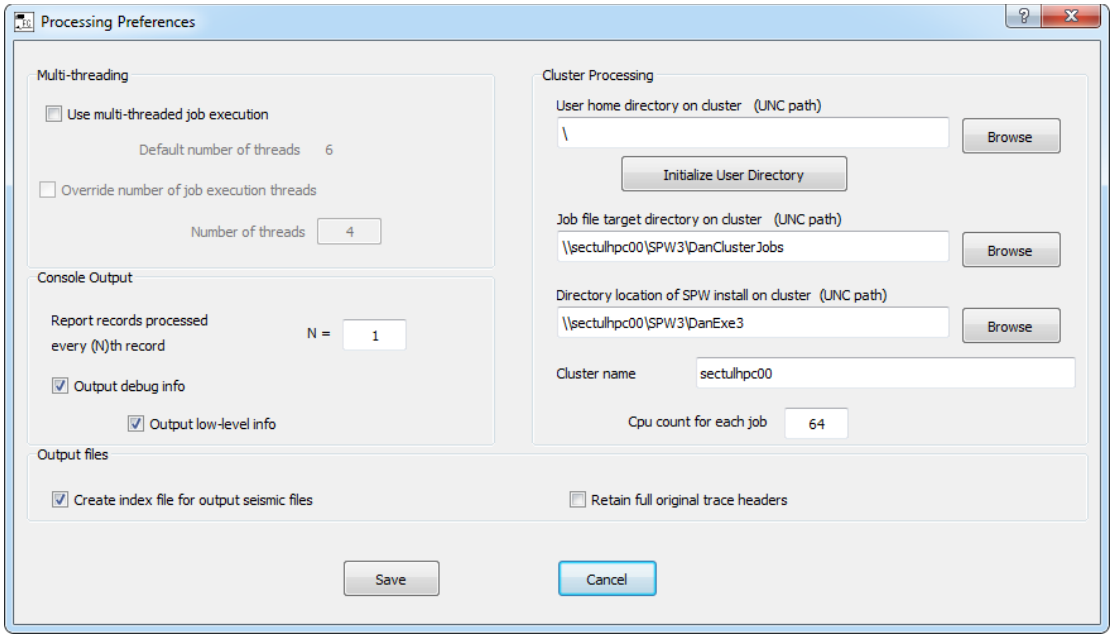

Figure 6 - Processing preferences dialogue of SPW.

Parallel processing in SPW is performed based on gathers or, for stacked data it is based on lines. Each seismic gather is processed using a separate thread or CPU. The input and output are managed by the main thread. Basing the multithreading capabilities on gathers and lines rather than traces ensures a larger number of processing steps may benefit from

parallelization; it also makes the parallelization more consistent between all steps and easier for maintenance.

1.7. Outline of the thesis

Chapter two of the thesis starts with a brief review of the seismic data representation and the different seismic gathers, followed by two sections, one concerning Kirchhoff time migration and the other concerning Kirchhoff depth migration. Chapter three tackles the problems of random clock drift and related artifacts. A simple method to remove those artifacts is presented. Chapter four discusses accuracy and cost of different methods for the positioning of the OBSs and how erroneous positioning may affect data quality. A positioning method developed within the scope of this thesis is described using synthetic and field data examples. Chapter five is dedicated to the migration of OBS data; the method of choice here is Kirchhoff Pre-Stack Depth Migration. Chapter six presents the main conclusions of the thesis and a complete workflow for the processing of field OBS data, followed by suggestions for future work.

Chapter 2

Kirchhoff pre-stack migration: An overview

Before going into the details of the migration techniques, we first briefly explore the basic concepts of seismic data representation. In typical marine acquisition surveys (Fig. 2) as the source fires, the pressure is recorded at each receiver location and a trace is associated with each source and receiver point. The midpoint between each source and each receiver is called a Common Mid-Point (CMP). Assuming a horizontally layered geology, all reflections at a given event on a CMP gather come from the same depth point (CDP). The relationships between the common source, common receiver and common mid-point gathers are shown in Figure 7.

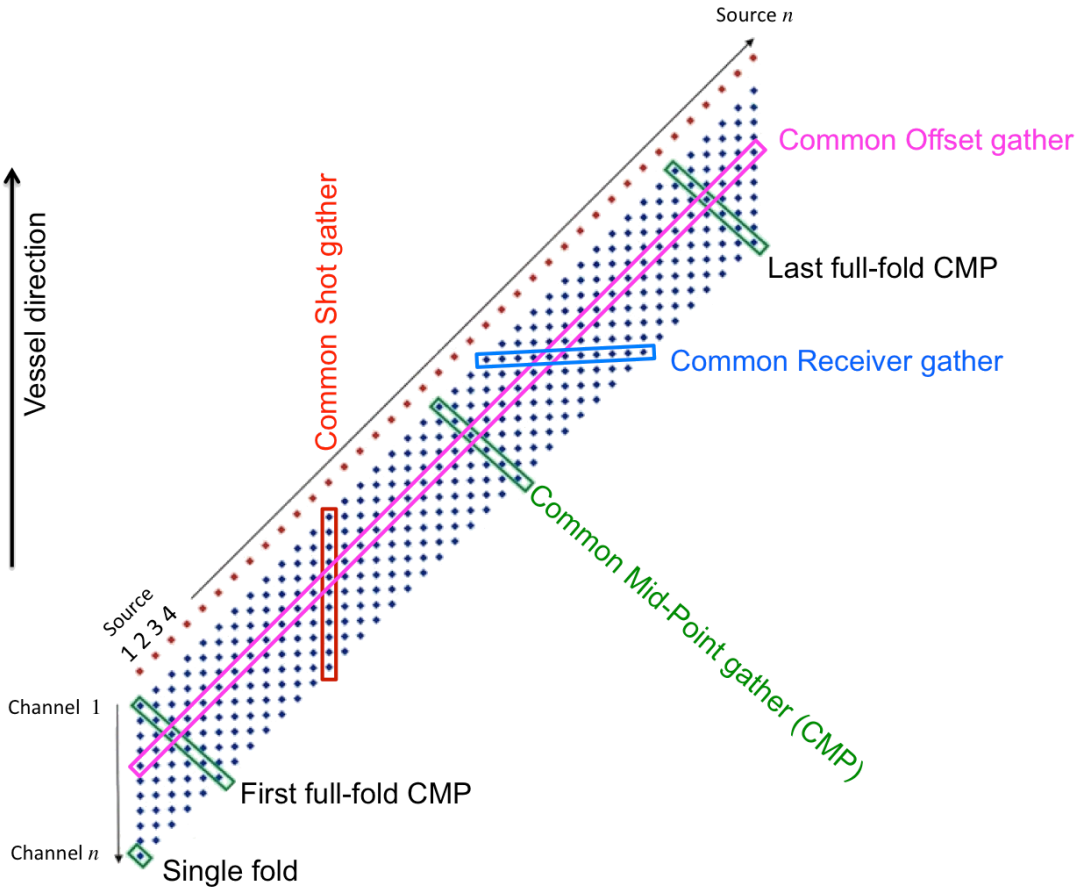

Figure 7- Relationships between source, receiver, offset, and common midpoint gathers for a typical marine survey.

For a Post-Stack Migration processing workflow, the normal process would be to perform a Normal Moveout Correction (NMO) with an appropriate velocity function, to correct for the time difference with offset of the reflections between the CMP traces, caused by the increasing pathways for increasing offsets, followed by the summation (stacking) of all traces

in each CMP gather; in this case the migration is only done after the stacking, thus the name "Post-Stack Migration". In the case of a flat reflector (Fig. 8A), the CMP gather has traces with reflections coming from the same subsurface point. In Figure 8C and 8D, the NMO correction correctly compensated for the offset differences and moved the reflections to the correct temporal position for stacking. However, in the case of complex geology with dipping events, the post-stack migration approach smears energy over the dipping event and fails to migrate the recorded energy to the correct position (Fig. 8B). Reflections coming from two different subsurface locations appear at the same CMP location only at different times. This smearing of energy along the dipping reflectors limits the post-stack processing. In order to correctly handle such complex geology, it is required to use a pre-stack migration workflow for the data. As one of the primary reasons to use OBS technology is the imaging of complex geology (salt, heavily faulted and folded reservoirs, etc.) this thesis will only be concerned with pre-stack migration processing.

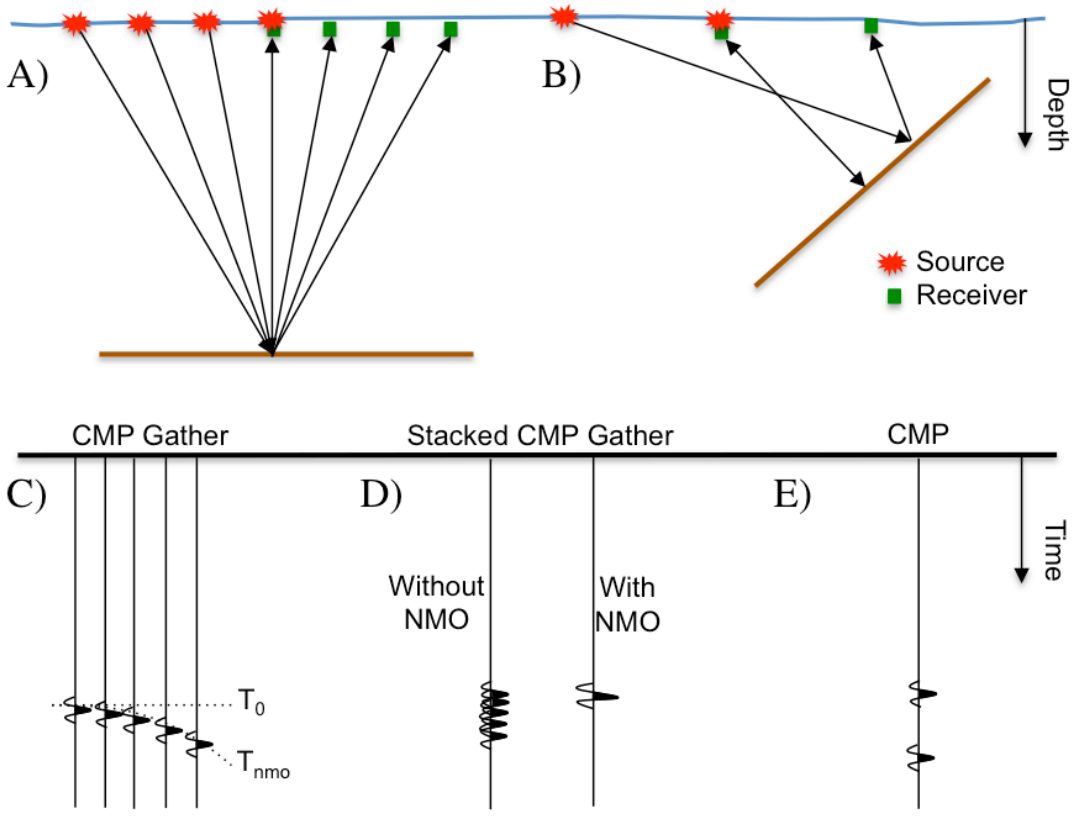

Figure 8 - Sketch of ray path for a CMP gather with: A) a linear reflector; B) a dipping reflector; C) and D) are the corresponding CMP gathers before and after stack, without and with NMO correction. E) Illustrates events from two different locations on the dipping reflector in B) that show in the same CMP trace because in this stacking process dip is not taken into account (modified from Bancroft 2013).

2.1. Kirchhoff pre-stack time migration

Kirchhoff migration descends from one of the oldest methods of migration: the diffraction stack. This method is based on the Kirchhoff integral solution used in optics. Schneider (1978) showed that the diffraction sum method is an asymptotically correct solution to the wave equation if appropriate scaling and filtering are included. The Kirchhoff method views the subsurface as multiple adjacent scatter points, calculates the diffraction surface at each one of these scatter points (also called imaging points), and then carries out a weighted summation over the diffraction surface. It is defined mathematically by the following integral:

$$I(x,t) = \int_A W(x,h,t)\, U(x,h,t)\, dh \Big|_{t=T_D(x,h,t,v)} \qquad (2.1)$$

Where $I(x, t)$ is the value assigned to the imaging point given by the parameters x, and t, which are respectively lateral displacement, and time. $U(x, h, t)$ represent the seismic data, and $W(x, h, t)$ is a true-amplitude weighting function; h in this expressions is the diffraction offset. The weighting function is included for true amplitude migration. For purely kinematic migration, it is excluded from the migration algorithm. The stacking curve or stacking surface is given by $t = T_D(x, h, t, v)$ where v is the RMS velocity.

Kirchhoff migration can easily be expressed for two-dimensional as well as three-dimensional data. For simplicity, let us first examine time migration for a 2D case $U(x, t)$. The first step is to sort the data with regards to offset, which adds another dimension to the input data creating a three-dimensional pre-stack volume $U(x, h, t)$ as shown in Figure 9; then for each imaging point (given here by X_m and t_0) compute the diffraction surface, over which the kernel will perform the weighed sum.

Let x_s, x_r, and x_m be the source, receiver and migrated trace lateral coordinates, respectively, in Figure 9; t_0 is the two-way time (TWT) at the imaging point, and v is the migration velocity. The diffraction time is given by the time the wave takes to propagate from the source to the imaging point and back to each receiver and can be expressed as:

$$T_D = \sqrt{\left(\frac{t_0^2}{4} + \frac{(x_s - x_m)^2}{v^2}\right)} + \sqrt{\left(\frac{t_0^2}{4} + \frac{(x_r - x_m)^2}{v^2}\right)} = \sqrt{\left(\frac{t_0^2}{4} + \frac{{h_s}^2}{v^2}\right)} + \sqrt{\left(\frac{t_0^2}{4} + \frac{{h_r}^2}{v^2}\right)} \qquad (2.2)$$

The above equation is often referred to as the Double Square Root Equation or simply the DSR, where the first square root computes the time from source to imaging point T_s and the second computes the time from the imaging point to the receiver T_r.

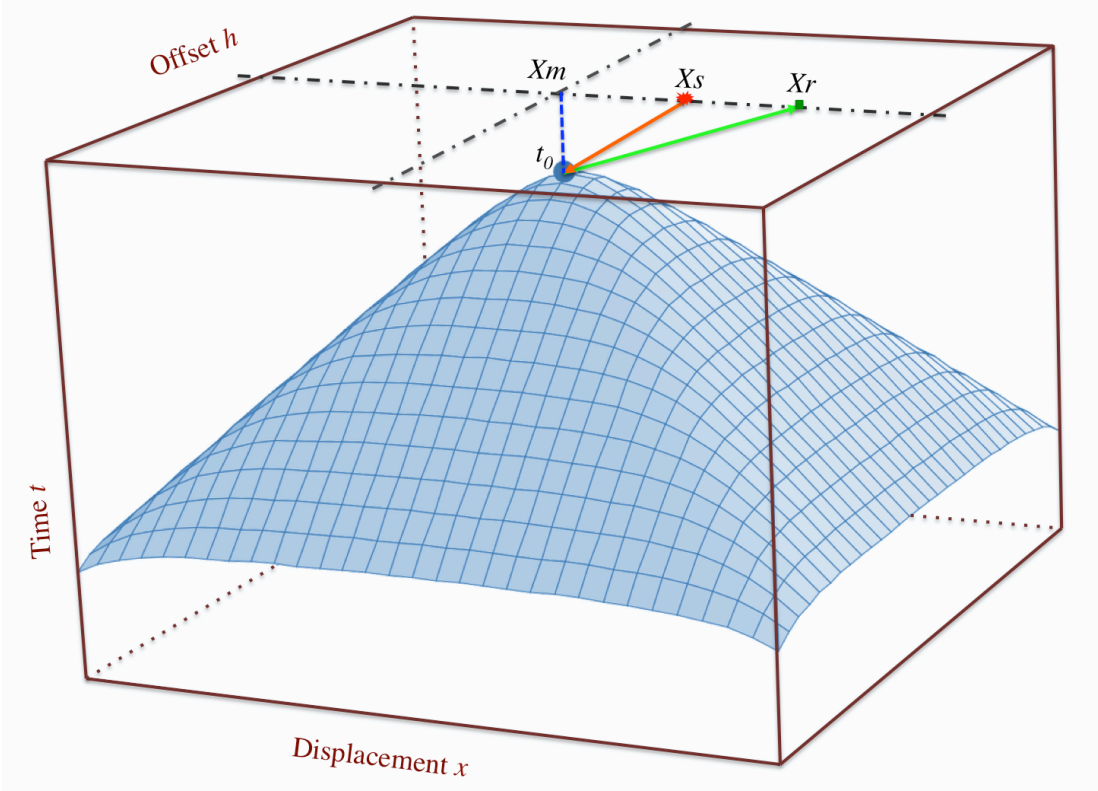

Figure 9 - Illustration of the summation surface in the pre-stack volume for 2D Kirchhoff pre-stack migration. x_s, x_r, and x_m are the source, receiver and migrated trace lateral coordinates, respectively, and t_0 is the two-way time (TWT) at the imaging point (modified from Bancroft 2013).

For the 3D case the same equation holds valid; we simply need to include the "*y*" coordinates in the computation of the terms h_s and h_r as follows:

$$h_s^{\,2} = (x_s - x_m)^2 + (y_s - y_m)^2 \quad and \quad h_r^{\,2} = (x_r - x_m)^2 + (y_r - y_m)^2 \qquad (2.3)$$

In this case the pre-stack volume is four-dimensional *U(x, y, h, t)* and cannot be visualized as in the 2D case.

The input data is the full pre-stack volume and all input traces will be summed into all migrated traces, and this is computationally very expensive. In order to reduce the computation cost related to this approach, source records or constant offset sections may

be used as input data, in which case for each imaging point, the Kirchhoff kernel will have to scan only the traces within the given source gather or zero offset section, thereby reducing significantly the computation cost. Figure 10 illustrates the construction of the diffraction hyperbola for a source gather. For the common offset section, it is exactly the same principle; however, in three-dimensional surveys, especially on land, it is often very difficult to construct common offset sections due to obstacles and acquisition geometries causing highly variable offsets. Notice that a change in the relative position of the source will alter the vertical position of the diffraction. The diffraction shape however is entirely due to the travel-time of rays from the scattering point to the receivers.

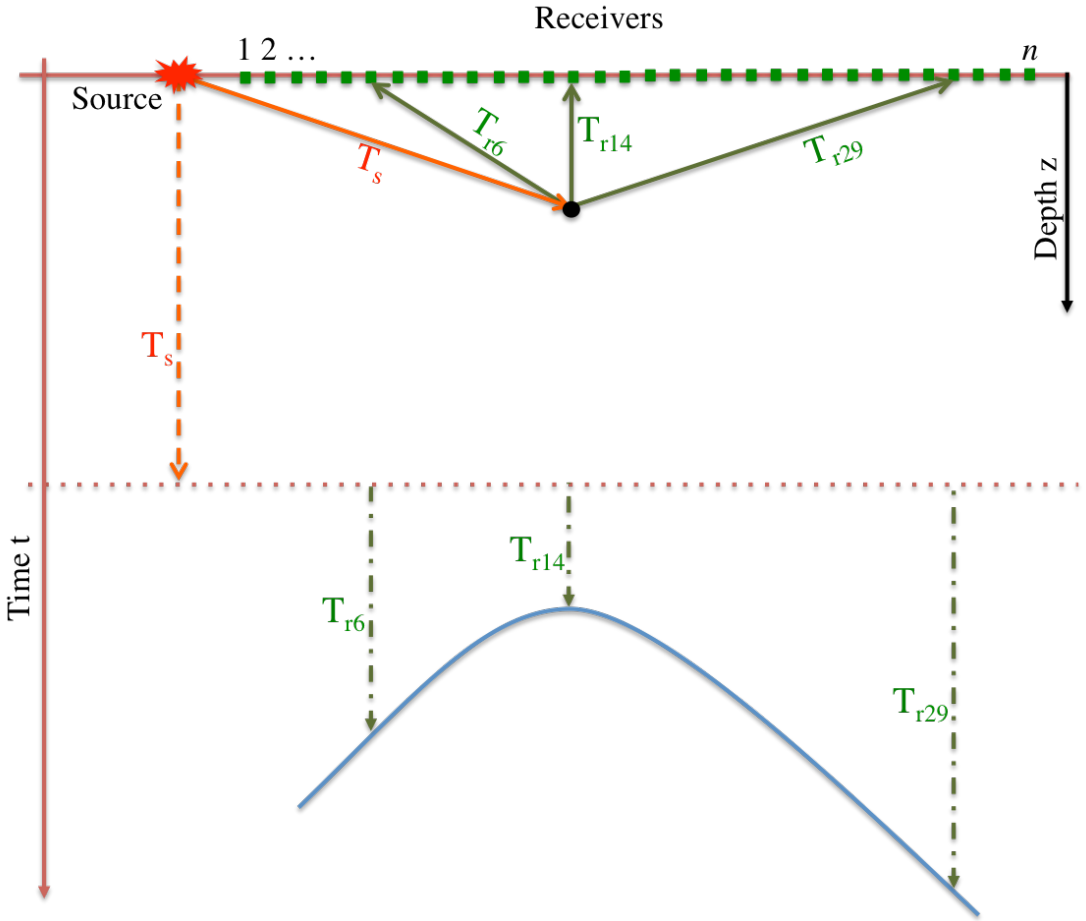

Figure 10 - Sketch of a scattering point on a source gather and it diffraction hyperbola. Ts represent the time from the source to the imaging point, and Tr is the time from the imaging point to the receiver. Notice the scattering point is in depth and the diffraction is in two-way time domain.

Limiting the diffraction aperture and/or setting a maximum diffraction offset acts as a dip-limiting filter (limiting the maximum geological dip to be imaged) (Bancroft, 2013) and can

further decrease the computation time. In the case shown in Figure 11, the Kirchhoff integral will only sum energy in the overlapping area of the pink triangle and the green box.

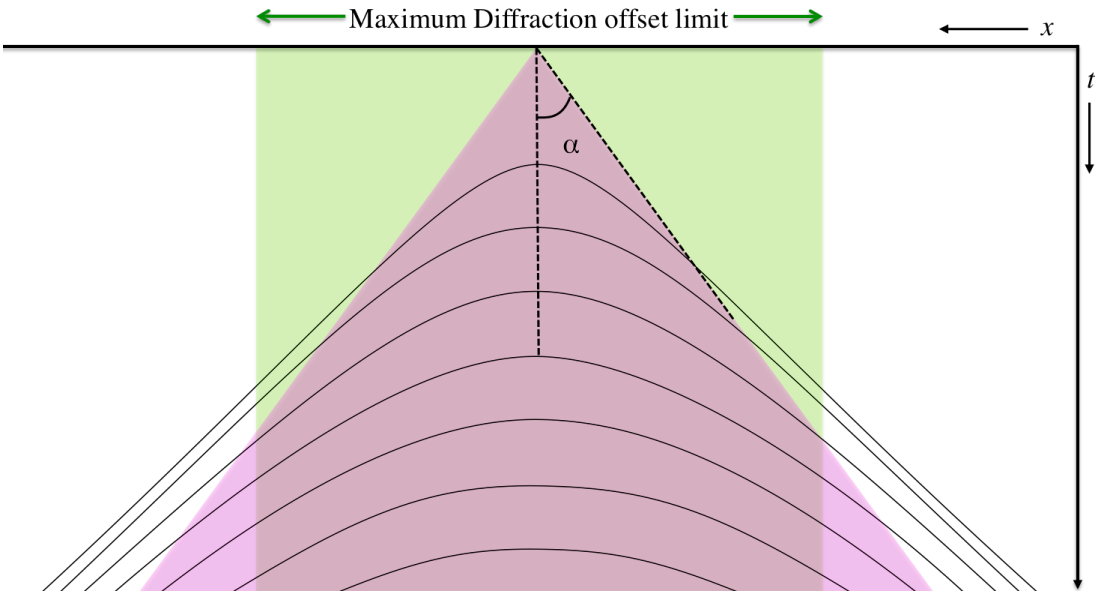

Figure 11 - Family of constant velocity diffraction hyperbolas. Maximum offset limit is shown in green and maximum dip limit is shown in pink.

The Kirchhoff diffraction curve usually intersects input traces in between time samples; therefore interpolation of sample amplitudes is required. With low frequency data, a linear interpolation method might be sufficient, but in order to preserve the high frequency content of the seismic signal, a quadratic or *sinx/x* interpolation method should to be used; otherwise the migrated trace will suffer from aliasing and broadband noise (Bancroft, 2013).

Figure 12 shows an example of marine seismic data to highlight the imaging advantages of pre-stack time migration over the post-stack migration procedure. The diffraction times used by the pre-stack Kirchhoff migration code were implemented using the equation (2.2). The same amplitude scale and velocity functions were used to generate all three sections shown in Figure 12. Different velocity functions would have led to slightly different results. The diffraction hyperbolas are mostly collapsed by the post-stack migration (Fig. 12b) and in multiple areas were over migrated. However, the over migration here does not necessary mean the estimated velocity is too high: it is rather related to a complex velocity structure that could not be resolved with the post-stack procedure. The migration smiles in this case result mostly from a smearing of energy over dipping events. The pre-stack migration (Fig.

12c) delivered a higher quality image and succeeded at resolving dipping conflict in areas where the post-stack migration could not. Most of the migration smiles are actually an artifact of either faulting or other steep events.

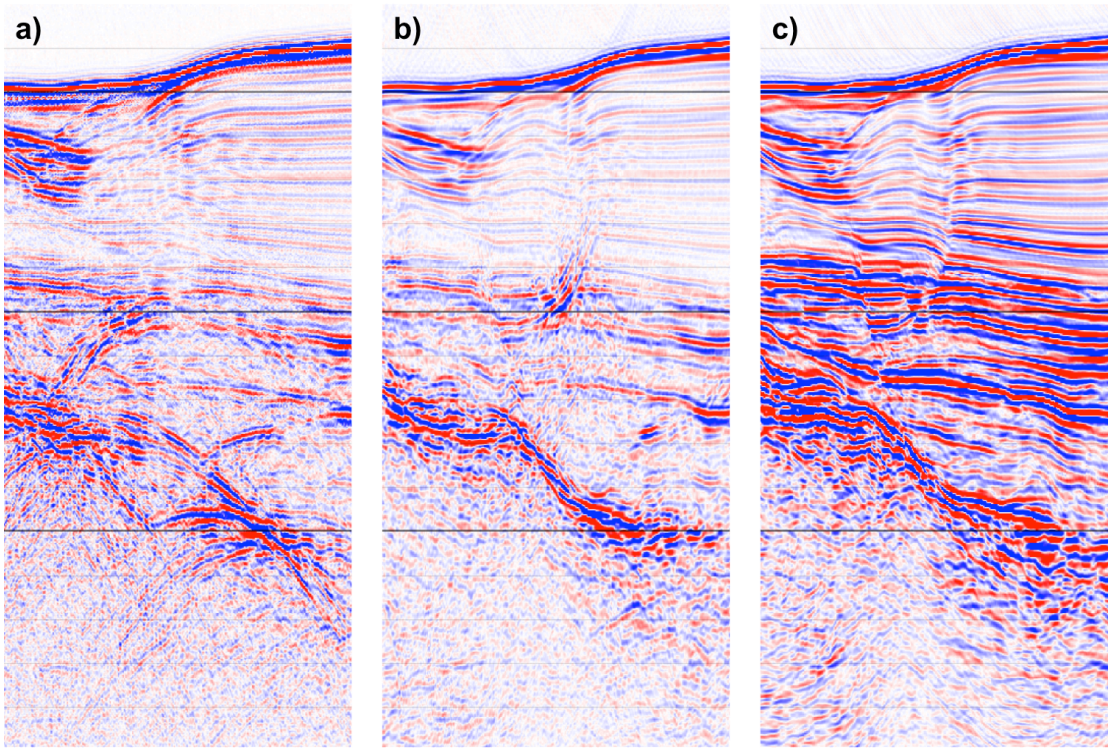

Figure 12 - Marine seismic section. a) Stacked section, b) post-stack migrated, and c) pre-stack migrated. All three sections are in time domain and the migrations were performed with the same velocity model.

Until here, we have discussed pre-stack Kirchhoff migration where the time for the seismic wave to propagate from the source to the imaging point and back to the receivers was calculated based on the source, receiver, and migrated trace positions, the recorded TWT, and the estimated velocity as shown in equation (2.2). This assumes the wave is propagating on a straight path at a certain velocity referred to as the migration velocity. Assuming these migration velocities are in fact RMS velocities, and using the Dix equation to convert them to interval velocities will often result in physically impossible values of velocities (Gray et al. 2001). The seismic wave in reality does not travel in a straight path, and does not propagate from source/receiver to the imaging point with the constant migration velocity at a given point; instead it propagates through a three-dimensional velocity field and bends with every change in the velocity of the medium due to refraction. In order to correctly handle ray bending, it is necessary to use a pre-stack depth migration algorithm.

2.2. Kirchhoff pre-stack depth migration

The distinction between time and depth migrations can be vague (Gray et al. 2001). Some consider *v(z)* migrations, which honor ray bending due to vertical velocity changes, such as phase-shift as time migrations (Gazdag 1978). Others consider time migration followed by image-ray conversion as depth migration processes (Lamer et al. 1981). For the purpose of this thesis, we take the view that the difference between time and depth migration is that the first uses an approximation of the ray path to calculate diffraction times, without honoring ray bending due to velocity changes, whereas the second uses a ray tracing method, or solves the wave equation, to accurately simulate the ray path taking into consideration vertical and lateral velocity changes. For many people, however the most apparent difference between time and depth migrations is the domain of the output migrated section: time migrated sections are in two-way time whereas depth migrated sections are in depth.

Pre-stack depth migration is considered by many to be the most glamorous step of seismic processing, because it transforms mere data into an image that we consider a highly accurate structural description of the subsurface. Pre-stack depth migration uses a ray-tracing algorithm (*e.g.* paraxial, finite difference, or other) to propagate the seismic wave within the interval velocity field, from the source location to the imaging point and back to the receiver. This produces a highly accurate estimation of the diffraction surfaces, which will eventually be used by the migration kernel. The interval velocity field used by this process is the average of the actual earth velocities over some characteristic distance (wavelength, user-defined step, or other). Some ray tracing algorithms only compute arrival times and in this case amplitude weights are computed separately; other algorithms compute amplitude weights during propagation of the seismic wave, thereby better preserving the true amplitude content of the final image.

Kirchhoff pre-stack depth migration is practically a ray-based migration, and because rays represent an asymptotic solution to the wave equation, many are tempted to accuse it of being less accurate than wave-equation migration methods, but this is not necessarily correct. Wave equation migrations can be superior to most ray-based methods only within their range of applicability, which might be quite limited (Etgen et al. 2009). We can only expect a wave equation migration to be superior to any ray based migration if the structural-

imaging situation is modeled well by the wave equation method; for example, one-way wave equation migration does not model overturned events (Etgen et al. 2009) but many ray-based migrations will image overturned events. Also for wave equation migrations, the source and receiver wavefields to be continued must be sampled spatially with the same spacing as the traces in the image (which is not always the case due to field conditions); this is why pre-migration data regularization is required, but even with sophisticated interpolators (FX or Radon interpolators) large gaps between shots and/or receivers are always problematic. This is not the case with the Kirchhoff integral solution because the sum is only performed over existing traces, and irregularly sampled data is inherently handled. Moreover, if the dataset does not refer to a flat datum, Kirchhoff migration can be performed directly from topography, which can be advantageous as opposed to first applying re-datuming (Gray and Marfurt 1995).

The integral in Kirchhoff depth migration can be limited (just like in time migration) by setting maximum diffraction dip and offset ranges for summation. However since depth migration uses ray tracing to calculate travel-times, more flexibility is offered in this respect. Ray tracing can be restricted to include a desired range of takeoff and emergence angles at the recording surface or propagation angles in the subsurface. Also, if ray angles are tracked through the subsurface, they can be used to estimate quantities such as subsurface opening angles or the geologic dip imaged by a particular trace (Xu et al. 2001). Another advantage of ray tracing is the capability to do illumination studies and be able to modify acquisition to provide imaging of all areas of interest in the subsurface.

Figure 13 shows a comparison of Kirchhoff post-stack depth migration versus Kirchhoff pre-stack time migration and illustrates some of the differences. The velocity field used for this example was built using an RMS time velocity analysis method; therefore it is more advantageous for the time migration. For the depth migration it was converted to a depth interval velocity model using the Dix equation. Although the velocity field used in this experience is more appropriate for the time migration, the depth migration still gave superior results, particularly for imaging steeply dipping events and small structures.

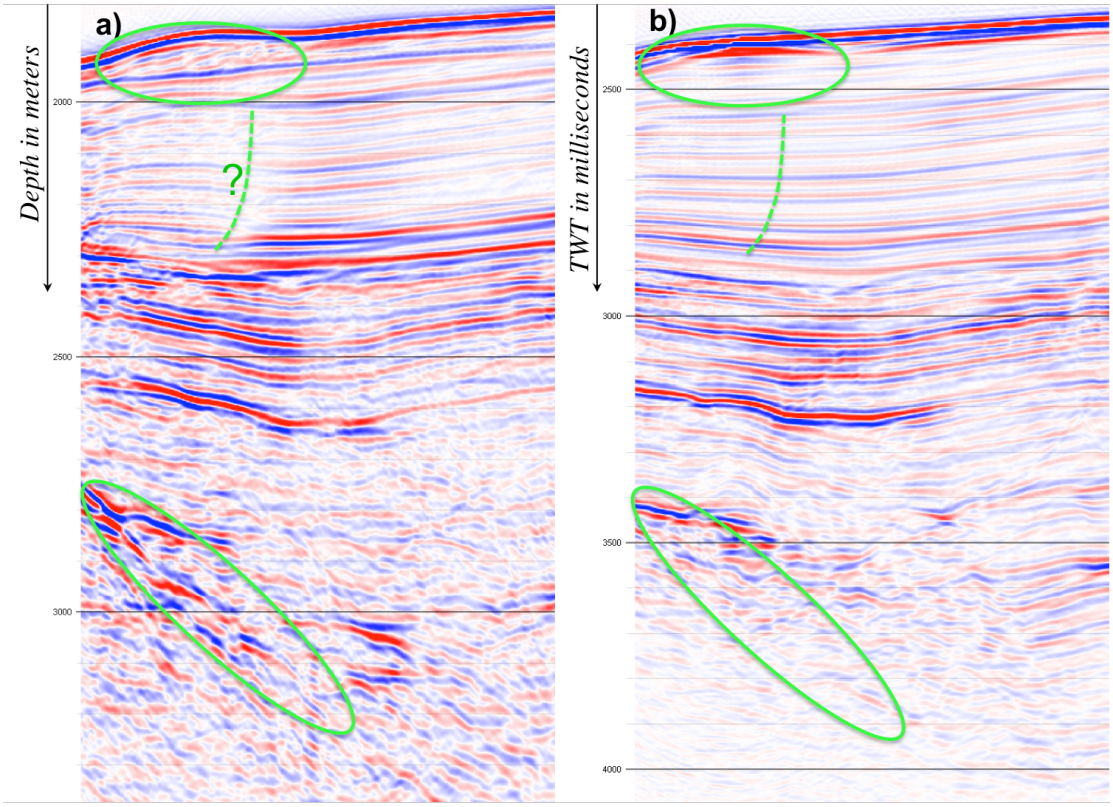

Figure 13 - Marine seismic profile. a) Pre-stack depth migrated, and b) post-stack time migrated.

A lot of differences can be noticed, the first being the shape of the sea bottom where the time migration smoothed it completely and erased the small bump. In the shallow part, a small progradation-like feature (highlighted with a green circle) is very well imaged in the depth migration but practically absent in the time migration; the strait ray approximation completely smeared the energy of those small events. Also, in the shallow part, a potential fault (dashed line) has been completely erased from the time migration but not from the depth migration. The imaging of this fault, even in the depth migration section is not conclusive, but it is very likely to be a small fault just within the lateral resolution allowed by the system geometry. In the deeper part, the steep event (green circle) was completely not resolved with the time migration, while again the depth migration did a decent job imaging it.

There are other small differences here and there. Sometimes, especially in this case, they might be advantageous to the time migration because of the used velocity model. But overall the imaging delivered by the depth migration is more accurate even in this case.

Interval velocity analysis would have delivered even higher quality imaging, particularly for the deeper part of the section.

Chapter 3

OBS clock drift correction

Note: this chapter was published as an extended abstract and presented at the 85th SEG annual meeting (2015) in New Orleans under the title:

Correction of Ocean-Bottom Seismometers random clock drift artifacts

Omar Benazzouz* and Luis Pinheiro, Universidade de Aveiro.
Daniel Herold, Parallel Geoscience Corporation.

3.1. Introduction

In conventional seismic acquisition (streamer acquisition), the recording system uses high precision timing from Global Positioning System (GPS) signal to sample the recorded data; OBS systems, however, are (as discussed in chapter 1.1) autonomous devices that record data continuously during deployment, with time gauged by their own independent clocks. These clocks are based on crystal oscillators units and suffer from random drifts. The clock drift depends mainly on the drift of the crystal oscillator output frequency with changes of environmental conditions (Panahi Shariat et al. 2006; Panahi Shariat et al. 2009). These environmental parameters include temperature, humidity, pressure, acceleration effects, electric and magnetic fields, ionization and radiation effects, aging, warm-up and retrace. To minimize the effect of this clock drift on the sampling process, each instrument's clock is synchronized to GPS time prior to deployment. The time differential between the OBS internal clock and the GPS time measured immediately after recovery is used to remove a linear drift from the dataset (Mànuel et al. 2012), but a significant non linear "random" component of the drift remain in the dataset (Gardner and Collins 2012; Gouédard et al. 2014).

Figure 14 illustrates a receiver gather (OBS record) only corrected for the linear component of the clock drift; multiple traces however are still suffering a significant residual clock drift. The seismic wavefield in this data propagated through the subsurface and back, and it was correctly sensed by the OBS. The problem occurs when associating a value of arrival time to the recorded energy. In order to correctly process this data, traces exhibiting clock drift should be either killed (thus sacrificing valuable data) or time corrected; otherwise they are only generating noise and thereby degrading the data quality.

In this chapter, a new method to eliminate this residual clock drift effect on the recorded seismic data, developed in the scope of this thesis, is presented. Normally these data traces would have to be detected and removed, thereby losing valuable information. The new residual correction methodology allows recovery of these data. The proposed methodology was tested and verified using both synthetic and field data examples.

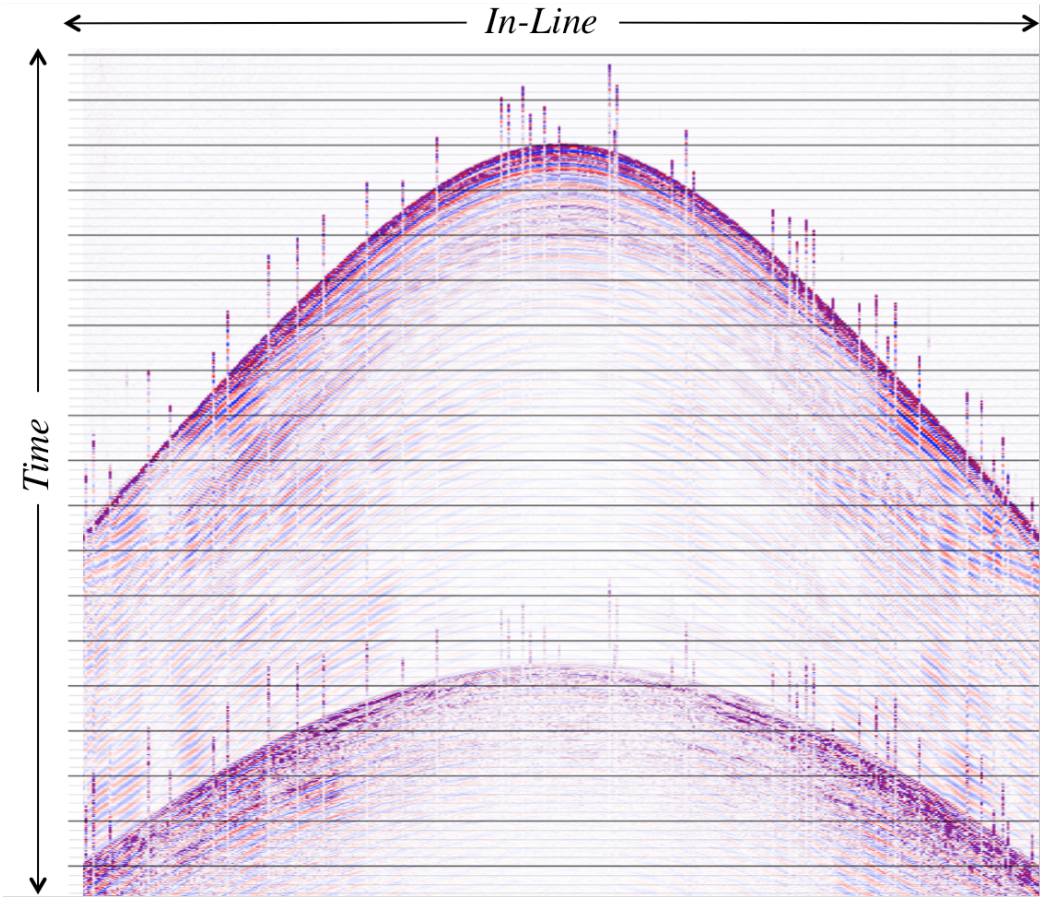

Figure 14 - OBS seismic data highlighting the residual clock drift effect.

3.2. Developed method

In this work, we address the clock drift problem as a simple static shift problem; we compute and apply a static shift required for each trace to shift it back to its correct position in time. The proposed methodology consists of the following steps: (1) we start by picking the first arrivals; automatic first arrivals pickers may be used for this purpose; depending on the quality of the data and the accuracy of the automatic picker, manually checking and editing of the picks may be required; (2) the first arrivals picks are used by the algorithm to identify shifted traces and compute the time shift associated with each trace; (3) these time shifts are then applied to the dataset as trace static shifts.

In order to identify the traces suffering the clock drift (bad traces), we compute the derivative of the first arrival times with respect to shot intervals; bad traces, in contrast to the good ones, will generate larger derivative values because of the jump in the value of arrival

time. To enhance the large derivative values even further, a nonlinear operator is used; in this work we chose to raise the derivatives to a large power (6th power). This value is then stored, and will be referred to as enhanced derivative (ED). A threshold value roughly estimating the percentage of "good traces" versus "bad traces" is then set by the user; for the example shown in Figure 15 the default value of 75%, was used, which means that 25% of the traces or less, are exhibiting clock drift. The user can also define, if wanted, a maximum value of shift to be allowed. The algorithm flags the traces with the lowest ED as good and those with the largest ED as bad, using the threshold parameter. If the user sets a value of shift to be allowed, a second check is performed, to only allow shifts smaller than or equal to the maximum allowed shift value. Figure 15 shows an example of a synthetic first break picks of 40 traces, with traces 10,11,12, and 15 showing a clock drift of about 100 milliseconds each, and the ED associated to each trace.

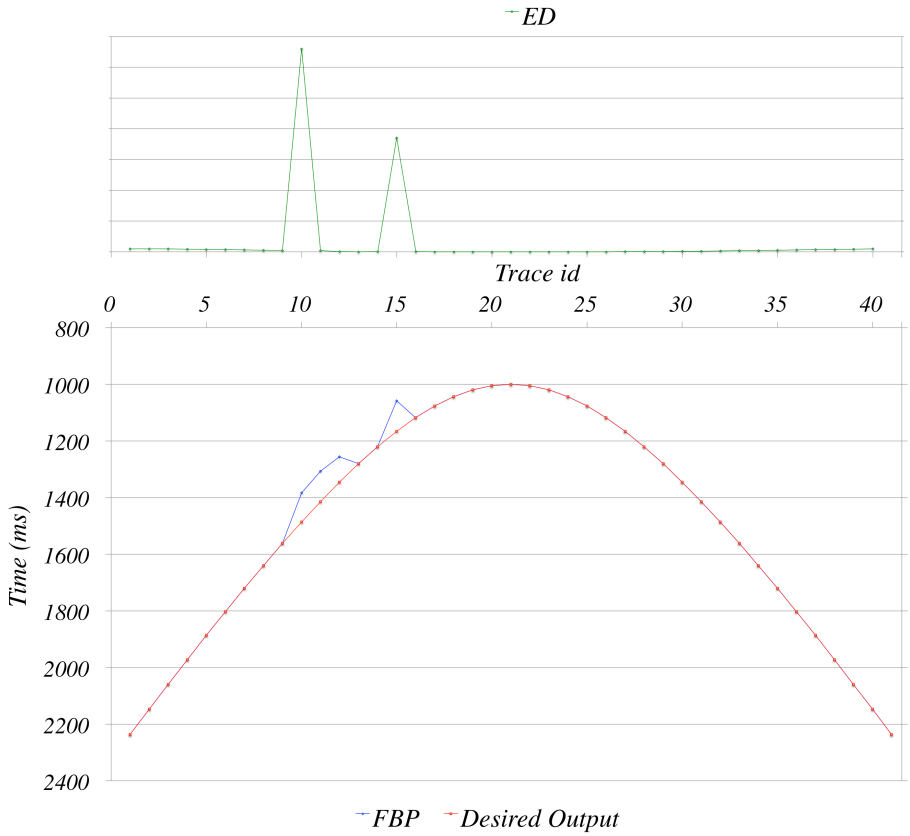

Figure 15 - Synthetic example of first arrival times with successive traces showing clock drift and the corresponding ED profile.

This example shows how to easily identify traces suffering clock drift using ED, but also highlights the problem of successive bad traces. To handle successive bad traces, the

algorithm checks a number of traces after every bad trace and compares the arrival times with a corresponding "theoretical" value calculated via linear regression of surrounding good picks. If the difference in arrival time between the actual and theoretical exceeds the maximum allowed, the trace will be flagged as bad. Depending on the severity of the problems with the timing, the number of traces after each bad trace and the linear regression window may be adjusted to provide better results.

After the identification of all bad traces, a theoretical arrival time will be calculated for every bad trace location, using a linear regression with the surrounding good traces. The static shift correction applied to adjust for the clock drift is simply the difference between the arrival time of the bad traces and the corresponding theoretical value. Figure 16 shows arrival times extracted from a field data both before and after the correction is applied.

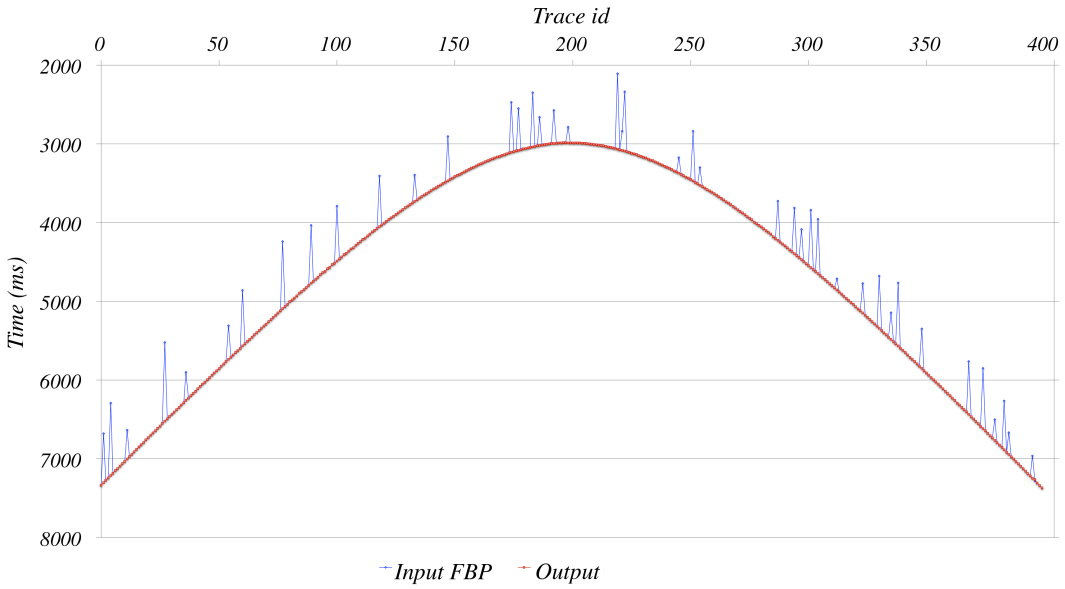

Figure 16 - Arrival times extracted from the field data example in Figure 14, before and after the correction.

3.3. Program and user interface

This clock drift correction method was implemented so as to become part of the SPW software package. The first break picking tools of SPW were used. For that, SPW offers multiple algorithms, and allows the OBS data to be sorted and resorted in any order desired by the user, which makes the processing of multiple records at the time much easier and user-friendly. Figure 17 shows the user interface implemented in the scope of this work for the clock drift correction tool.

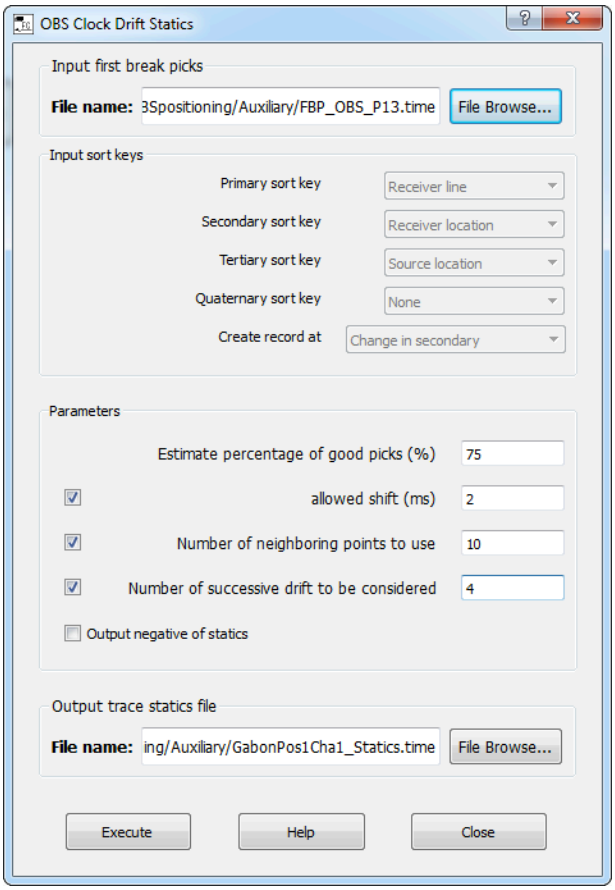

Figure 17 - Screenshot of the user interface of the developed clock drift correction tool.

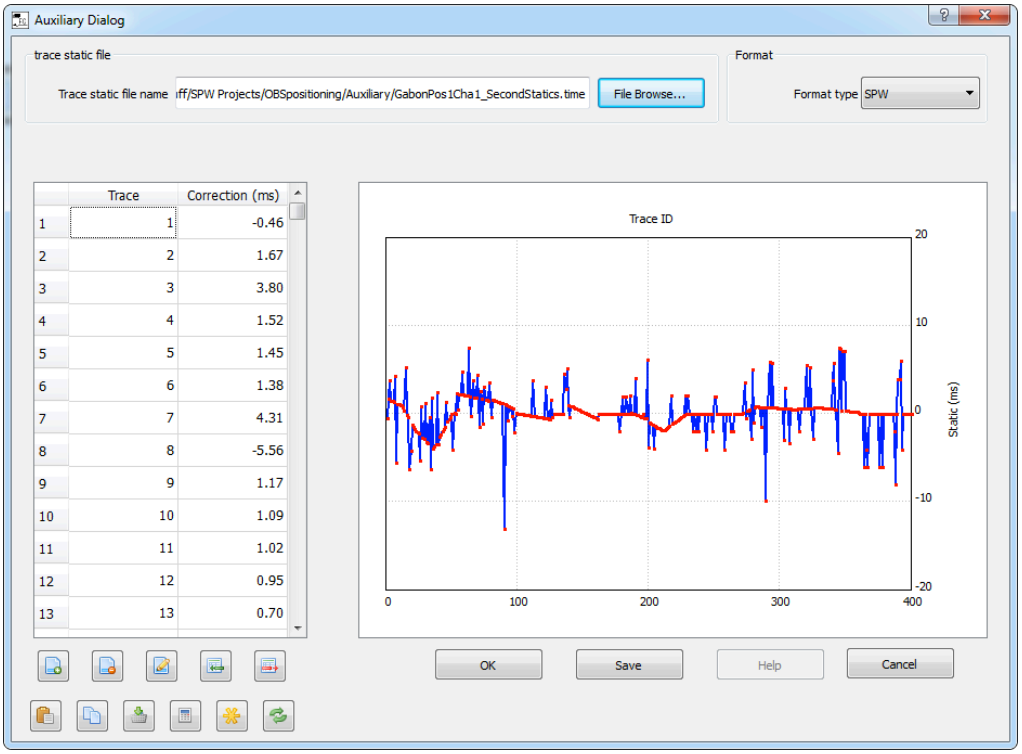

Figure 18 - Screenshot of the trace static file computed using the implemented clock drift correction tool.

The first break picks file is then passed to the clock drift correction tool; this tool reads the file and recognizes the number of records being processed. Then, for each record we compute the static shift value needed to correct the clock drift artifact on the seismic data. The parameters discussed earlier in Section 3.2 can be set optionally by the user through the user interface; otherwise, default values will be used. The computed static shift values can be checked by the user using the auxiliary card dialog (Fig 18). The static shift is then applied to the data using the static shift tool from SPW.

3.4. Application to field data

The method described above was applied to OBS data acquired offshore West Africa, which contains severe clock drift problems. The data was almost noise free; therefore an automatic first breaks picker was used, and no manual editing was required. Figure 19 shows the dataset before and after the clock drift correction.

Figure 19 - a) Raw OBS Seismic data, b) the same seismic data after clock drift correction. The green circles show a close view of the data before and after clock drift correction.

Overall, the clock drift correction succeeded in shifting bad traces into the correct time location, but a meticulous analysis of the data shows: 1) small clock drifts errors of values within the same range as the differential moveout between two adjacent traces were not detected; and 2) bad traces were not shifted to exactly the correct place and there is always a small error left. These errors are primarily due to the lack of accuracy on the first arrivals picks, which will very often be the case in real data. Another reason is the use of linear regression over more sophisticated interpolation methods. Linear regression may be giving a small error, but nothing that can justify what is observed in Figure 19b since the change in the arrival times in a window of about 10 adjacent traces (the window used for regression on this example) is nearly linear. The output result is considerably improved but still not as accurate as is desired; thus further improvements are needed.

The second step consists of flattening the data with a normal moveout correction (NMO) using the water column velocity, re-applying the clock drift correction procedure previously applied, and then applying an Inverse NMO. Figure 20 shows a segment of the same data after applying the NMO, with and without the second step correction.

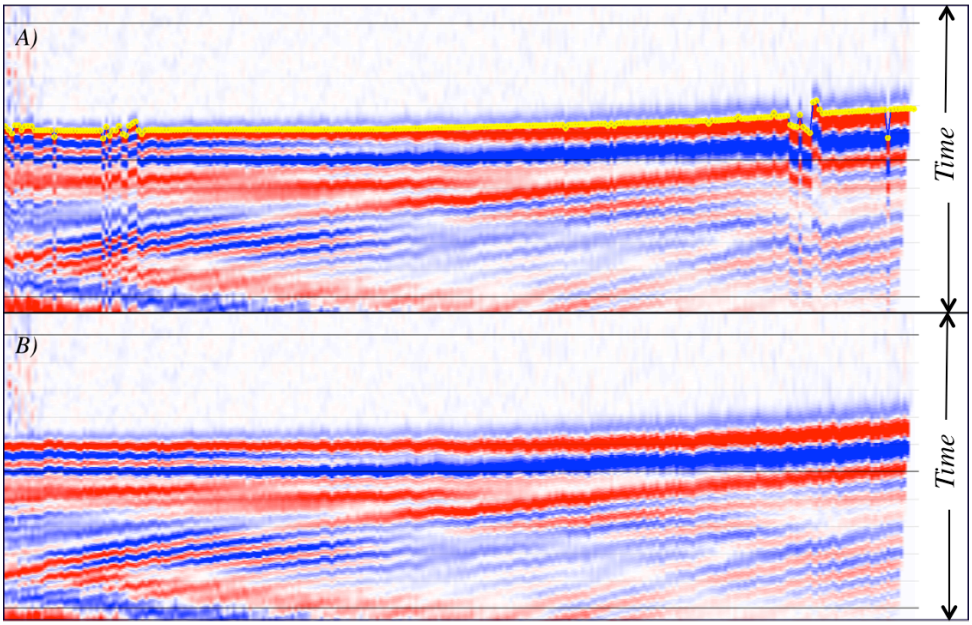

Figure 20 - Flattened OBS seismic data. a) After first step clock drift correction; b) after second step clock drift correction. The yellow dots on (a) are the first arrivals picks.

As shown in Figure 20, the NMO successfully revealed the minor errors and shifts in the data. The exact same procedure as applied in the first step now performs even better, as the

rate of change (derivative) of first arrivals is now truly linear. Figure 21 shows a comparison of data with only one pass of the clock drift correction, and the same data after NMO, a second pass of the clock drift correction followed by the inverse NMO. The data quality is tremendously improved, and all traces are now correctly time-located.

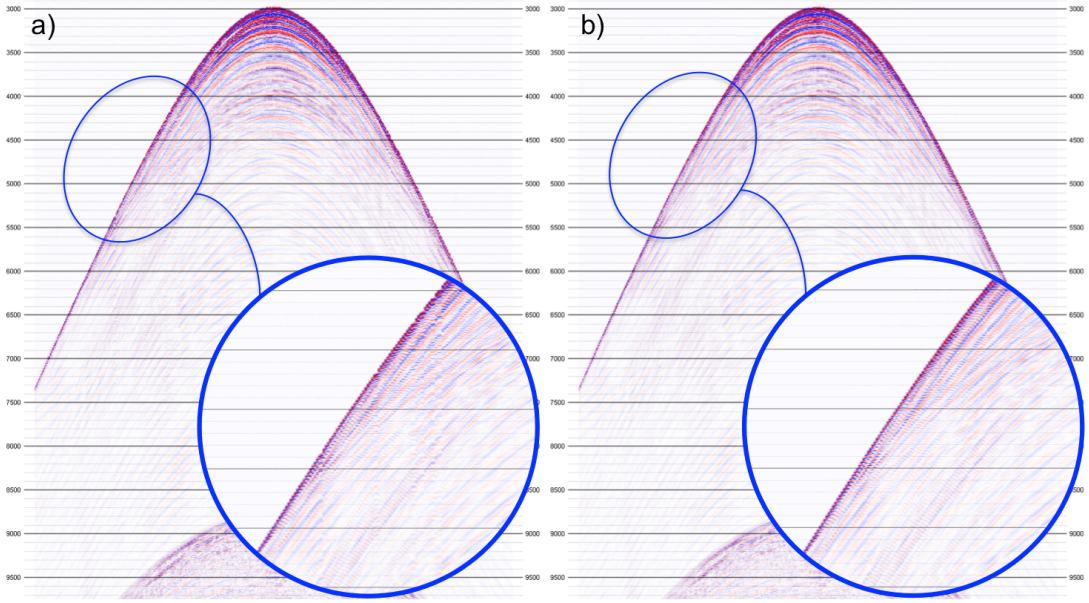

Figure 21 - OBS Seismic data with: a) one pass clock drift correction and b) two passes of clock drift correction, the second pass being applied on NMO flattened data.

A close up comparison with wiggle trace plot is shown in the following figure (Fig. 22), this type of plot makes it easier to compare subtle differences.

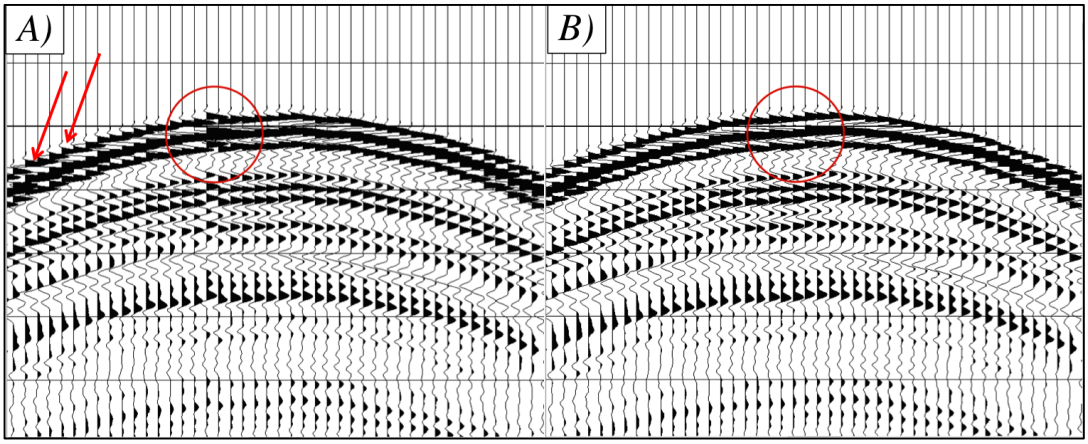

Figure 22 - Wiggle trace plot of a record with: a) one pass clock drift correction, and b) two passes correction.

The comparison shown in Figure 22 highlights the case where the one pass application (Fig. 22a) of the clock drift correction delivered satisfactory results, but still the very subtle

improvement accomplished with the second pass adds more continuity to the seismic events (Fig 22b). Some of these differences are highlighted by the red circles and arrows.

3.4. Conclusions

In this chapter, we presented a new method capable of efficiently eliminating the clock drift effect on recorded seismic data. This methodology is not a replacement for the linear correction applied to the data after OBS recovery via GPS timing, but rather a subsequent correction to eliminate random components of the clock drift. The quality of the final correction depends on the accuracy of the first arrival picks and the number of points used for regression and/or the maximum allowed value of shift. However, the main factor affecting the results is the quality of the first arrival picks. So long as the regression and maximum allowed value are reasonable, they will have a relatively small effect. This methodology has been tested on multiple real field data examples and has successfully removed the random clock drift effects.

Chapter 4

Ocean-Bottom Seismometers positioning

Note: this chapter was partially published as an extended abstract and presented at the 85th SEG annual meeting (2015) in New Orleans under the title:

Accurate Ocean-Bottom Seismometers positioning using Multilateration technique

Omar Benazzouz* and Luis Pinheiro, Universidade de Aveiro.
Daniel Herold, Parallel Geoscience Corporation.
Alexandra Afilhado, Instituto Superior de Engenharia de Lisboa.

A final version of the method presented here has been submitted to the journal "Mathematical Geosciences", under the title:

Accurate OBS positioning method inspired by Multilateration technique

Omar Benazzouz * and Luis Pinheiro, Universidade de Aveiro.
Luis A. Matias, Dom Luiz Institute - Lisbon.
Alexandra Afilhado, Instituto Superior de Engenharia de Lisboa.
Daniel Herold, Parallel Geoscience Corporation.
Seth S. Haines, Central Energy Resources Science Center - United States Geological Survey.

There are two methods currently used for deploying OBS systems. The first method uses remotely operated vehicles (ROV) equipped with very accurate underwater navigation systems to deploy the OBS units; the second method, consists of dropping the OBS unit from the deck of a ship on the sea surface and let it slowly fall to the seafloor. The free fall of the OBS is greatly affected by currents causing it to drift laterally; this means the actual position of the OBS is never the same as the deployment position. This positioning issue is detrimental to the entire OBS data processing (Oshida et al. 2008; Ao et al. 2010; Imtiaz et al. 2013). It is therefore critical to know the exact OBS position to benefit from all the advantages of OBS acquisition systems and to accurately image the subsurface.

4.1. Introduction

Ocean bottom seismometer positioning is a key step in the processing flow of OBS data, especially data acquired with self pop-up types of OBS instruments. The most common method used to get the OBS position is distance measurements from the ship to the OBS utilizing acoustic transponders (Shiobara et al. 1997; Oshida et al. 2008). In order to obtain the OBS position, the boat has to deploy it from the vessel's deck, wait for the descent time and then turn in circles around the deployment site transmitting an acoustic signal. With the help of an acoustic unit mounted on the OBS, the arrival time is computed (Shiobara et al. 1997). This method has two big disadvantages: first, the number of acoustic shots is generally small; and second, the time cost associated with this method is very large (descent time plus the time shooting the acoustic signal). Using first arrivals from airgun shots rather than acoustic transponders should save this time and lead to more accurate positioning, due to the statistics from a large number of shots. In this respect, some authors proposed to use airgun first arrivals energy, sometimes with other supportive data, to invert for the OBS location. Oshida et al. (2008) proposed a non-linear inversion of the first arrival times jointly with a precise bathymetric grid of the study area. Ao et al. (2010) discussed a method based on forward ray tracing and curve fitting of first arrival times and compared it to their Monte-Carlo based curve fitting method. Imtiaz et al. (2013) proposed another approach, inverting for OBS positions and average water layer velocity for all shot lines simultaneously using an iterative least-square method.

The heart of all the methods cited above is a non-linear inversion, which makes sense, because the unknown OBS position is non-linearly related to the measured time of first arrivals. However, the complexity of the problem would be reduced if the OBS position could be described in a linear form.

In this chapter, we present a new positioning algorithm developed within the scope of this thesis. The algorithm uses Multilateration to linearize the problem and solve simultaneously for the OBS position and the average water layer velocity.

Multilateration is a method very well known in surveillance and air traffic control operations (Mantilla Gaviria et al. 2013), and is based on the measurement of the difference in distance, or arrival times, to multiple stations at known locations broadcasting signals at known times. Data from two stations results in an infinite number of locations that satisfy the measurement, representing essentially a hyperbolic curve in 2D case and a one half of a two-sheeted hyperboloid in the 3D case scenario. A second pair of stations produces a second hyperbola intersecting the first one, and the two curves together minimize the number of possible locations to those around the intersection area. Multilateration relies on the differential measurements of multiple stations to converge from possible locations toward the exact location. In order for the multilateration technique to work properly, the stations used for measurements have to be placed at strategic locations to avoid an ill-conditioned system of equations; this is typically known as a sensor placement problem for target localization and, in case we have control over x, y, and z for each station, can be optimized to improve the accuracy of the solution (Mantilla Gaviria et al. 2013; Domingo-perez et al. 2016).

4.2. Developed method

Figure 23 shows a sketch of the OBS acquisition scenario. Here we used only one source line for simplicity. The source positions are known and the distance between each source and the OBS is known in term of time of first arrivals but the water velocity remains unknown.

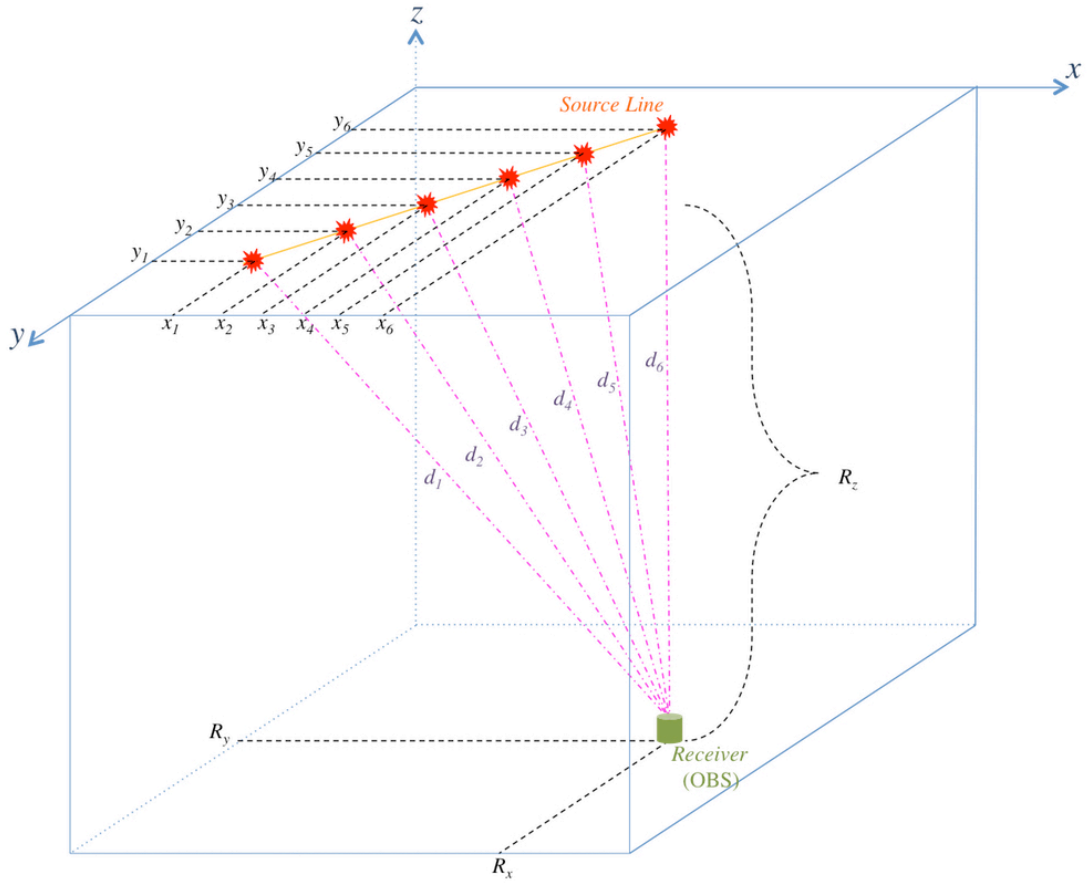

Figure 23 - OBS acquisition sketch with source and receiver (OBS) coordinates. d1 to d6 are the distances between each source and the OBS receiver.

Let S_i (with in this case i = 1 to 6) represent sources with coordinates x_i, y_i, and z_i. t_i and d_i are respectively the time and distance between source S_i and the OBS. The OBS coordinates are R_x, R_y, and R_z. If the water layer velocity was constant and known, this problem will be reduced to finding the intersection point of multiple spheres, each with a center at a source location and a radius equal to the time of the first arrival of the source-receiver pair multiplied by the velocity of the water column. That is solving for a set of equations of this type:

$$d_i^{\,2} = (x_i - R_x)^2 + \left(y_i - R_y\right)^2 + (z_i - R_z)^2 \qquad (4.1)$$

To solve simultaneously for the OBS position and the average water layer velocity, d will be replaced by an average unknown water layer velocity in equation (4.1), as follows:

$$v_{avg}^2 * t_i^{\,2} = (x_i - R_x)^2 + \left(y_i - R_y\right)^2 + (z_i - R_z)^2 \qquad (4.2)$$

In order to linearize equation 4.2, we use a technique known as Multilateration where we calculate the time difference of arrivals by subtracting d_2^2 from d_1^2, d_3^2 from d_1^2, ... d_n^2 from d_1^2, as follows:

$$d_i{}^2 - d_1{}^2 = \{x_i{}^2 - 2R_x x_i + R_x{}^2 + y_i{}^2 - 2R_y y_i + R_y{}^2 + z_i{}^2 - 2R_z z_i + R_z{}^2\} - \{x_1{}^2 - 2R_x x_1 + R_x{}^2 + y_1{}^2 - 2R_y y_1 + R_y{}^2 + z_1{}^2 - 2R_z z_1 + R_z{}^2\} \quad (4.3)$$

Simplifying equation (4.3) and substituting d_i with velocity and arrival time t_i:

$$R_x(x_1 - x_i) + R_y(y_1 - y_i) + R_z(z_1 - z_i) + v_{avg}^2(t_1{}^2 - t_i{}^2)/2 = (x_1{}^2 - x_i{}^2 + y_1{}^2 - y_i{}^2 + z_1{}^2 - z_i{}^2)/2 \quad (4.4)$$

From equation (4.4) and a scenario of n shots, we can write a linear system A*X = B, where A is n-1 by 4, X is the vector $[R_x; R_y; R_z; v_{avg}^2]$, and B is a vector of size n-1:

$$\begin{vmatrix} (x_1 - x_2) & (y_1 - y_2) & (z_1 - z_2) & (t_1{}^2 - t_2{}^2)/2 \\ \vdots & \vdots & \vdots & \vdots \\ (x_1 - x_i) & (y_1 - y_i) & (z_1 - z_i) & (t_1{}^2 - t_i{}^2)/2 \\ \vdots & \vdots & \vdots & \vdots \\ (x_1 - x_n) & (y_1 - y_n) & (z_1 - z_n) & (t_1{}^2 - t_n{}^2)/2 \end{vmatrix} * \begin{vmatrix} R_x \\ R_y \\ R_z \\ v_{avg}^2 \end{vmatrix}$$

$$= \begin{vmatrix} (x_1{}^2 - x_2{}^2 + y_1{}^2 - y_2{}^2 + z_1{}^2 - z_2{}^2)/2 \\ \vdots \\ (x_1{}^2 - x_i{}^2 + y_1{}^2 - y_i{}^2 + z_1{}^2 - z_i{}^2)/2 \\ \vdots \\ (x_1{}^2 - x_n{}^2 + y_1{}^2 - y_n{}^2 + z_1{}^2 - z_n{}^2)/2 \end{vmatrix} \quad (4.5)$$

Both "A" and "B" are known and can be constructed from source positions and first arrival times; so, theoretically solving this linear system should give us the OBS position, but this will not work correctly yet. The third column of the matrix "A" is (z_1 – z_2), which in our OBS acquisition model corresponds to the difference between the depth of two sources and is generally equal to zero; the same applies for (z_1 - z_i) in vector "B". This means a solver will always return a value of R_z equal to zero. The depth of the OBS can only be deduced if the sources were placed at different relative depths. The other possibility is to use a two steps approach, computing first R_x, R_y, and v_{avg}^2 and then R_z.

Using the same differentiation technique as in equation (4.3), the relationship between the offset at each source location and the source-receiver distance (d) can be linearized as follows:

$$Offset_i = \sqrt{d_i^2 - R_z^2} \qquad (4.6)$$

Which means:

$$Offset_i{}^2 - Offset_1{}^2 = d_i^2 - d_1^2 \qquad (4.7)$$

A set of equations of type (4.7) translate to the corresponding linear system:

$$\begin{vmatrix} (x_1 - x_2) & (y_1 - y_2) & (t_1{}^2 - t_2{}^2)/2 \\ \vdots & \vdots & \vdots \\ (x_1 - x_i) & (y_1 - y_i) & (t_1{}^2 - t_i{}^2)/2 \\ \vdots & \vdots & \vdots \\ (x_1 - x_n) & (y_1 - y_n) & (t_1{}^2 - t_n{}^2)/2 \end{vmatrix} * \begin{vmatrix} R_x \\ R_y \\ v_{avg}^2 \end{vmatrix}$$

$$= \begin{vmatrix} (x_1{}^2 - x_2{}^2 + y_1{}^2 - y_2{}^2)/2 \\ \vdots \\ (x_1{}^2 - x_i{}^2 + y_1{}^2 - y_i{}^2)/2 \\ \vdots \\ (x_1{}^2 - x_n{}^2 + y_1{}^2 - y_n{}^2)/2 \end{vmatrix} \qquad (4.8)$$

Now that we solved for the OBS easting and northing plus the average water layer velocity, the next step is to use the Pythagoras theorem and for each source *i* the OBS depth will be equal to:

$$R_z = \sqrt{d_i^2 - Offset_i^2} \qquad (4.9)$$

The offset here is the horizontal distance between each source and the OBS, *d* is the time of first arrivals multiplied by the average water layer velocity. R_z will be computed using the arrival times and offset of all shot-receiver pairs individually. We have used here the average value as the actual OBS depth. The RMS, median or weighted average could also be used to better account for variations in the R_z values. Statistical analysis of these variations is a future topic of study.

Generally, first arrival values as well as the source coordinates may contain some errors and may not as accurate as would be desired, but the multiplicity of the input data (number of shots used) will compensate for these errors. A good linear equation solver capable of handling such "noisy" system has to be used to solve the linear system in (4.5) or (4.8). In our case, the solution was implemented using a solver based on singular value decomposition (SVD), which uses orthogonal matrices to reduce the matrix "A" thus minimizing the risk of magnifying inaccuracies in the input data.

SVD methods are based on the following theorem of linear algebra (whose proof is beyond our scope): Any $m \times n$ matrix A with $m \geq n$ (overdetermined matrix), can be written as the product of an $m \times n$ column-orthogonal matrix U, an $n \times n$ diagonal matrix W with positive or zero elements (the *singular values*), and the transpose of an $n \times n$ orthogonal matrix V, with matrices U and V are each orthogonal in the sense that their columns are orthonormal as shown by the following illustration (Vetterling et al. 2002).

$$\begin{pmatrix} & \\ & \mathbf{A} \\ & \end{pmatrix} = \begin{pmatrix} & \\ & \mathbf{U} \\ & \end{pmatrix} \cdot \begin{pmatrix} w_1 & & & \\ & w_2 & & \\ & & \cdots & \\ & & \cdots & \\ & & & w_N \end{pmatrix} \cdot \begin{pmatrix} & \\ & \mathbf{V}^T \\ & \end{pmatrix}$$

Figure 24 - Singular Value Decomposition (SVD) of an overdetermined matrix A.

Once the matrix "A" is decomposed, a back substitution routine is used to find the vector of unknown "X" as follows:

$$\begin{pmatrix} \\ \mathbf{x} \\ \\ \end{pmatrix} = \begin{pmatrix} & \\ & \mathbf{V} \\ & \end{pmatrix} \cdot \begin{pmatrix} \\ \mathrm{diag}(1/w_j) \\ \\ \end{pmatrix} \cdot \begin{pmatrix} & \\ & \mathbf{U}^T \\ & \end{pmatrix} \cdot \begin{pmatrix} \\ \mathbf{b} \\ \\ \end{pmatrix}$$

Figure 25 - Back substitution of the SVD decomposed matrix "A" to solve for the unknown vector "X".

To implement this inversion, a single source line cannot be used unless it is curved. Figure 26 shows how a single straight line (case A) cannot distinguish between a left sided and a right sided receiver, because indeed both positions are solutions to the same system of equations. When the source line is curved (case B), however, times of first arrivals are no longer symmetric and therefore the inversion is constrained to the proper solution.

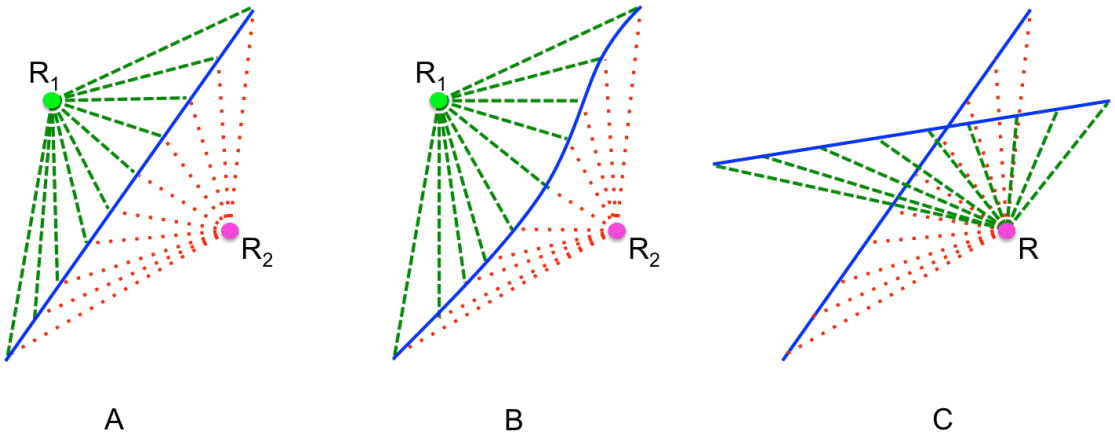

Figure 26 - Multiple scenarios of sources shot into a receiver. A) Single straight source line. B) Single curved source line. C) Two crossing source lines.

Using two or more crossing source lines (case C) ensures more constrains on the inversion process. This is the same conclusion drawn by Ao et al. (2010).

One of the important assumptions to note, is that equation (4.1) describes a straight ray path in the water column, which is a valid assumption for the near offsets, but at large offsets, the ray path usually will be severly curved due to sound speed velocity variations in the water layer and the assumption is no longer valid. Therefore, the use of first arrival picks in a narrow offset window provides a better constraint on the inversion, and thus leads to a more accurate positioning.

4.3. Test with simulation data

To test the method, we first built a simple scenario with four source lines, each line with fifty shot locations and placed a receiver in between the lines at a depth of -2143 meters. The water layer velocity was taken to be constant (1500 m/s), as the objective of this test is not to mimic real field conditions at this stage but only to validate the concept. The depth of the OBS and acquisition geometry was taken arbitrarily with the only consideration of having crossing source lines. Figure 27 shows the geometry of the shot lines; the corresponding first arrival times are shown in Figure 28.

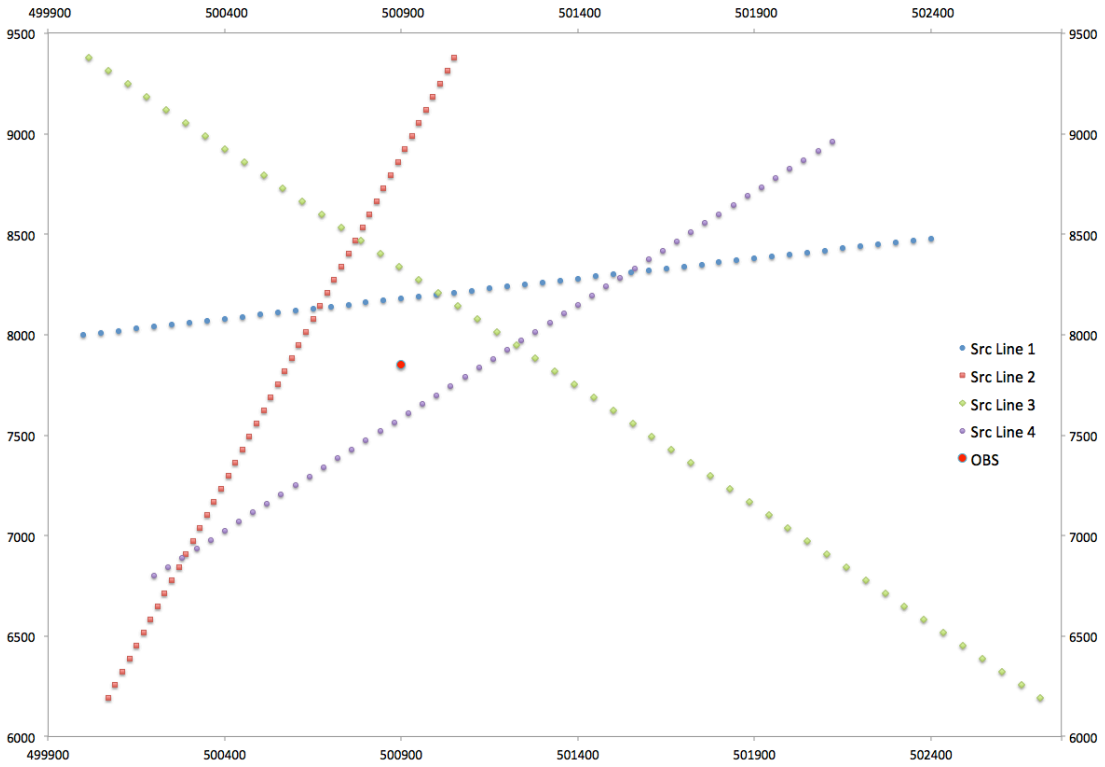

Figure 27 - Simple OBS acquisition geometry with four source lines, the red dot in between is the OBS receiver.

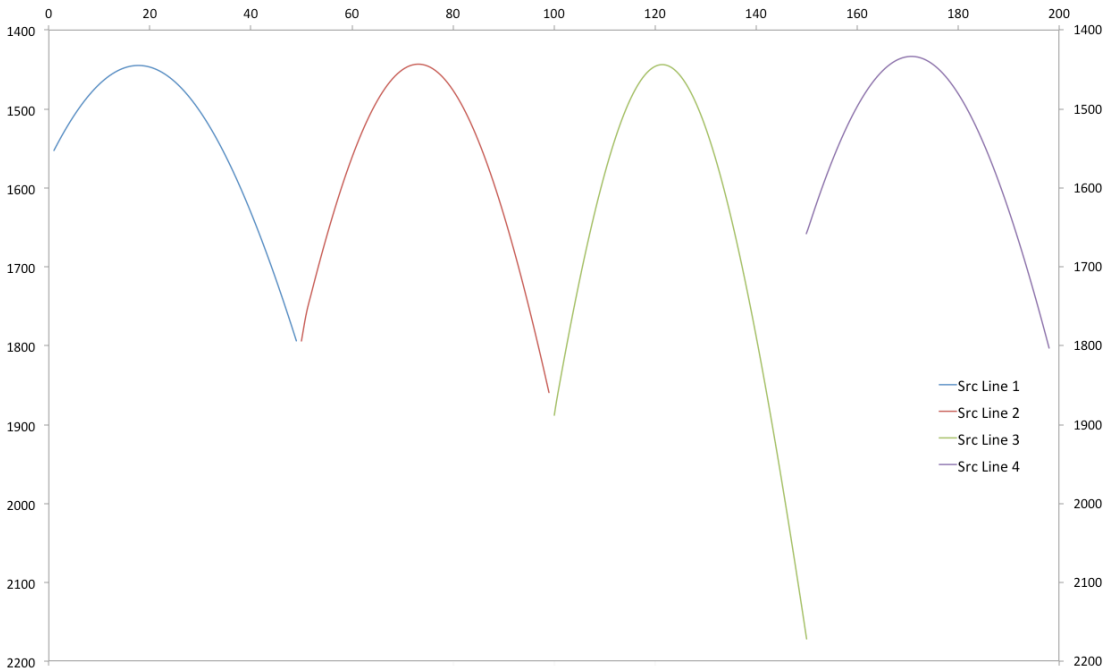

Figure 28 - First arrival times corresponding to the acquisition geometry shown in Figure 27. The vertical axis is time in millisecond, and the horizontal axis is shot number.

First, we put the sources at random depths (between 0 and 100 m depth) and use the corresponding times of first arrivals to run the inversion shown in equation (4.5). Then we put all sources at the same depth (6 m), which is closer to usual field conditions, and use the corresponding first arrival times to run the inversion in equation (4.8) followed by equation (4.9) to get the depth of the OBS. Both inversions gave the same results, as expected, due to the fact that the water layer velocity used in this model is constant and so there were no inaccuracies caused by velocity variation in the travel path and therefore the inversion returned exact values.

4.4. Program implemented and user interface

The proposed OBS positioning method was implemented in the scope of this work as a processing step in the SPW seismic processing software package; again the first break picking tools of SPW were used, and the picks file was then passed to the new OBS positioning tool. As an alternative, the new step can read first arrivals directly from trace header words. Indicating the sources are at similar depth forces the step to use equation (4.8) for the inversion; otherwise equation (4.5) will be used. The user interface (Fig. 29) allows the user to set a warning message if the inversion returns a water velocity far from the expected range, thus making sure the inverted values are reasonable.

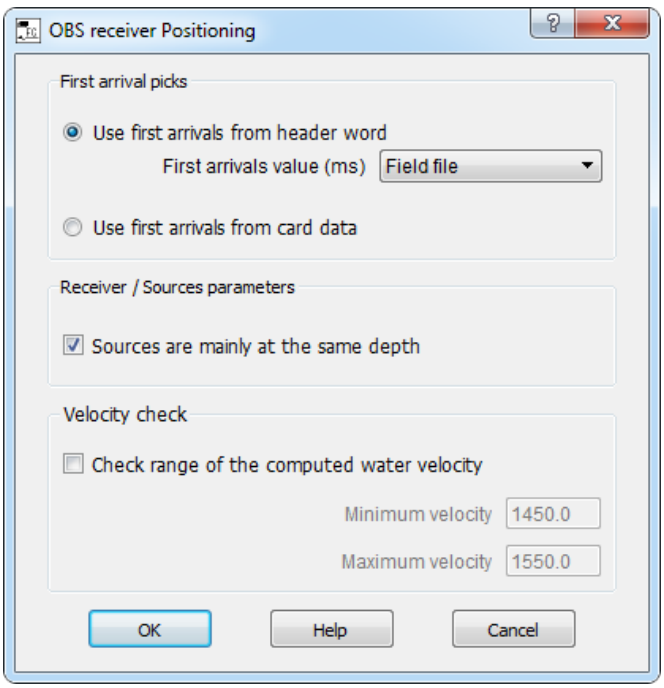

Figure 29 - Screenshot of the implemented user interface of the OBS positioning tool.

4.5. Application to field data

4.5.1. Example 1: Sardinia

In this example, we present the results of the application of the developed OBS positioning algorithm to field data acquired offshore Sardinia at about 1600 meters depth with two crossing shot lines. This data was acquired to analyze the crustal structure and is discussed in more details in Moulin at al. (2015). Figure 30 shows a receiver gather with the first arrivals picks used for the inversion as in equation (4.8).

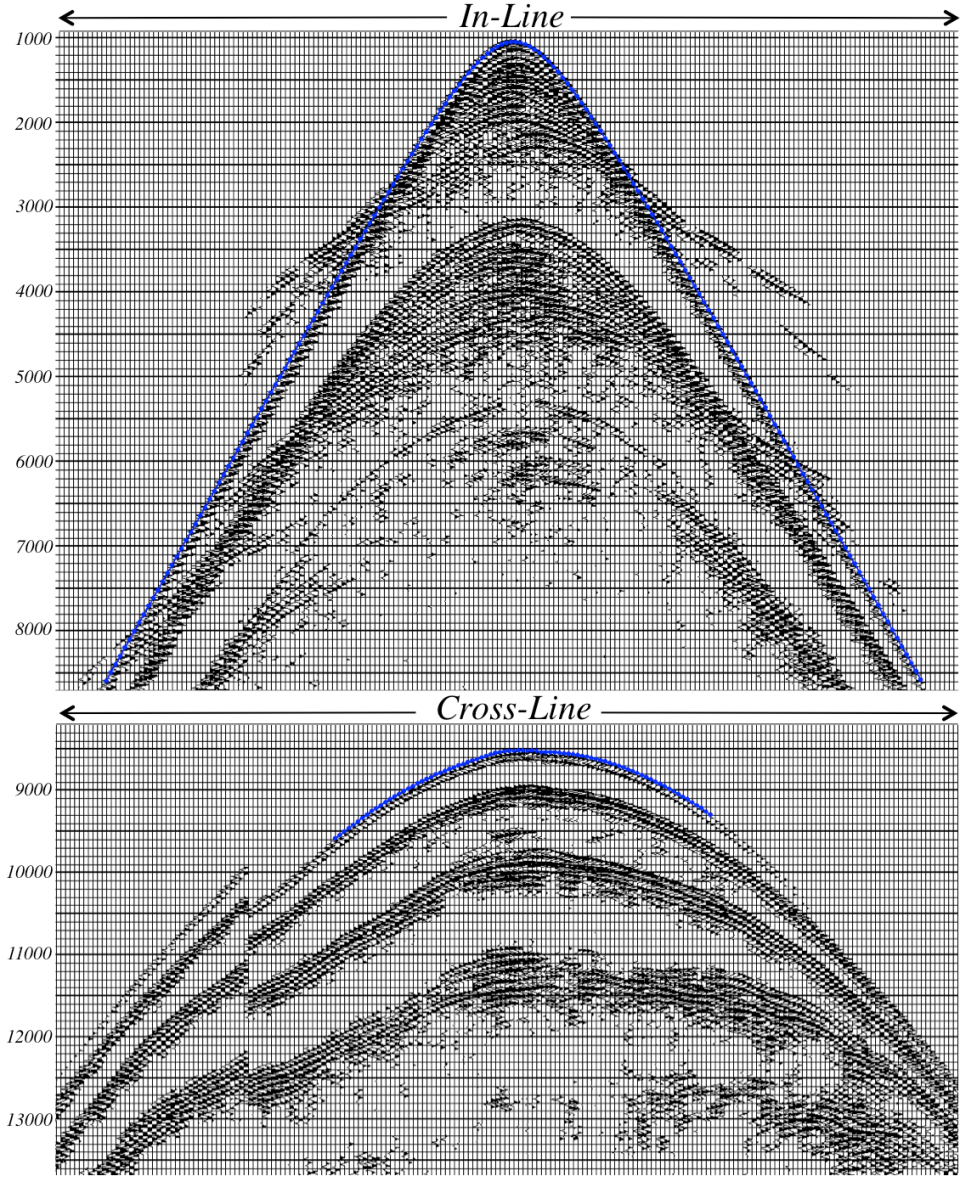

Figure 30 - In-line and cross-line OBS record used for the inversion. The vertical axis shows time in milliseconds. The blue lines are the picked first arrivals.

The first arrival times were picked in a narrow offset window, in the in-line direction the maximum offset used was about 13 km, and in the cross-line the maximum offset was about 14.5 km. In order to verify the accuracy of the inversion results, first arrival times were forward computed using the inversion results (OBS position, depth, and average water layer velocity). The computed first arrival times were plotted on top of the seismic data and visually checked with the recorded first arrivals.

The OBS position, water depth and water layer average velocity were also computed with a brute force method starting from the drop position and exploring the solution space (Moulin et al. 2015) The misfit of the forward computed first arrival times with the actually picked first arrivals were quantified by the root mean square deviation (RMSD) for comparison. The brute force method has an RMSD of 18.37 milliseconds. The proposed method implemented here showed superior accuracy with an RMSD of 1.74 milliseconds. However, the RMSD in this case should not be thought of as a means of measuring the accuracy of the positioning; part of the error in the RMSD could be caused by accuracy of the first arrivals picks; also, the inversion process tries to find a water velocity fitting the observed arrival times and minimizing the errors in positioning, but that doesn't mean that the seismic wave propagated with that given average velocity.

4.5.2. Example 2: Bay of Biscay

The data used in this example was collected in the Bay of Biscay (West of France) for refraction studies of the deep crustal structure of the Armorican Basin; more details about the data acquisition are found in Thinon et al. (2003). In this case we have two OBS locations: the first one has two quasi-perpendicular shooting lines and the second location has a crooked line shooting geometry (fig. 31). This will allow the use of these two receiver locations to understand the effect of shooting geometries on the accuracy of the final positioning. The first step is to use all shooting azimuths for each receiver location to position the OBS and then run other inversions without the picks that fall in certain azimuth and compare the results. Figure 31 shows the acquisition geometry at each OBS location and the picks used in each inversion.

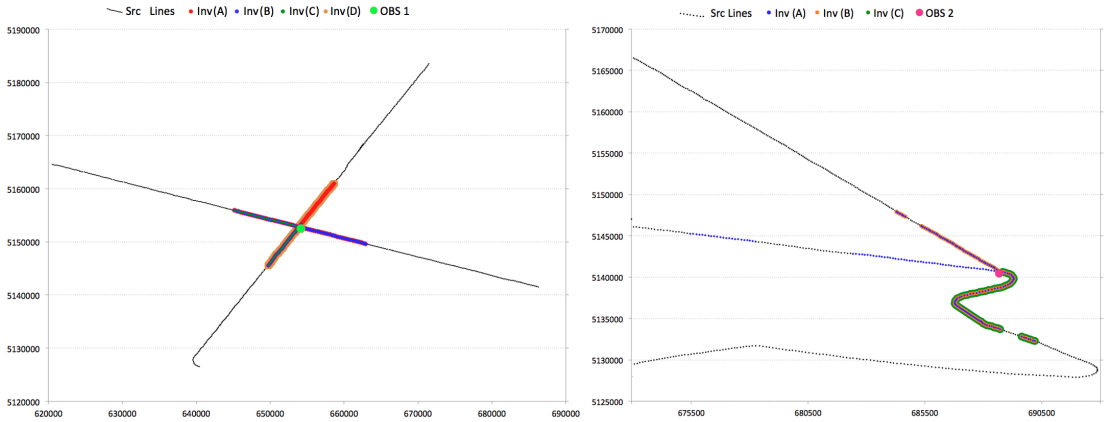

Figure 31- Shooting geometry at two OBS locations in the Bay of Biscay. To the left with two quasi-perpendicular shooting lines, and to the right with crooked lines geometry. The picks used for each inversion are shown in different colors and identified by capital letters for later reference.

The comparison of the results focuses on lateral and vertical OBS position and water layer velocity (Fig. 32).

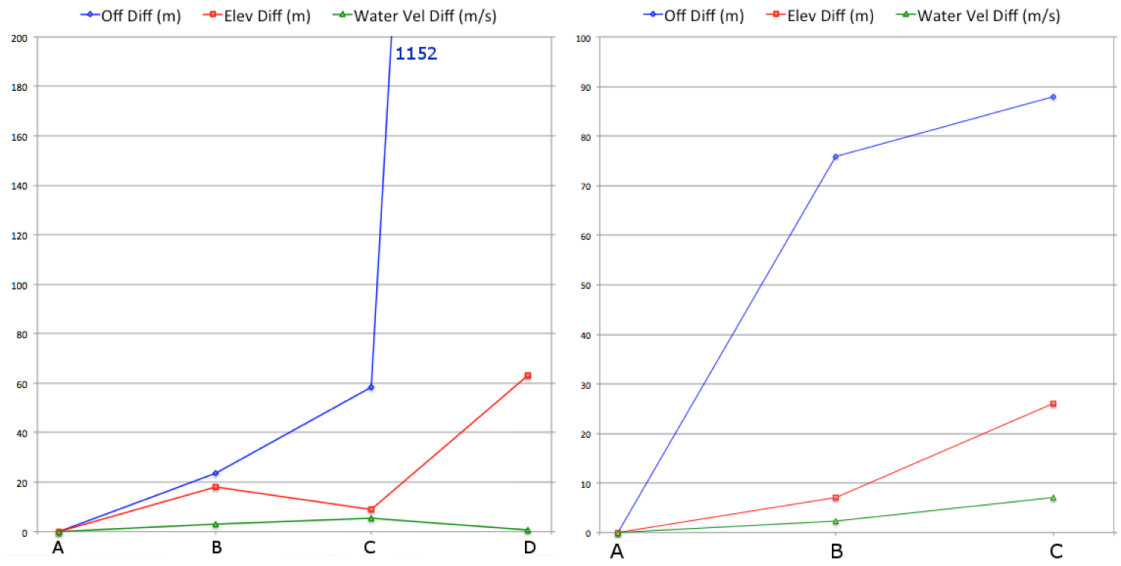

Figure 32 - Results of the comparisons of the lateral and vertical positions of each OBS (Off diff / Elev diff) and the water layer velocity (Water Vel diff); on the left for the first OBS location and on the right for the second. The picks used for each inversion (A, B, C, and D) are shown in Figure 31.

The results of each inversion are compared to the results of the inversion "A" for both OBS locations. The results of these comparisons suggest that decreasing the azimuthal coverage influences the lateral position of the OBS the most. Also, Inversion "C and D" on the first OBS location, shows that a 2D line that crosses the OBS location can still yield a reasonable positioning, with less than 10 meters shift on the vertical position and about 60

meters shift on the lateral position. However, when only one side of the 2D line was used the lateral shift was more than a kilometer.

4.5.3. Example 3: Green Canyon dataset – Gulf of Mexico

The Green Canyon dataset was acquired by the U.S. Geological survey in the Gulf of Mexico area in 2013 to refine geophysical methods for gas hydrate characterization and achieve improved imaging of established gas hydrate study sites, as described in the cruise report (Haines et al. 2014). For OBS deployment, the standard academic approach was followed and the OBS(s) were dropped by free-fall from the sea surface in carefully selected locations. The water depth is about 2000 m in the area, the sink times were approximately 30 minutes, and the lateral drift was anticipated to potentially be as large as a few hundred meters. Figure 33 shows the study area and a portion of the acquisition grid.

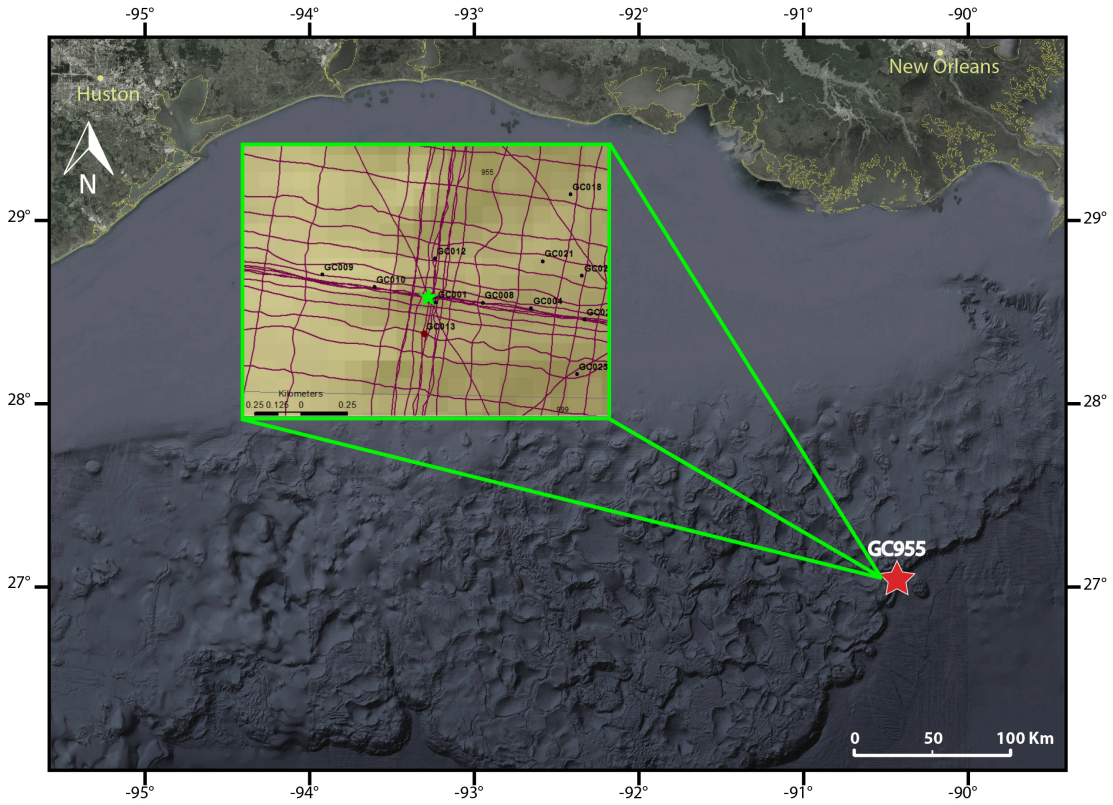

Figure 33 - Map showing the Gulf of Mexico and the Green Canyon 955 study area. The green box shows a portion of the acquisition grid and the green star shows the location of the OBS used for this test.

The OBS location GC001 was used for this test and the first arrival times from a number of shots from multiple surrounding lines were picked. Figure 34 shows the geometry of the

source lines in blue; in red are the shot locations used for the inversion process, and in green is the inverted position of the OBS GC001. The maximum offset used in this test is about 2.5 km, meaning the average water layer approximation and the straight ray propagation should provide good accuracy.

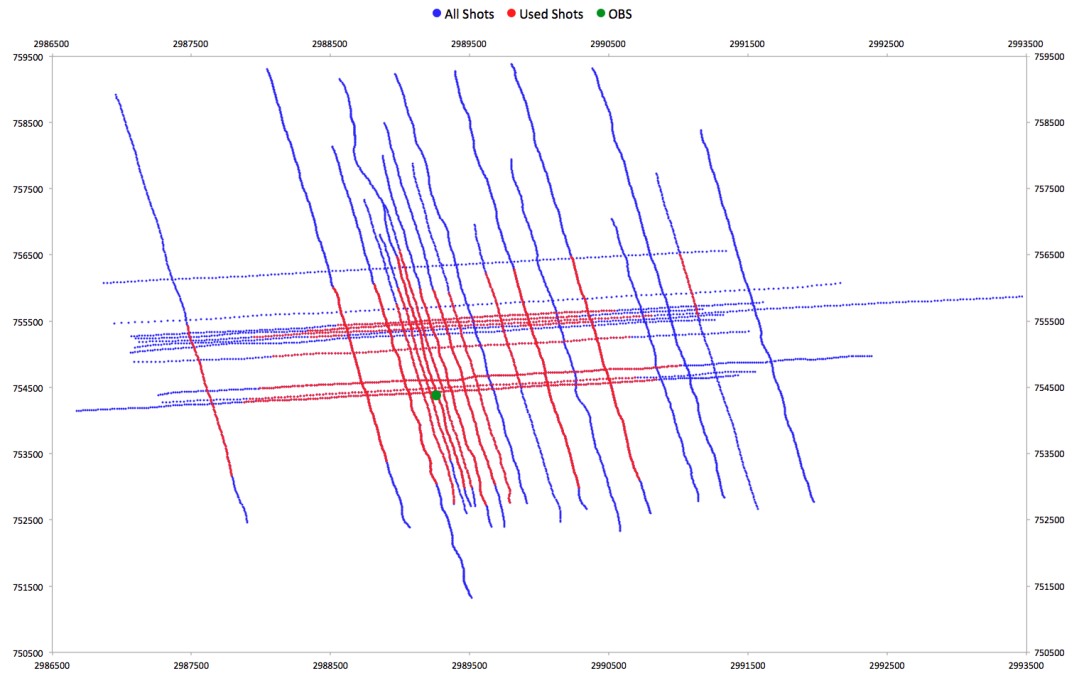

Figure 34 - A map view showing the position of the shots used for the positioning algorithm and the actual OBS position. The vertical and horizontal axes are northing/easting with UTM zone 15N.

After running the inversion as shown in equation (4.8/4.9), we forward computed the travel-time of first arrivals from each source to the OBS position using the source locations and the inverted OBS position and average water layer velocity, and then computed the differential error between the computed and picked first arrivals (Fig. 35). The differential errors range between +/-12 milliseconds.

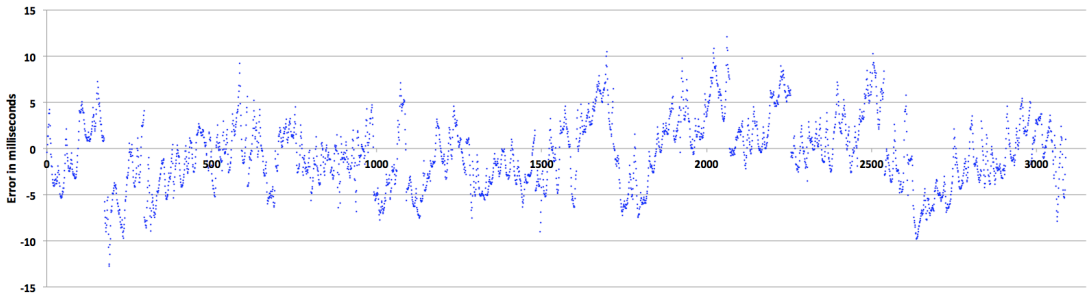

Figure 35 - Differential error of travel-time of first arrivals. Vertical axis is the error in milliseconds and the horizontal axis is the trace number.

In order to further assess the accuracy of this inversion, we computed the magnitude of the differential error (absolute value) and sorted it in an ascending order. Figure 36 shows the graph of this differential error.

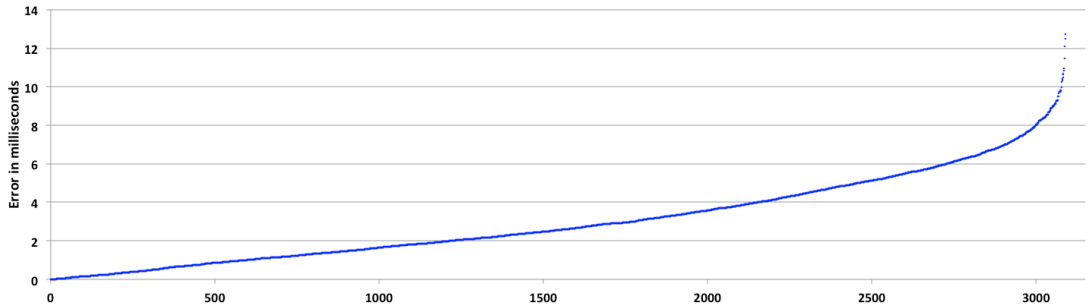

Figure 36 - Magnitude of the differential error of travel-time of first arrivals sorted in an ascending order. Vertical axis is the absolute error in milliseconds and the horizontal axis is the trace number.

From this graph, we can easily see that more than 80% of the picks (2500 pick) have an error with a magnitude less than 5 milliseconds. The average and median errors were determined to be 3.06 and 2.56 milliseconds respectively. These are very satisfactory results given that the seismic data was sampled at 5 milliseconds; this indicates that the differential errors are within the accuracy limits allowed by the picks of the first arrival times used as input data in the inversion.

In order to assess the effect of the azimuthal distribution of shot locations and the total number of the used shots for the inversion, we ran eleven experiments with the same inversion process removing two or three source lines each time (Fig. 37).

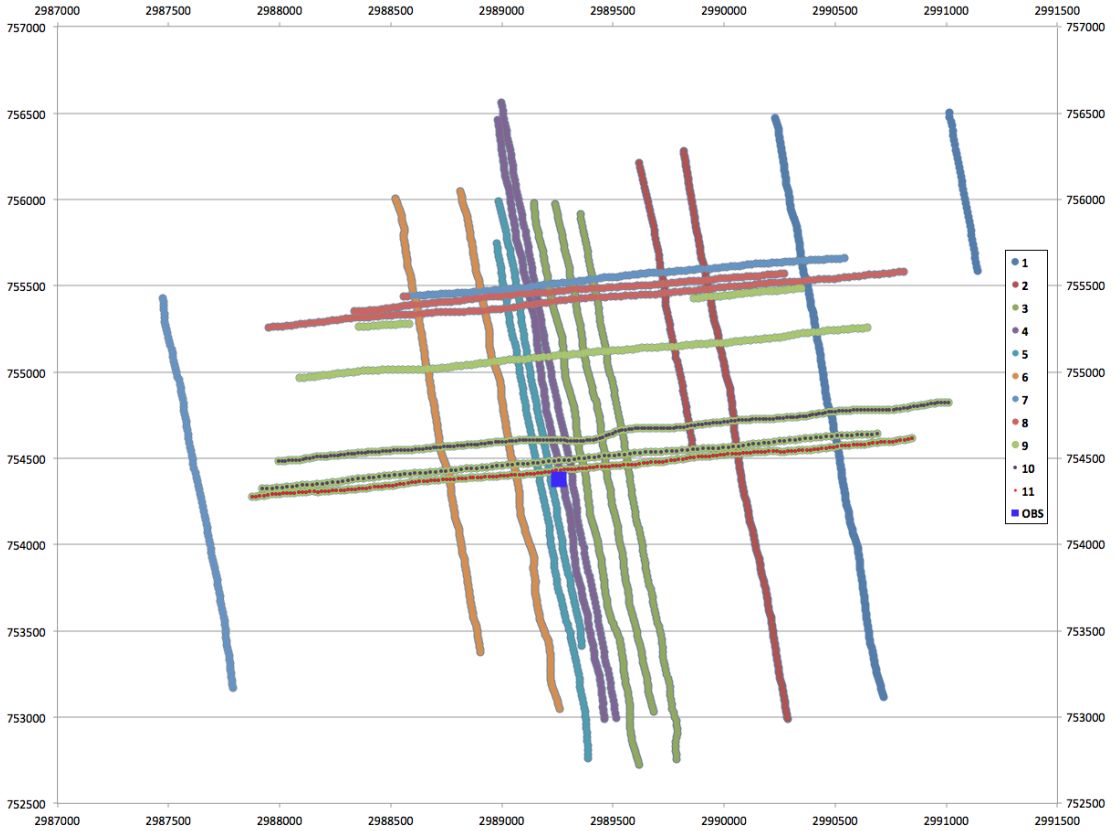

Figure 37 - Source lines used in each experiment (1 to 11). The blue box shows the OBS position. The vertical and horizontal axes are northing/easting with UTM zone 15N.

The results of these experiments were compared with the original inversion (using all source lines) in term of lateral drift, vertical position, and the average water layer velocity. Figure 38 shows the results of the comparison.

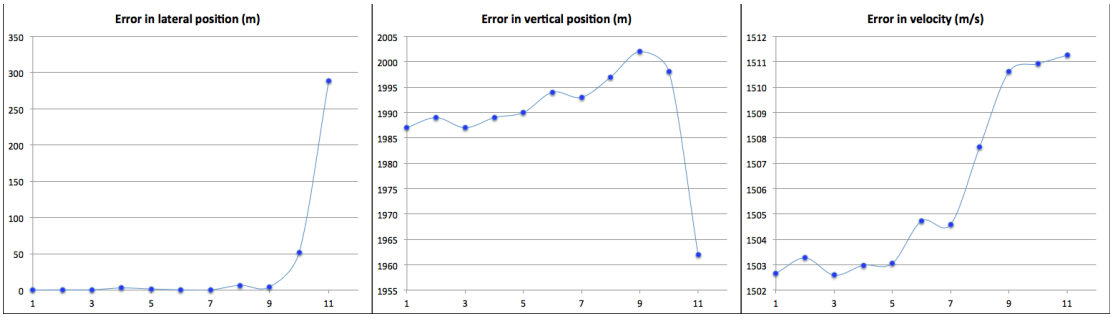

Figure 38 - Comparison of differences in the OBS lateral/vertical position and average water layer velocity computed with different inversion scenarios; the horizontal axis refer to the experiment number and is the same as in Figure 37.

The azimuth of each source/receiver pair of all traces used during each experiment was also computed and is shown in Figure 39.

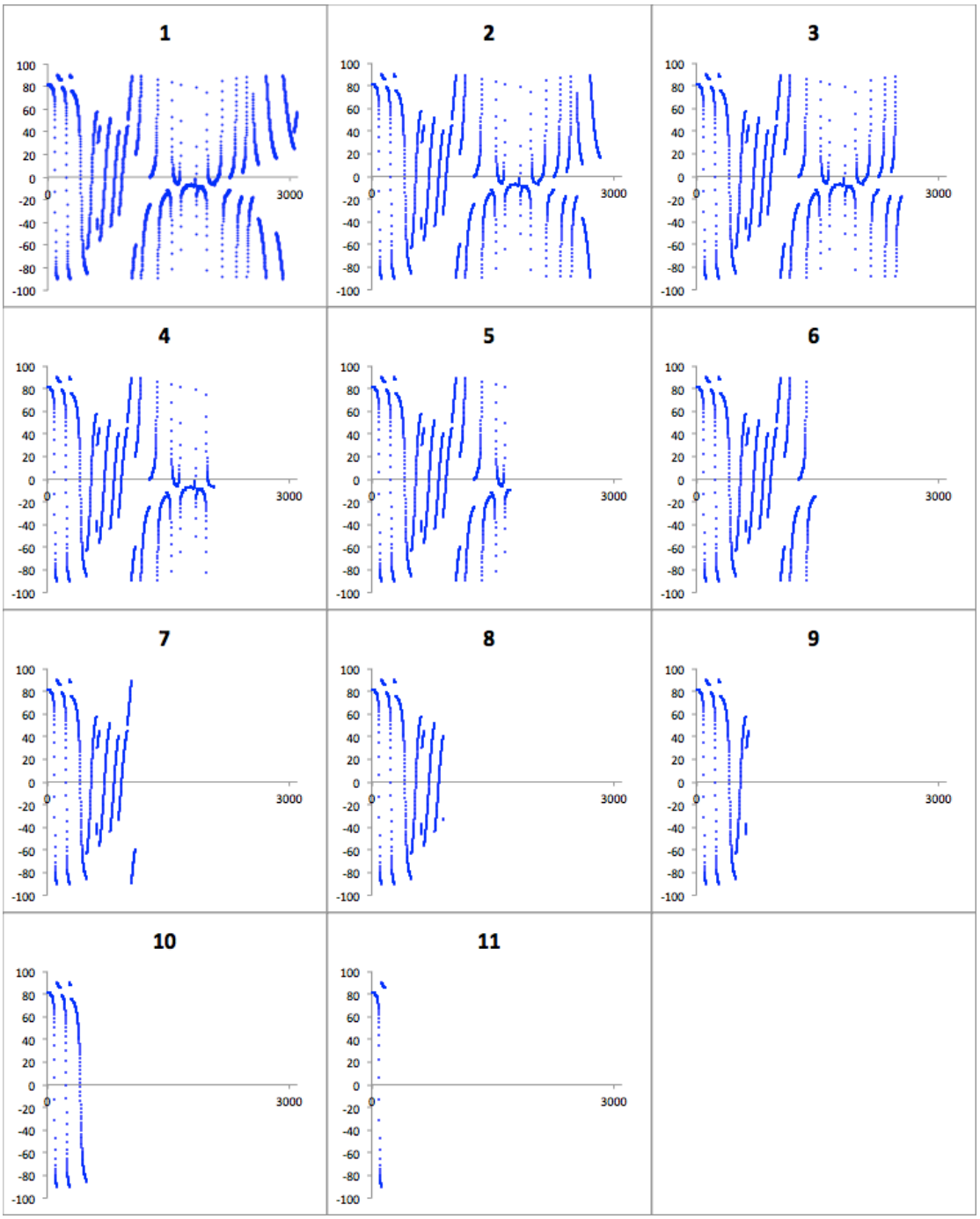

Figure 39 - Each graph shows in vertical axis the azimuthal angle of each source/receiver pair used in the inversion, in degrees, and in horizontal axis the number of picks used (source locations). The number on top of each graph is the experiment number and is the same as in figure 37.

From Figure 38 and 39, we see that the experiments 1 to 9 have wide azimuthal coverage and they all give a very similar lateral position (within 5 meters). Experiments 10 and 11 have very poor azimuthal coverage in the angle range between about +/- 40 and +/- 60 degrees respectively and give a lateral position error of approximately 50 to 300 meters.

However, the error in vertical position follows almost a linear trend (up to 15 meters) with the number of picks used except in the last experiment where the error jumps to 36 meters. Regarding the error in the average water layer velocity, we can distinguish three groups: the first one with an error of less than 0.5 m/s; the second which increases almost linearly to up to 5 m/s error and the last group with experiment 9, 10, and 11, which reaches an error of 8 m/s.

From this comparison, we can say that the lateral position is affected the most by the azimuthal coverage while the number of picks used affects equally the vertical position and the average water velocity. In general, higher azimuthal coverage and larger number of picks (within the short offsets used in this experiment) are naturally preferred, while small azimuthal coverage and small number of picks are going to result in lower accuracy. For most applications in seismic data processing, 10 meters accuracy in both lateral and vertical positions is very satisfactory; a scenario as in experiment 9 will lead to reasonable results.

4.6. Conclusions

The new OBS positioning method developed in the scope of this thesis efficiently linearizes the problem of OBS positioning and solves simultaneously for the OBS position, depth, and average water layer velocity. The method was validated by forward computation of the first arrival times using the inversion results and visual check with the recorded seismic energy. The accuracy of the positioning is mostly influenced by the azimuthal distribution of the shot locations. While the total number of first arrival time picks impact the accuracy, it has less weight. Using a larger number of first arrival time picks mostly compensates for inaccuracies in the first arrival time picks. The use of singular value decomposition for the linear solver provides extra robustness as it can handle inaccuracies in the input data.

Chapter 5

Pre-stack depth migration of OBS data

OBS data are usually processed as common receiver gathers to get the highest lateral sampling as discussed in Chapter 1.2. Each Node is therefore processed and migrated as an independent 2D (single source line) or 3D (multiple source lines) dataset and then merged together afterwards. Constructing the diffraction hyperbola/surface with common receiver gathers is very similar to that of source gathers; the only difference is in the case of shot gather data, for each imaging point we need one *Ts* (the time from the source to the imaging point) and multiple *Tr* (the times from the imaging point to each receiver) (see Fig. 10, in Chapter 2). For common receiver gathers on the other hand, the time from the imaging point to the receiver is constant for each imaging point and thus computed only once; it is the time from each source to the imaging point that needs to be computed multiple times. Also important to mention is the shape of the diffraction in this case, which is dictated by the travel-time from each source to the imaging point as opposed to the time from the imaging point to the receiver in the case of shot gathers.

Kirchhoff pre-stack time migration is a relatively a fast migration compared to the pre-stack depth migration as discussed in chapter 2. It is therefore necessary to explore whether it can be implemented to handle OBS data without losing the time cost advantage or not. Figure 40 shows the difference between the recorded energy in the OBS case as opposed to the streamer case. In the case of streamer acquisition (fig. 40b), for each recorded seismic trace, the reflection points are vertically one below the other and form almost a straight line, if joined. On the other hand, with OBS acquisition (fig. 40a), the data recorded on each trace falls into a curve, which can be defined using the interval velocity model and a ray tracing technique. This will make it almost a depth migration in the sense that it will honor lateral and vertical velocity changes to find the reflection point. But then, it would make more sense not to use the DSR equation to estimate diffraction's travel-time and use instead the more accurate travel-time from the ray tracing, since the ray tracing has already been carried out. As such we can conclude that Kirchhoff pre-stack time migration loses the time coast advantage when dealing with OBS data, and therefore it becomes a more suitable option to directly use the Kirchhoff pre-stack depth migration.

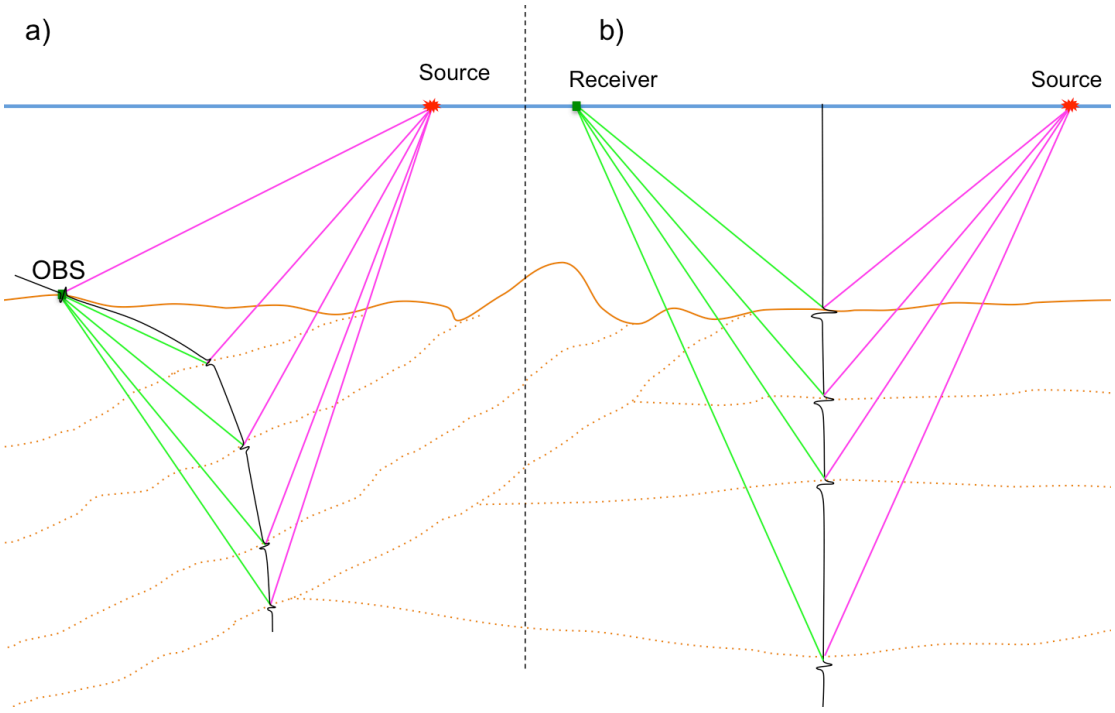

Figure 40 - Recorded energy of a seismic trace in a) OBS recording versus b) streamer recording.

5.1. Travel-time computation and velocity field

One of the key properties of a seismic signal, and perhaps the most important of all, is its travel-time. It allows to directly infer useful information about the Earth's interior (velocity, distance, attenuation, etc.). Travel-time computation has applications in multiple domains and contexts; it is widely used in seismic modeling and imaging, but it is also of utmost importance in fields such as velocity analysis and tomography (Sava and Fomel 1998). In this section, we describe broadly some techniques and methods used for the computation of travel-time tables required by the depth migration algorithms that will be implemented in the scope of this work.

The most commonly used methods of travel-time computation fall into two categories: ray tracing and numerical solutions of the eikonal equation (Nowack 1992; Sava and Fomel 1998). Ray-tracing methods compute arrival times along the ray path. In this context, rays are referred to as the trajectories along which high-frequency energy flows (Nowack 1992). The greatest advantages of ray tracing methods are the speed of computation, the small memory requirements, the possibility to separate elementary seismic waves, and the ability to compute multiple arrivals (Ben-menahem and Beydoun 1985; Bucha 2004). However,

in shadow zones and other velocity regions with complex interference phenomena, ray-tracing methods might either fail to find the correct first arrival ray or will require large computational costs (Qin et al. 1990). On the other hand, numerical solutions to the eikonal equation can handle these complexities in the velocity model more efficiently and are getting more and more robust (Vidale 1988; Qin et al. 1990; Podvin and Lecomte 1991; Nowack 1992).

There are two different approaches to compute and store travel-time tables. In the first one, we shoot rays from the imaging point upward. In this case, for each imaging point $I(x,y,z)$ a new set of travel-times must be computed from $I(x,y,z)$ to all upper surface points in question, namely all sources and receivers (Julian and Gubbins 1977). The time spent computing a different travel-time for each output point can easily exceed the time spent in the Kirchhoff summation (Gray 1986). The second approach was introduced in the late nineties by Gray, and consists of ray tracing from the top down. That is, rays are shot downward from the upper surface, from each source or receiver location and through the entire velocity model; the velocity model can be constrained with the desired illumination geometry. The top-down approach allows efficient ray calculations at a depth $z+\Delta z$, depending only on the previously computed ray information at depth z and the continuation of the rays from z to $z+\Delta z$. Basically, raypaths and slowness integrals are computed over short segments of raypaths (the segments lying between z and $z+\Delta z$). In the upward shooting approach however, slowness integrals must be computed over the entire raypath for every depth. Therefore, shooting rays downward eliminates a large duplication of effort in travel-time calculations (Gray 1986).

Travel-time computation, whether it is done using ray-tracing techniques or by solving the eikonal equation, often has to be carried out on a uniformly sampled grid. A geophysicist typically runs a velocity analysis tool to generate a set of velocity functions at different CMP locations or CMP bins. The choice of the distance between different functions is normally based on previous knowledge of the study area. A complex geological setting will require a denser distribution of velocity functions compared to a simple undeformed sedimentary basin. Moreover, velocity analysis tools usually generate velocity functions based on CMP locations, but sources/receivers might be out of the CMP coverage area. The CMP

coverage is enough for time migration algorithms, as the RMS velocities considered in the DSR equation are taken only at CMP location. However, for ray-tracing purposes and depth migration algorithms, this coverage must be extended to cover all source/receiver locations. Figure 41 illustrates this situation in both 2D and 3D case.

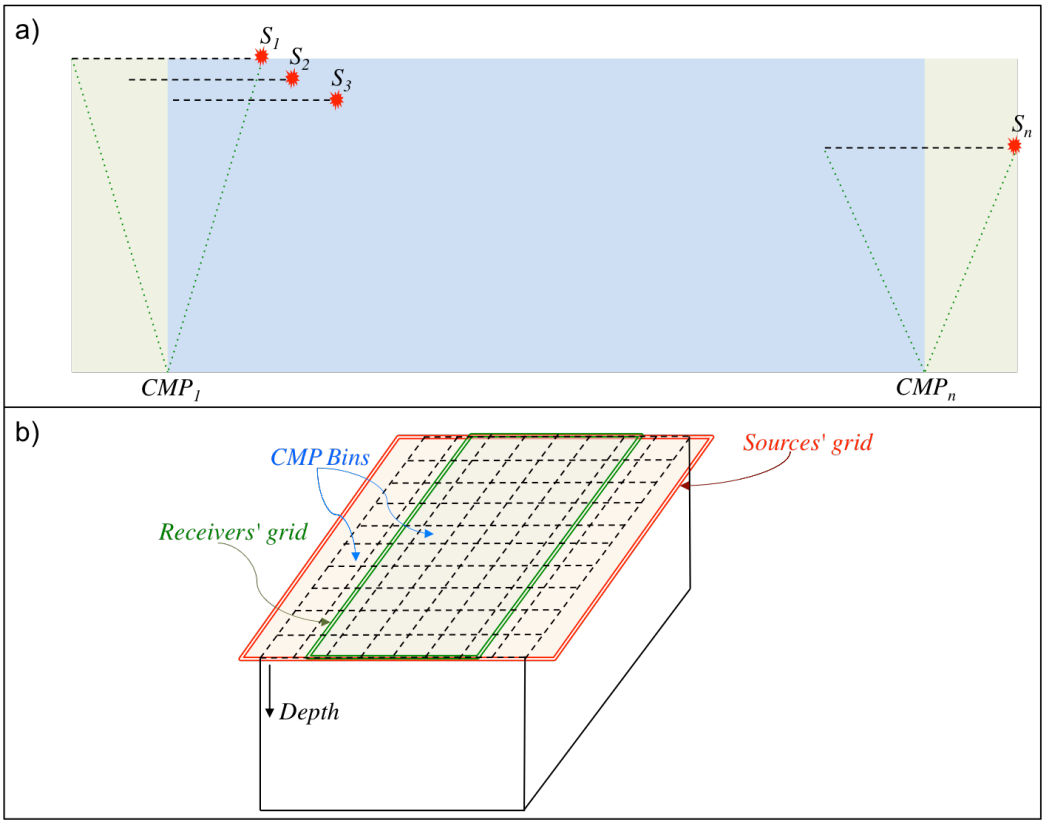

Figure 41 - Illustration of CMP coverage versus the coverage of sources/receivers in: a) 2D acquisition and b) 3D acquisition case.

In the 2D case (Fig. 41a), we can clearly see that the region corresponding to the CMP coverage (blue box) does not include all sources and receivers (green box). The same for the 3D scenario presented here (Fig. 41b), given the source grid represented in red and the receiver grid represented in green, the CMP bin grid (the grid in dashed lines) will not cover all source positions. A tool was created, in this respect, not only to interpolate velocity functions into a continuous and uniformly sampled grid, but also to extrapolate the grid geometry to cover all sources and receivers (Fig. 42). The file type of the velocity field was chosen to be a "SEG-Y" file with velocity information instead of signal amplitude, as this would keep all geometry information in the header fields of the file and would make it very practical from a programing point of view. It is also very helpful for the user as it allows the

use of the 2D visualizer from SPW or any other 2D/3D SEG-Y file visualizer for display and quality control.

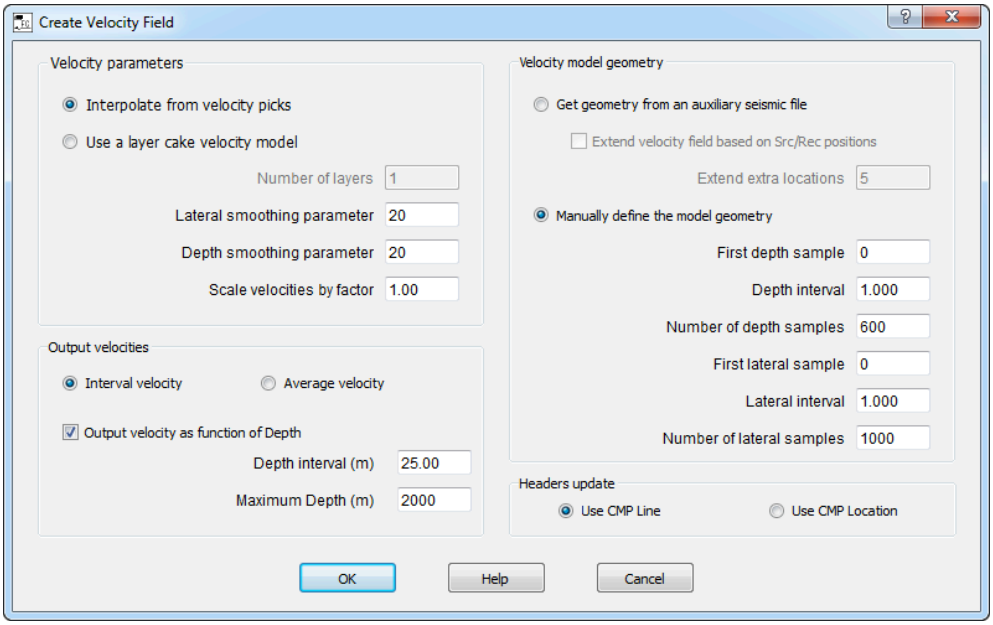

Figure 42 - User interface of the tool implemented in this work to create velocity field files.

The new tool created, shown in Figure 42, allows the user to create velocity fields from picked velocity functions or simply by defining a simple layer cake model. An auxiliary seismic file or manual settings may be used to define the geometry. Typically the pre-stack seismic file should be used as the auxiliary file for geometry; in this way, a perfect match is attained between the geometry of the velocity model and the seismic data. The tool can output the velocity field in depth or in time, and can output either interval velocities or average velocity (in the following text, for practical reasons the term average velocity is used interchangeably as RMS velocities). The implemented lateral/depth smoothing option will be explained in the upcoming paragraph.

One of the most important underlying assumptions of ray theory is that the velocity model in which the rays are computed should be smooth within the dominant wavelength of the seismic wave (Cerveny 2001). Basically, the problem happens when the reflected ray path is approximately parallel to the computational incident wave front. Smoothing the velocity field can suppress the curvature of the ray path and avoid such turned rays (Zhenyue 1993a). An under-smoothed velocity model cannot eliminate migration artifacts arising from velocity discontinuities, while an over-smoothed velocity model will lead to large

travel-time errors and thus to a distorted image. Velocity smoothing also benefits eikonal equation solvers. The upwind finite difference method, for instance, provides an efficient way to solve the eikonal equation but fails in the presence of turned rays (Vidale 1988; Vidale 1990; Vidale and Houston 1990). Therefore, a velocity-smoothing algorithm will benefit the migration by stabilizing the ray tracing only if it is capable of smoothing strong discontinuities without losing much details of the velocity structure.

Convolutional-type smoothing operators, such as boxcar smoothing and triangle averaging, are either discontinuous or their derivatives are discontinuous, hence are not very effective when the velocity structure has strong discontinuities. Another problem is that some regions in the velocity field may require more or less smoothing then other regions, but convolutional-type smoothing methods cannot change operator length easily to account for such local smoothing requirements. Moreover, the computational cost in this type of smoothing operators is proportional to the size of the operator, which makes it very expensive especially for 3D cases and large datasets.

In the implementation proposed here, input velocity smoothing is carried out using a method based on damped least squares (DLS) (Zhenyue 1993a). The DLS method smooths the velocity field by minimizing (1) the weighted sum of the derivation between the smoothed velocity and the original one, (2) and the first derivative of velocity with respect to spatial variables. This formulation is equivalent to a second order differential equation, which can be solved very efficiently. In this respect, the smoothed velocity in the single dimensional case, is determined by:

$$\int \omega(x)\,(V_s(x) - V(x))^2 dx + \alpha^2 \int \left(\frac{dV_s}{dx}\right)^2 dx = min \qquad (5.1)$$

Where V is the original velocity, Vs is the smoothed velocity, α is the smoothing parameter and $\omega(x)$, ranging from 0 to 1, is a weighting function.

The weighting function $\omega(x)$ imposes a local constraint between the original velocity and the smoothed one. Generally, the quality of the velocity model degrades with depth. In order to accommodate this issue, a useful choice would be for the weighting function to decrease with depth (Liu and Bleistein 1991). One example would be to choose:

$$\omega(x) = \frac{1}{1 + \mu^2 x^2} \qquad (5.2)$$

In this case x is the depth and μ is a constant. The larger the value of μ, the faster $\omega(x)$ decreases with depth. The multidimensional version of the DLS method is the same minimization as in equation (5.1) but carried out over each dimension (or axis) instead of the x-axis only as in the above example.

The execution time related to this method is independent of the smoothing operator length, as shown in equation (5.1), making it ideal for multidimensional and large datasets. Furthermore, the DLS method, by using the derivative of velocity with respect to spatial variables, inherently handles local variation of smoothing needs for any given velocity model. More details on the DLS smoothing method can be found in (Zhenyue 1993b).

The DLS smoothing method was implemented in SPW as a filtering tool giving it the possibility to operate directly on "SEG-Y" files. The DLS filter has also been tested for other applications out of the main subject of the thesis, with very promising results (*e.g.* migration noise reduction, ice cracks artifact attenuation). The implemented user interface (Fig. 43) allows the user to either smooth the entire velocity field or just a specific part, by defining a window within which the DLS will be applied.

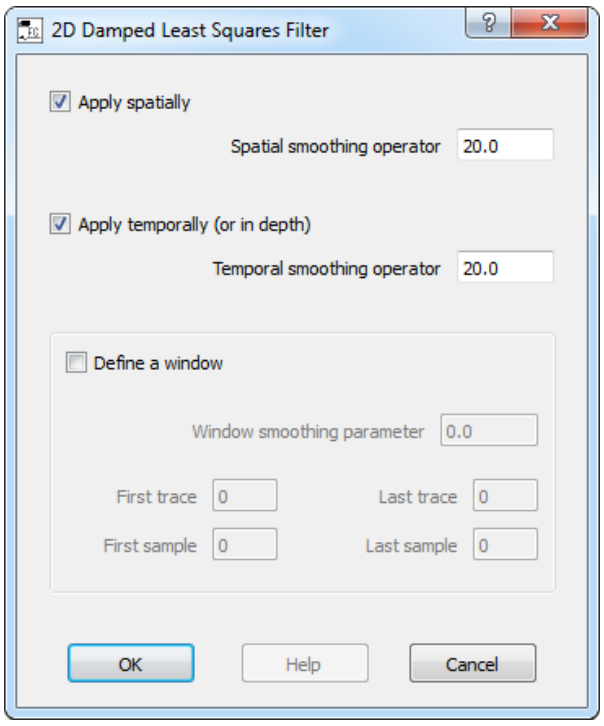

Figure 43 - Screenshot of the user interface of the DLS filter implemented in the scope of this thesis.

To demonstrate the superiority of the DLS method, we will use a 2D velocity model built using a standard velocity analysis (constant velocity scanning) and apply two different smoothing methods, the DLS and a boxcar median smoother. The dimensions of this velocity model are 125x200 cells. Figure 44 shows the raw velocity model.

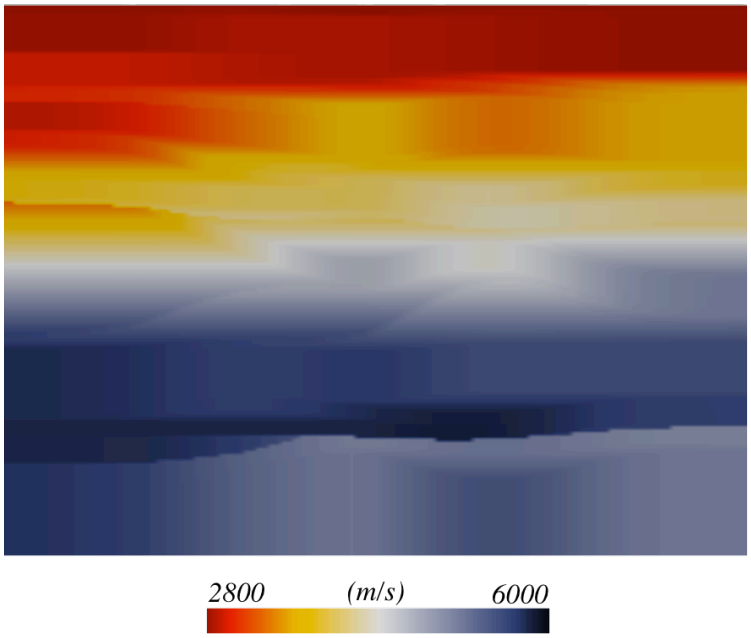

Figure 44 - Raw velocity model of 125x200 cells. Velocity ranges from 2800 to 6000 m/s.

The first smoothing method whose application we will show is a median boxcar filter. We will use three different operators of following sizes: 25x25, 50x50, and then 100x100 points. Note the computation time increases exponentially with operator size. Figure 45 shows the obtained results.

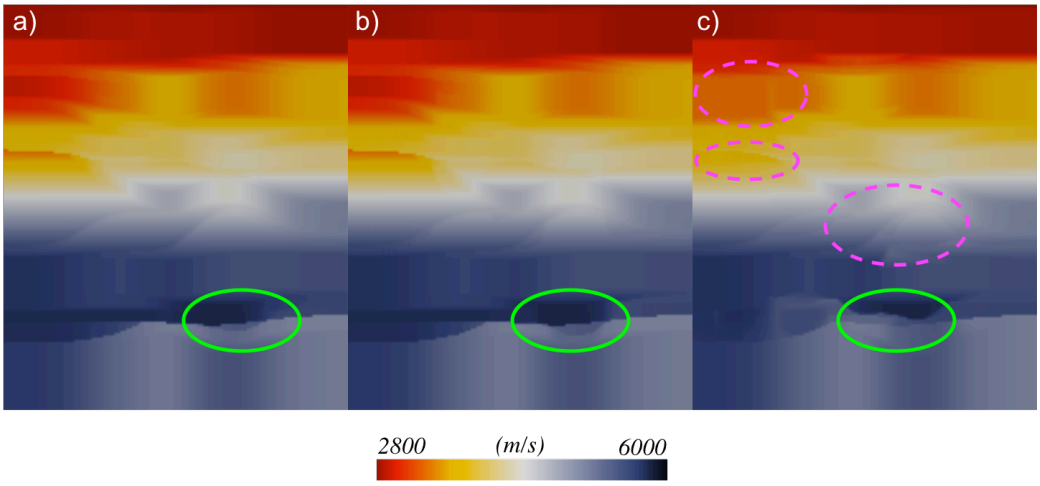

Figure 45 - The same velocity model as in (fig. 5.5) smoothed using a median boxcar filter of size: a) 25x25, b) 50x50, c) 100x100. The same color scale as in (fig. 44) is use to allow direct comparison.

Besides the expensive computational cost, the results from the median boxcar filter are not smooth enough to benefit the ray tracing algorithms, and are substantially altered compared to the original raw data. The green circles highlight how the increased size of the filtering operator destroyed the geometry of the velocity structure in the presence of a strong discontinuity without actually smoothing the transition from the one velocity to another. The dashed pink circles highlight several other velocity structures which were either completely destroyed or severely modified. This is probably not the most sophisticated smoothing method available, but it is certainly one of the most common methods used in daily practices, thus the need for another more reliable smoothing algorithm. Figure 46 shows the result from the DLS method compared side by side to the raw data:

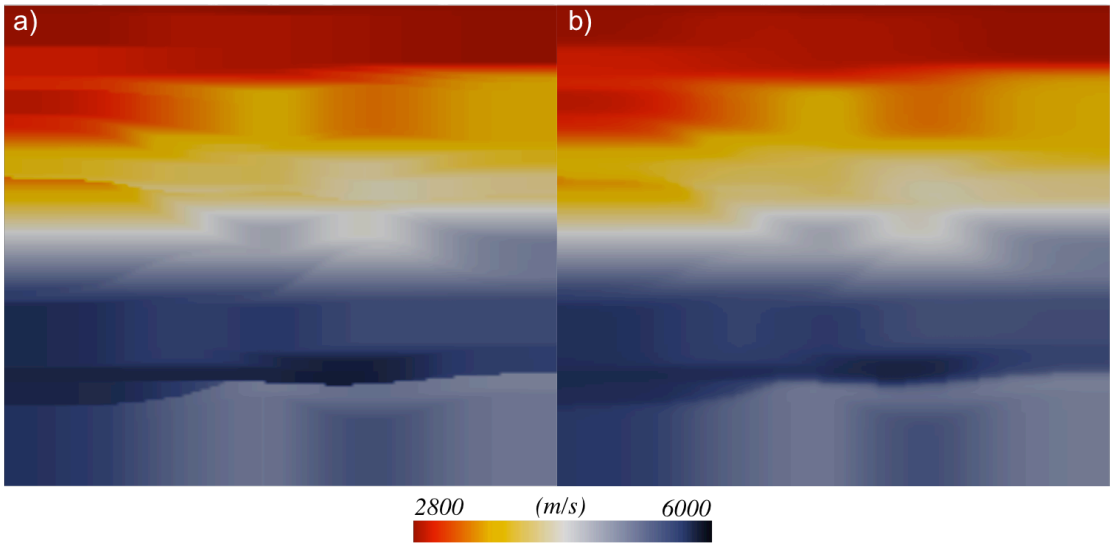

Figure 46 - Side by side comparison of: a) the raw velocity model, b) a smoothed velocity model using the DLS method and an operator size of 2x2.

Figure 46 clearly demonstrates the superiority of the DLS smoothing method; sharp discontinuities in the velocity field were eliminated while preserving all velocity structures. Moreover, the computational cost is only a fraction of that of the boxcar filters shown in Figure 45.

5.2. 2D Paraxial ray tracing

The original formulation of the parabolic-paraxial wave theory was done by Leontovich and Fock (Leontovich and Fock 1946). The paraxial ray tracing is an asymptotic wave method,

which uses quantities (local wavefront curvature and spreading information) determined along a central ray via dynamic ray tracing, to evaluate approximately the seismic wave field in its vicinity rather than just on the ray itself (Cerveny et al. 1984). Another very similar method is the Gaussian beam method, which instead uses information from nearby rays, to approximate the wavefield in the vicinity. The Gaussian beam method generally requires of the order of ten beams, in which each beam support is a ray, to properly reconstruct the high frequency wave field (Nowack and Aki 1984; Beydoun and Keho 1987). In this respect, the paraxial method represents the limiting case of the Gaussian beam; it basically corresponds to an infinitely wide Gaussian beam (Cerveny et al. 1984; Beydoun and Keho 1987). However because the paraxial method can evaluate the wave field using a single ray, it is simpler and computationally more efficient. This efficiency does not come without a price, the Gaussian beam method is slightly more accurate in critical regions (e.g., caustics, shadow zones), and therefore offers an advantage whenever sources/receivers are in such regions (Beydoun and Keho 1987). Having said that, the Gaussian beam method still does not provide an exact solution in such regions and will not be able to correctly compute the Green's function in these complicated regions because it also relies on the validity conditions of the dynamic ray method (Keho and Beydoun 1988). The mathematical founding of the paraxial method is beyond the scope of this thesis, but a full description of the method with numerous references and applications can be found in Cerveny et al. (1984), Beydoun and Keho (1987), Keho and Beydoun (1988).

Travel-times can be computed with high accuracy by shooting multiple rays at different takeoff angles, with a certain angle increment, and let the paraxial method evaluate the Green's functions between the origination of the fan and every other point in the medium. Increasing the density of the ray fan boosts the accuracy of the computed travel-times, but also increases the computational cost. Despite this increased computational cost, it is still a fraction of the cost associated with two-point ray tracing, as typically there are hundreds of thousands if not millions of imaging points, and performing two-point ray tracing between each imaging point and each source/receiver becomes prohibitively expensive. Beydoun and Keho (1987) demonstrated the paraxial ray method is also faster (approximately an order of magnitude) than using a polynomial for interpolating the travel-times from a fan of rays shot using a dynamic ray tracing method. This makes the paraxial ray tracing method

ideal for imaging problems in heterogeneous media where many computations of the Green's functions are required.

Keho and Beydoun (1988) implemented a paraxial ray Kirchhoff migration. However, because of the disadvantage of the paraxial method in regions of complex velocity, their implementation requires a velocity model with no such regions (Keho and Beydoun 1988). In order to properly handle this issue, the ray-tracing algorithm implemented here will make use of an eikonal solver to perfect and refine the travel-times in those regions. This implementation is adapted from subroutines originally written by Zhenyue Liu from the Center for Wave Phenomena at the Colorado School of Mines, as part of the Seismic Unix processing package and are publically available at their website.

This implementation was designed to be simple to use and user friendly, it was also designed to run in single thread or in parallel, giving it the possibility to take full advantage of multiple processors and multicore processors at the same time. The efficiency of the code was also improved by rearranging some of the loops and minimizing subroutines calls. The part of the code responsible for handling different recording surfaces (including rugged topography or OBS case) was completely re-written, and now uses elevation values from each trace header to build the recording surface. The flow implemented (Fig. 47) requires the user to feed to the Paraxial ray-tracing processing step with: 1) a uniformly sampled velocity field in units of depth (lateral increment and vertical increment can be different from each other); and 2) a pre-stack seismic file, which contains the positions of all sources and receivers.

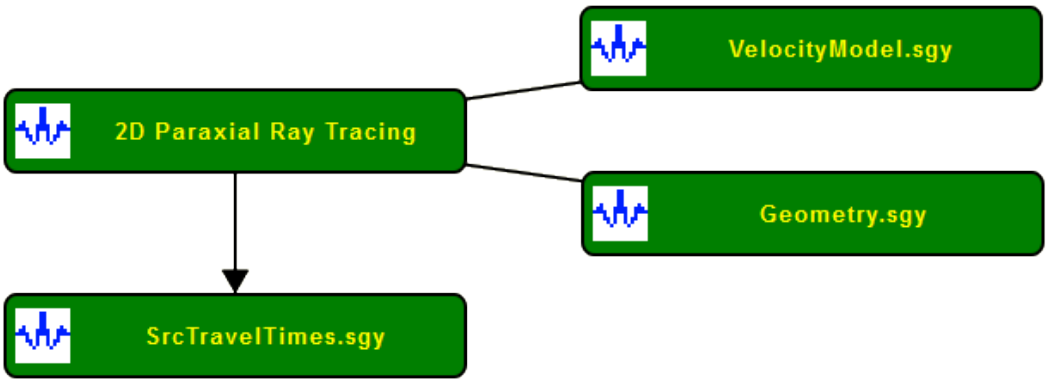

Figure 47 - The processing flow implemented for ray tracing. To the right are the velocity field and the pre-stack seismic data. The output is a file containing the travel-time maps.

The user interface implemented for the 2D Paraxial ray-tracing tool (Fig. 48) is divided in three parts. In the ray tracing parameters section, the user can set the vertical resolution (or sample interval) of the computation as well as the maximum number of samples; this allows the user to constrain how far the wave propagation should be simulated. The user can also control the ray fan by setting the takeoff angle and the takeoff angle increment parameters as well as controlling the ray emergence angles to be considered. The eikonal solver is proposed as an optional step to make-up for shadow zones. The user then choses to run either a source or a receiver ray tracing from the source/receiver parameters section. Depending on the choice, the program scans the pre-stack data and finds all sources/receivers with their corresponding positions, and outputs a travel-time table for each source/receiver as a separate record. In the case of a rugged topography or OBS data, which is the main concern of this thesis, the user can define the recording surface from which the rays will be shot. For rugged topography, it corresponds to the terrain elevation in which the geophones were planted, and in the case of OBS data, it will correspond to the bathymetric depth. The last section in the user interface is optional for those who would prefer to have the travel-time tables output with a different geometry.

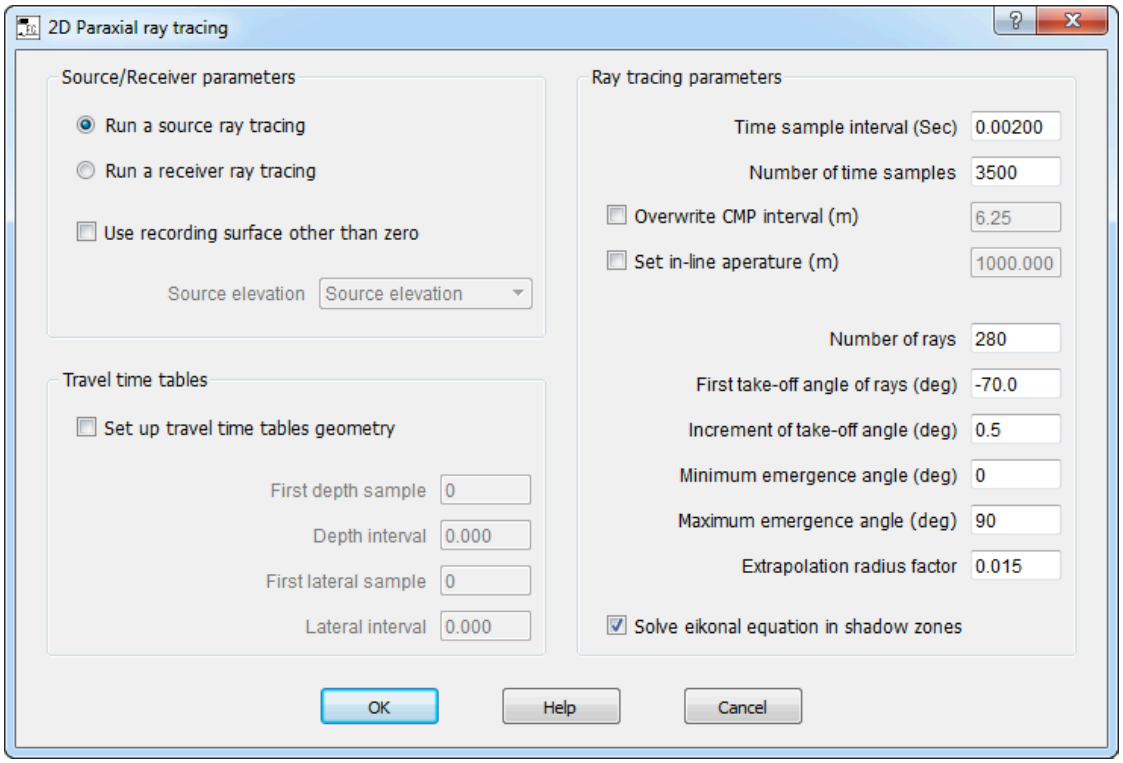

Figure 48 - Screen shot of the user interface implemented for the 2D Paraxial ray-tracing tool.

We have built a simple layer cake velocity model to use for a first test of the paraxial method (Fig. 49). The model mimics a calm sedimentary deposition basin and a marine acquisition scenario with a water column of about 2000 meters with a velocity of 1500 m/s. The velocity increases gradually over the rest of the model to reach a maximum of about 5000 m/s.

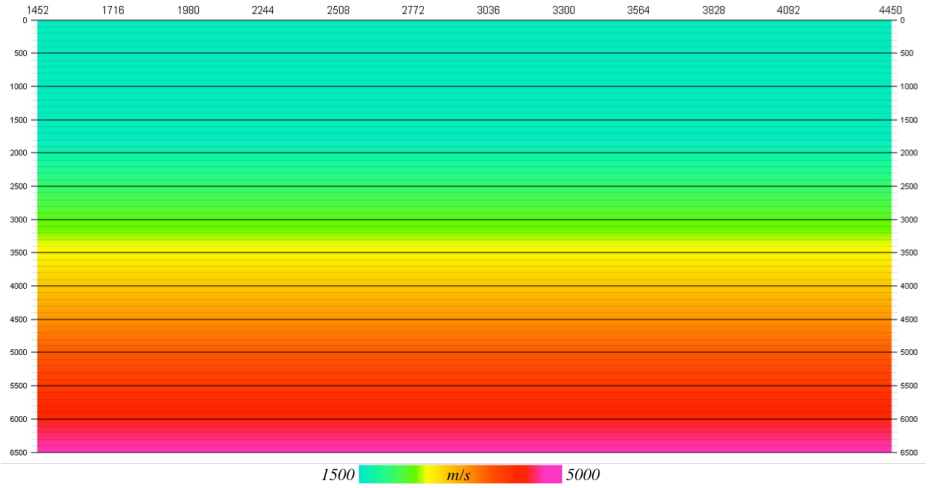

Figure 49 - Simple interval-velocity model as function of depth, mimicking a calm sedimentary basing.

Multiple source locations were ray traced with a ray fan starting from -70 to +70 degrees, with a half-degree angular increment. All emergence angles were considered (0-90 deg.). For convenience, we will only show the travel-time map at a single source location located at about 10000 meter offset in the middle of the velocity field (Fig 50).

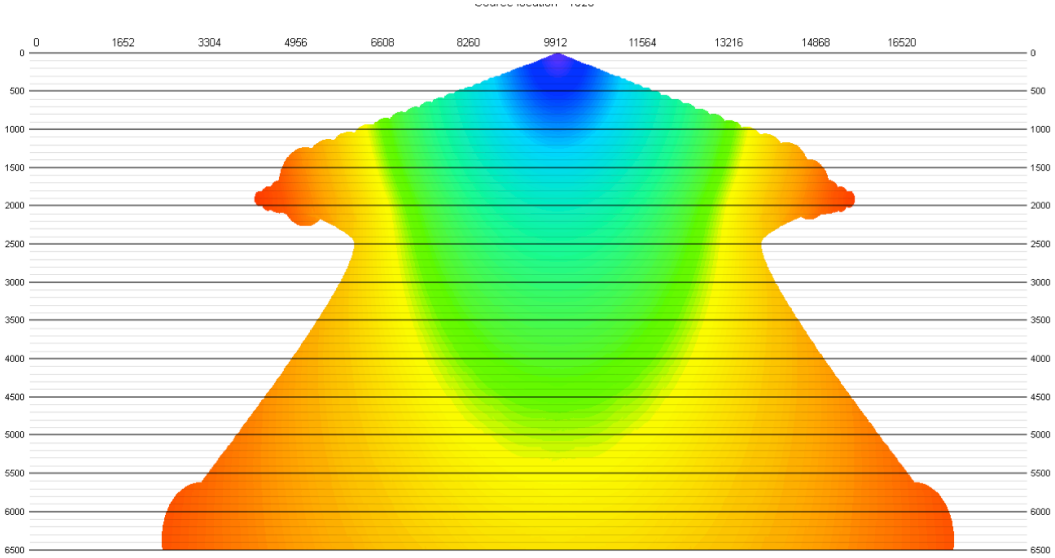

Figure 50 - Travel-times computed over the velocity field shown in (Fig. 49). The color scale highlights travel-times ranging from 0 to around 3800 milliseconds.

The reason we chose to show a source location in the middle of the velocity field, is to highlight the symmetry effect on both sides of the source location. This is due to the velocity model being laterally homogeneous and with only one axis of variability, the vertical axis. The strongest interface (water/sediment) in this velocity model can be easily seen in the arrival times. A more complex velocity model with two axes of variability would produce a more complex travel-time map; we should be expecting an asymmetric shape reflecting shorter travel-times in regions of higher velocity.

The next example in Figure 51 shows the kind of heterogeneities that we may be dealing with; the same geometry was used to build a synthetic velocity model with multiple fault-like features and complex velocity regions (Fig. 51). In this example, we will evaluate the advantages of smoothing velocities before ray tracing and the DLS smoother will be put to the test.

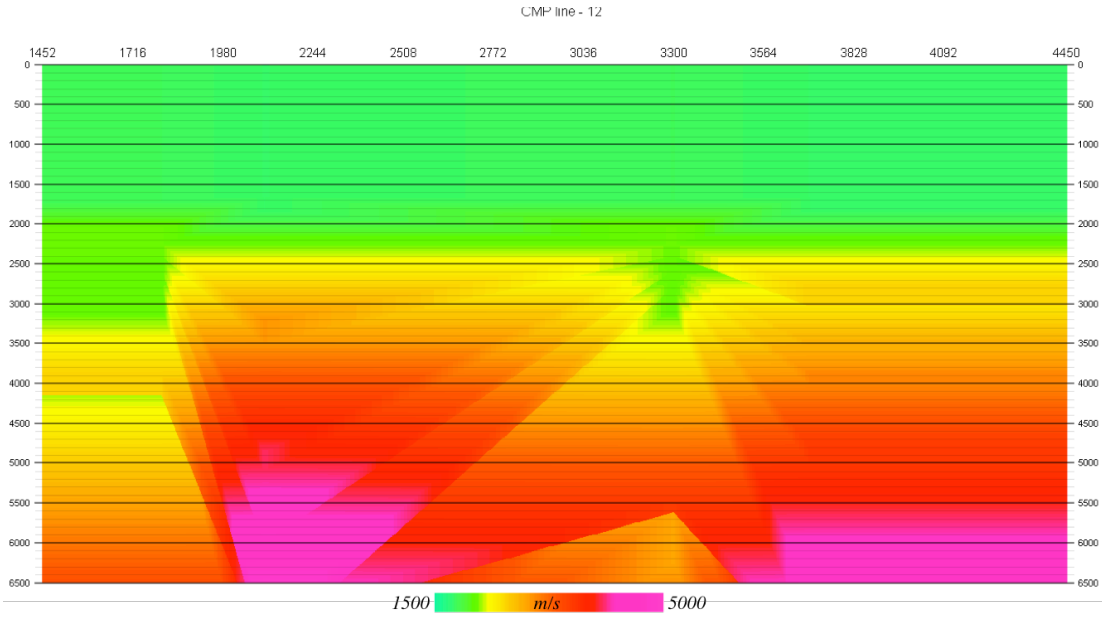

Figure 51 - A complex interval-velocity model as function of depth, with no smoothing operator.

The first part of the experiment is to compute the travel-times of a source location corresponding to CMP location 2800 (Fig. 52). The resulting travel time map (Fig. 52) clearly illustrates the asymmetry in the wave propagation and highlights some shadow zones where rays failed to emerge (black circles in the figure).

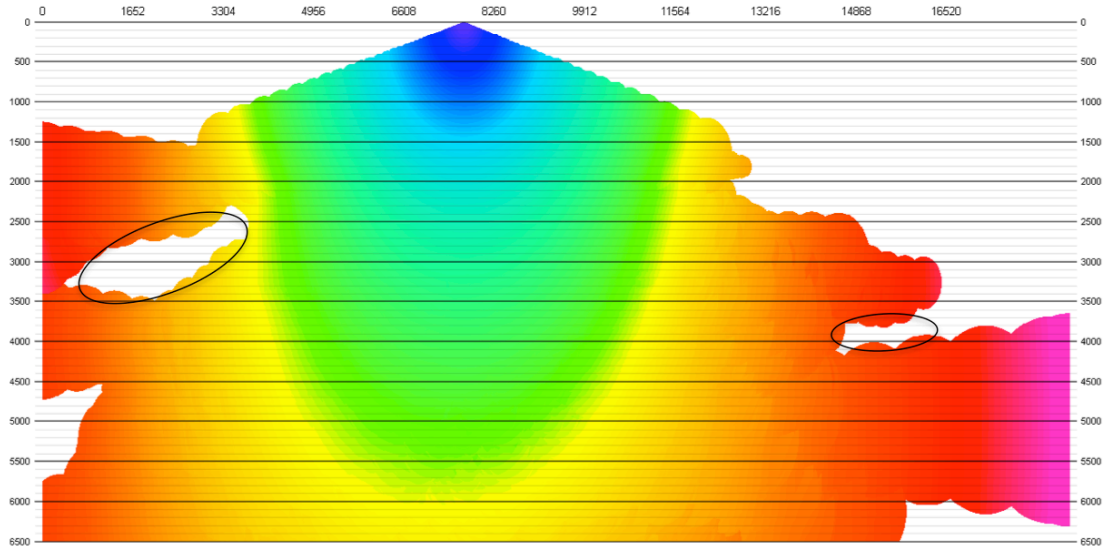

Figure 52 - Travel-times computed over the velocity field shown in (Fig. 51). Travel-times range from 0 to around 5000 milliseconds. The two black circles highlight some shadow zones.

The second part of the experiment is to smooth the velocity model shown in (Fig. 51) and compare the ray tracing result before and after the smoothing. The smoothing operator used here is the DLS smoother with an operator of size 20x20. The smoothed velocity model is given in Figure 53, for ease of comparison the same color scale is used.

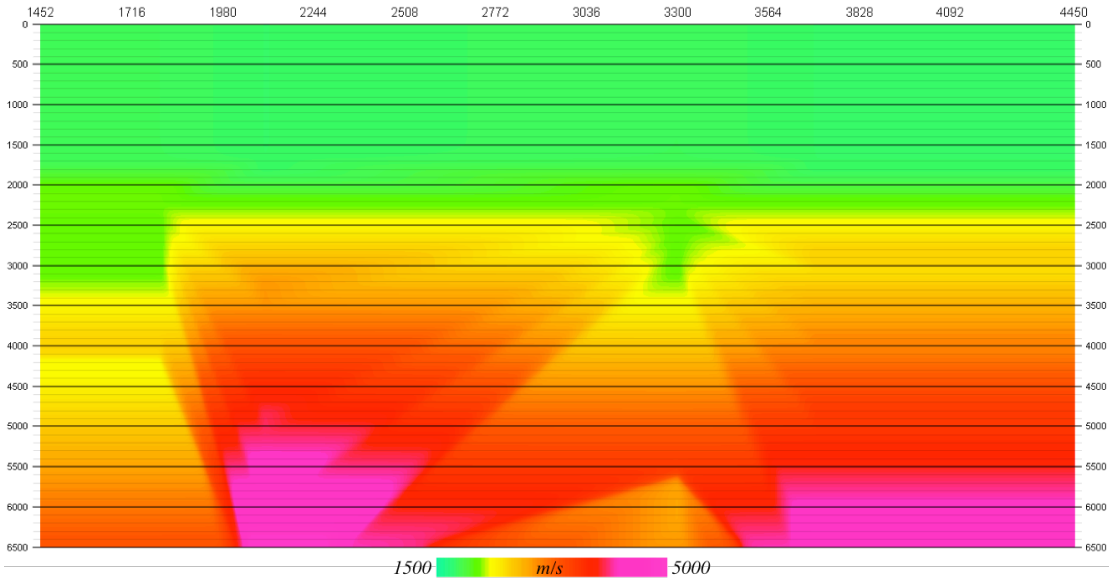

Figure 53 - The same velocity model as shown in (fig. 51) smoothed with a 20x20 DLS filter.

Ray tracing was run a second time with the same parameters used in the first part of the experiment; Figure 54 shows a comparison of a part of the travel-time map with and without smoothing.

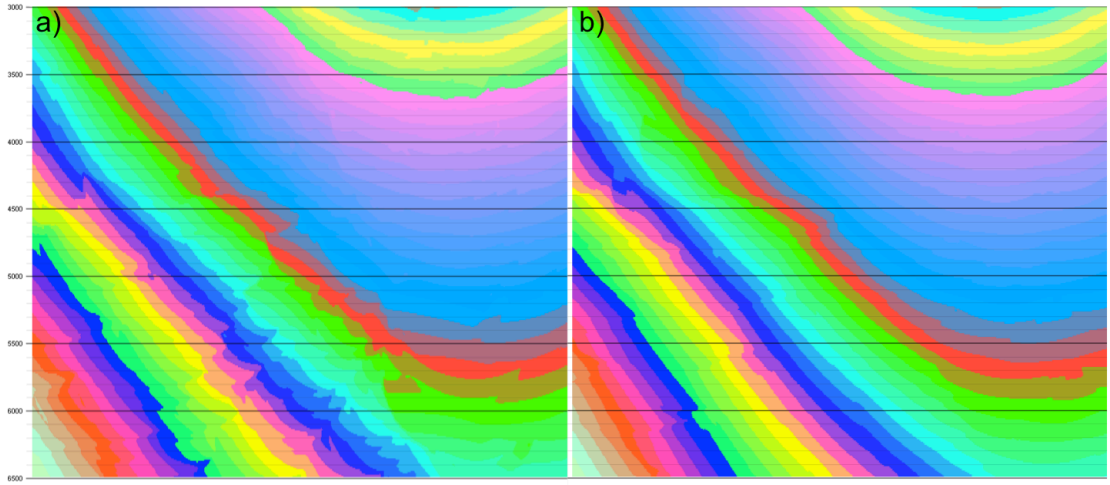

Figure 54 - Comparison between the travel-time maps with a) unsmoothed versus b) smoothed velocity.

Figure 54 was created using a different color scale from the previous travel-time maps in order to create a contour-like effect. Also, the gain of the image was adjusted in a way that helps to evaluate the smoothness of the computed travel-times. Therefore, one should not think of this image as absolute value of travel-times but rather as a relative tool for comparison. The travel-time in the raw velocity model (Fig. 54a) show abrupt changes and discontinuities in the arrival time value at multiple places. This is due to the sharp changes in the velocity field. On the other hand, when the velocity model was DLS smoothed (Fig. 54b), most of these discontinuities disappeared or were at least diminished. A larger smoothing operator would have resulted in a completely smooth travel-time map; the tradeoff here is to find the operator size reducing these artifacts in the travel-time map without completely redefining the original velocity structure.

To put things in perspective, we should look at the travel-time maps in fig. 50 and 52 versus simply using the DSR equation for the computation of the diffraction hyperbola. This illustrates the superiority of the depth migration. The DSR equation uses RMS velocities, which only honor velocity changes in the vertical axis, as discussed in chapter 2. Also, the DSR equation does not handle caustics or shadow zones, and does not constrain any incident or emergent angles (a caustic is a curve or surface to which each of the reflected or refracted rays is tangent. An example of caustic from daily life is when light shines through a drinking glass, the glass casts a shadow, but also produces a curved region of bright light; the caustic in this case, is that patch of concentrated light). The DSR simply incorporates offset, depth, and vertical velocity gradient. Thus it produces travel-time maps even more

simplistic than the one shown in Figure 50 regardless of the complexity of the velocity model. This is exactly why it cannot produce high quality images in complex geology, but works reasonably well in simple and calm sedimentary basins scenarios. Another point which should be stressed is that depth migration will not always lead to better imaging. In fact, accurate velocity modeling is a key factor, and without an accurate velocity model, it is not possible to take full advantage of depth migration.

5.3. 3D Finite Difference travel-time computation

Ray tracing techniques were typically the method of choice for computing travel-times of seismic waves. Nevertheless, wavefront tracing was known to be a powerful and accurate tool in this regard. Graphical methods devoted to wavefront tracing were first proposed by Thornburgh (Thornburgh 1930), but a general numerical implementation was only proposed in the late eighties (Vidale 1988). Vidale's method was based on a finite difference approximation of the eikonal equation, and quickly opened the way to numerous studies addressing the same question, notably the work done by Qin *et al.* to improve upon Vidale's original algorithm (Qin et al. 1990). These algorithms however, encountered serious difficulties when applied to models containing sharp velocity contrasts (Qin et al. 1990; Podvin and Lecomte 1991).

The method implemented here was first proposed in 1991 by Podvin and Lecomte, and was improved and stabilized over time. This method relies on the application of Huygens' Principle in the finite difference approximation. That is, every point reached by a wave becomes a secondary source; the sum of these secondary waves determines the form of the wave at any subsequent time. This method is capable of dealing with step velocity contrast as high as 1:10 regardless of the sharpness of the velocity anomaly. A general description of the method and why it can accommodate sharp velocity contrast will follow, but a more detailed discussion of the method with accuracy tests and performance benchmarks can be found in the original paper (Podvin and Lecomte 1991).

The eikonal equation describing wave propagation in the single dimensional case can be written in a very compact way as:

$$\left(\nabla t(x)\right)^2 = s(x)^2 \qquad (5.3)$$

Where *s(x)* is the slowness of the medium and *t(x)* is the arrival time of a wavefront at point *x*. This can be understood as propagating a wavefront (represented as isochrones) through the velocity model, rather than rays. Vidal's approach relied basically on solving this equation. His algorithm fails in contrasted velocity models because solving equation 5.3 consists in mathematically propagating a single wavefront, whereas in reality, multiple locally independent wavefronts originating from localized secondary sources (diffractions points) might be propagating in the medium to reach any point (Podvin and Lecomte 1991). The algorithm developed by Podvin and Lecomte (1991), used here, surpasses the idea of simply approximating the eikonal equation using finite difference to systematically considering multiple arrivals from several independent wavefronts and then picking the first arrival. This way, discontinuities in the travel-time field (e.g. caustics) are explicitly handled, although they might not be seen mathematically as regular solutions of the eikonal equation. In addition, this algorithm takes into account different modes of propagation, namely transmitted and diffracted body waves plus head waves.

The propagation takes place in a uniformly discretized model of the slowness, and the accuracy of the approximation depends mainly on the grid spacing. The grid spacing should actually be chosen according to the signal wavelength (conventionally an order of magnitude smaller than the signal wavelength), or in more practical terms, should be smaller than the size of the slowness anomalies to be considered.

In the implementation we produced in this thesis, the original "C" code developed by Podvin from the Paris School of Mines, was redesigned into a "C++" object oriented code reducing some of the subroutine calls. It was also made to run in single thread or in parallel, computing arrival times for each source/receiver with a separate thread. All operations on the velocity model, including the new options for handling non uniformly sampled velocity models, were taken out of the main program loop to avoid wasted computational effort.

The flow used for the 3D finite difference computation of travel-times (Fig. 55) looks very much the same as the one used for the 2D paraxial ray tracing (Fig. 47). In fact the user still

has to feed to the travel-times computation step the velocity model and the pre-stack seismic file containing sources/receivers positions; the only difference is that here the velocity model has to be a 3D file with predefined geometry (inline/crossline spacing, bin size in both directions, etc.)

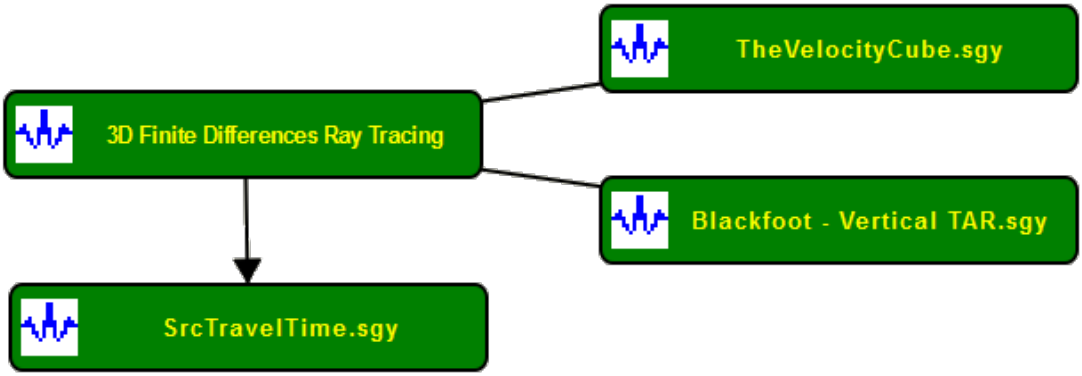

Figure 55 - The processing flow used for 3D finite difference computation of travel-times. To the right are the velocity field and the pre-stack seismic data. The output is a file containing the travel-time maps.

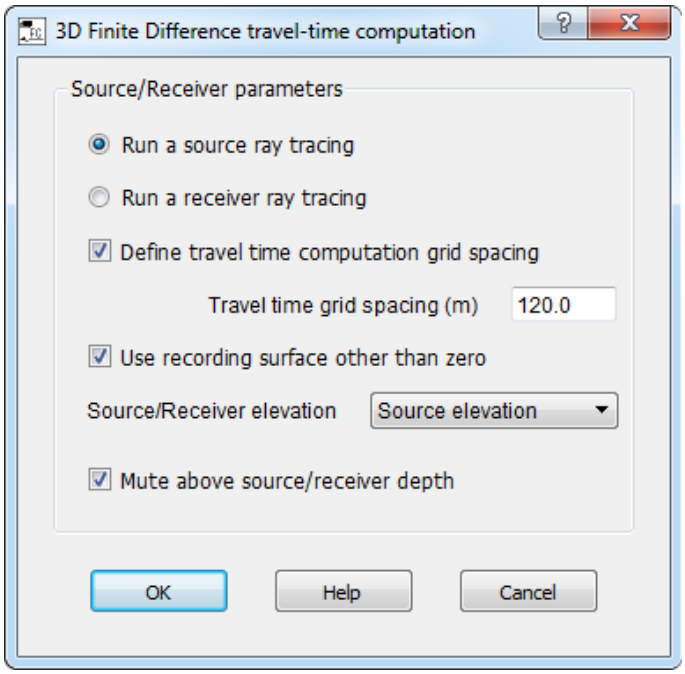

Figure 56 - User interface of the 3D finite difference travel-time computation step implemented in the scope of this thesis.

Concerning the user interface (Fig. 56), it was designed to be as simple as possible. The user has only four options to configure: 1) whether to compute travel-times originating from

sources or from receivers; 2) the grid spacing - this option should be used in two case: if the velocity model is not uniformly sampled, in which case the program will first start by regularizing the grid with the chosen grid spacing, or in case the user wants to increase/decrease the grid density in order to boost accuracy or to save some computation time (needless to say that increasing the grid spacing will reduce computational cost but also reduces the accuracy); 3) setting up the recording surface - again this is useful for rugged topography scenarios and OBS acquisition cases; and 4) to mute above the source/receiver elevation.

To test the 3D finite difference travel-time computation algorithm, we used a 3D field dataset acquired in "Blackfoot – Canada" and ran a velocity analysis tool to generate multiple velocity functions at different bin locations. The velocity tool implemented, presented in figure 42, was used to generate the 3D model of interval velocities as function of depth (fig. 57), with a grid spacing of 30x30 meters in inline and crossline directions and 5 meters spacing in the vertical direction. The velocity model was generated with the option to extend the velocity field to cover all source/receiver locations; in this case, it covers an area of about 10 km^2 and is 9 km deep.

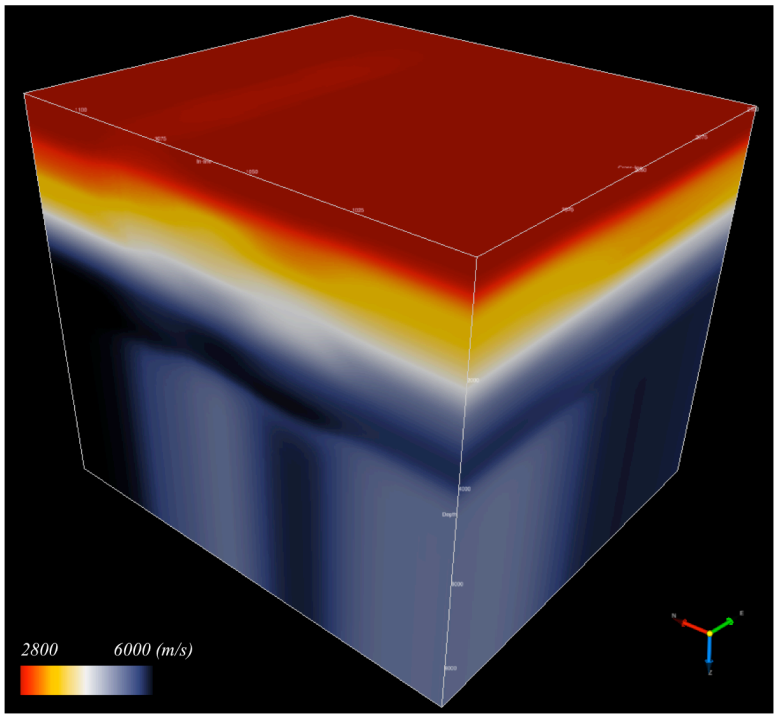

Figure 57 - 3D velocity model for testing the 3D finite difference travel-time computation tool.

The 3D travel-time computation was run for all sources with 30 meters grid spacing. For convenience, the 3D travel-time map of a single source will be shown; the source is located right in the middle of the area at the surface (Fig. 58).

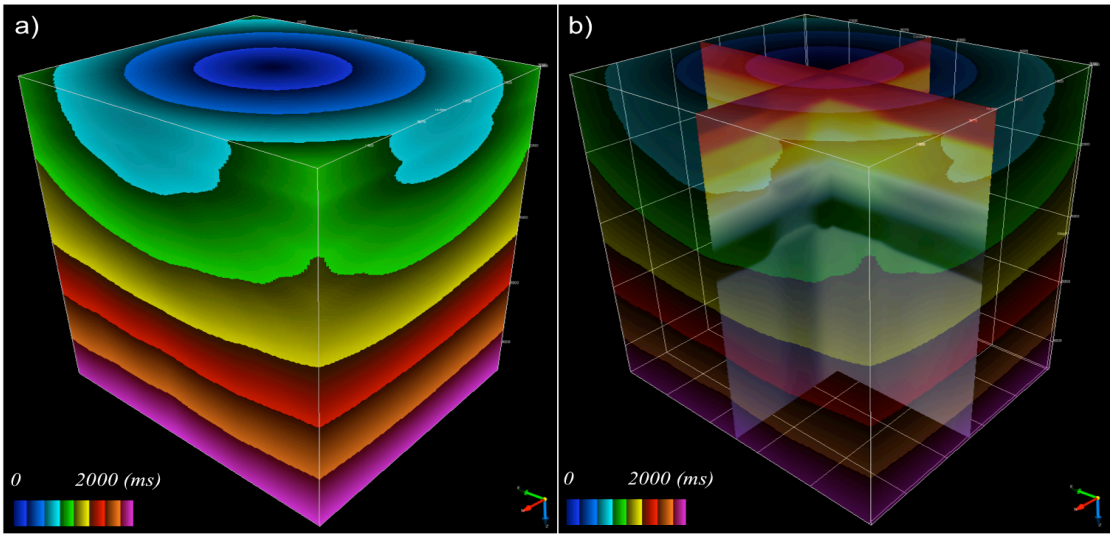

Figure 58 - a) 3D travel-time map computed using finite differences; b) with a transparency effect and superposed on the inline/crossline velocity field.

The travel-times map in figure 58 follow the velocity model; changes in the shape of the wavefronts (isochrones) can be directly correlated with the different structures in the velocity model. The travel-time cube can then be sliced in several ways to highlight different aspects regarding velocity structure and wave propagation. Depth slices of the travel-times (Fig. 59) can reveal information about lateral continuity of complex geological structure (e.g. graben horst, faults, etc.); however these structures will only be visible if their size is bigger than the resolution of both the velocity model and the grid spacing of the travel-times.

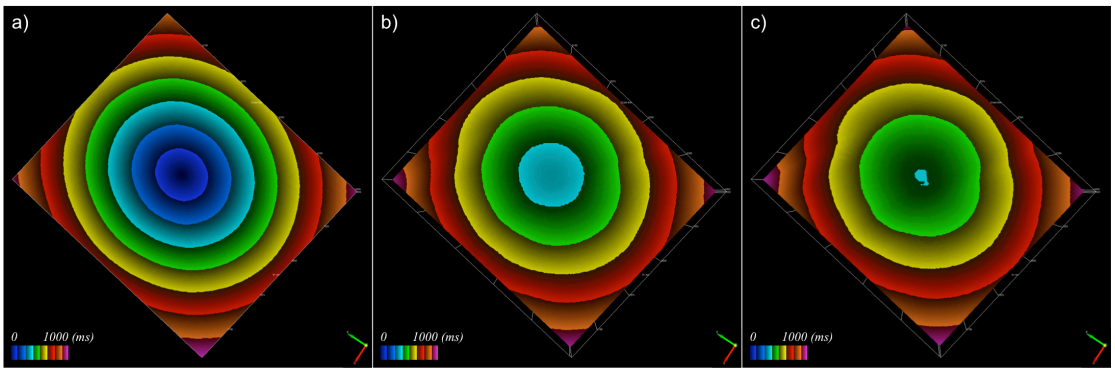

Figure 59 - Depth slices of the travel-time cube shown in (Fig. 58). a, b, and c are at increasing depths.

Comparing results from the paraxial ray tracing method (Fig. 50 /52) and the 3D finite difference solution of the eikonal equation (Fig. 58 / 59), it is easy to conclude that solving for wavefronts instead of rays overcomes the problem of shadow zones and can provide information about the time of the first arrivals in these geologically complex areas.

5.4. Pre-stack depth migration implementation

The pre-stack migration algorithms implemented in the scope of this thesis act on source gathers rather than common offset sections, which inherently cope with irregular 3D surveys where it is not always possible to get consistent common offset sections. Also, the algorithms implemented here can handle OBS, streamer and land data. The implementation can run on a single thread or in parallel. The biggest challenge for implementing such a method in parallel is the size of the travel-time files and the time used by each thread to read these files. We use lookup tables to solve this problem and share the lookup tables between different threads.

The flow for running the depth migration is similar in both 2D and 3D cases (Fig 60); the input data are the shot gathers with geometry information and all pre-migration processes applied to it. Two auxiliary files input the sources and receivers travel-time tables to the step. And the output file is the migrated shot gathers.

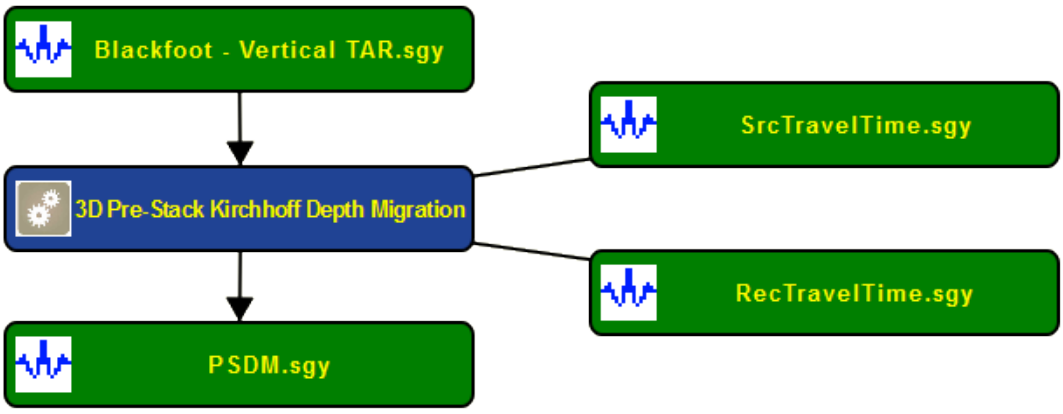

Figure 60 - The processing flow implemented for 3D pre-stack Kirchhoff depth migration.

The user interface of the depth migration step is quite simple (Fig. 61). The user has first to select the dataset type - streamer and land data require shot gathers but OBS data will

require receiver gathers. The migration limits constrain offset and dip of the diffraction hyperboloid. The amplitude correction and anti-aliasing filtering will be discussed in the next paragraph. The migration grid parameters are simply setting the output depth parameters.

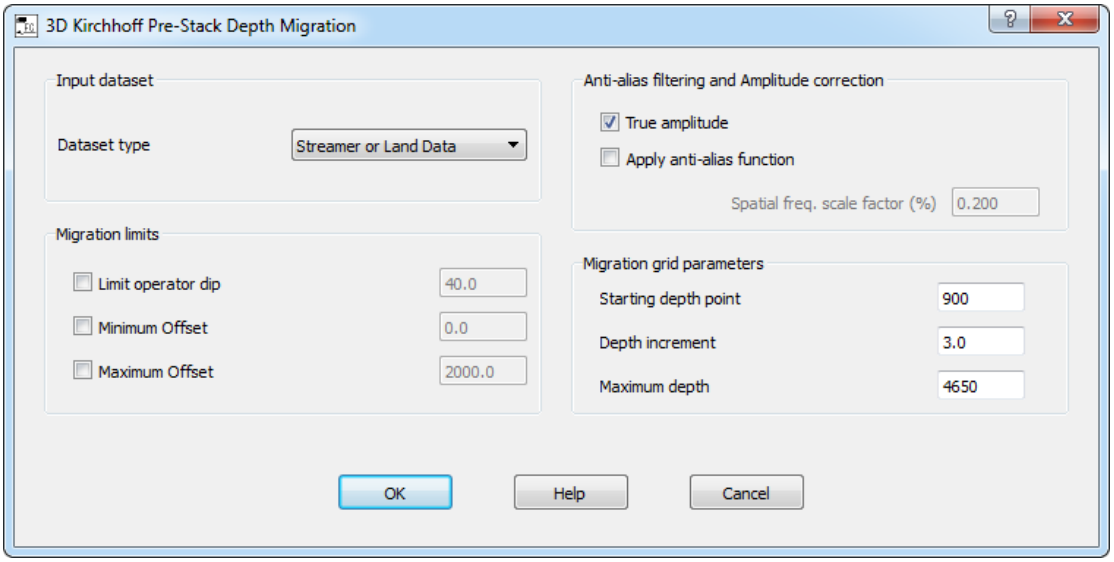

Figure 61 - User interface of the 3D pre-stack Kirchhoff depth migration step implemented.

The migration output assigned to a given imaging point "*I*" is obtained by summing the amplitudes of the input seismograms along the diffraction surface. This surface will usually cross the input seismic trace between samples as illustrated in Figure 62.

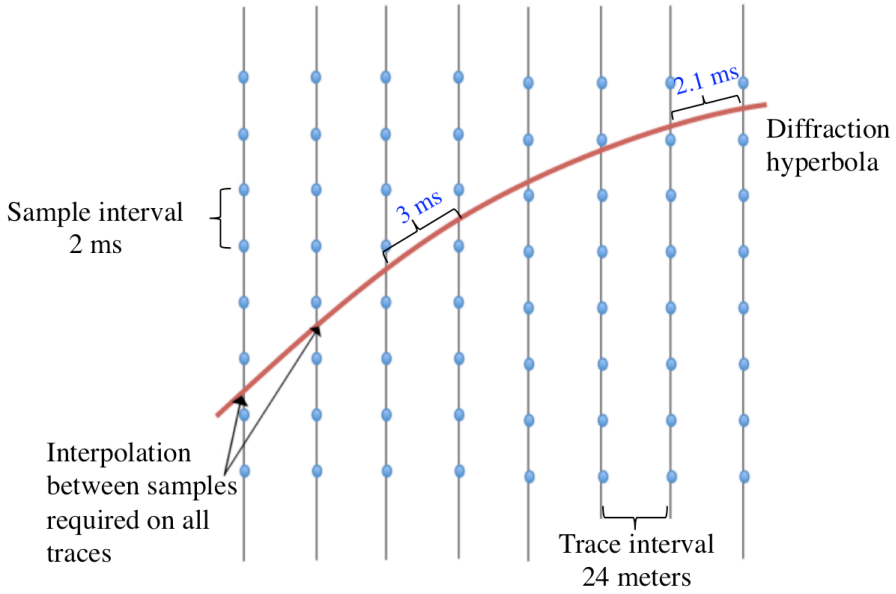

Figure 62 - Part of a diffraction hyperbola illustrating the need for interpolation and anti-aliasing.

As shown in Figure 62, interpolation between samples is usually required. Interpolation results in an alteration of the frequency content of the data. Two major risks are associated with this interpolation; the first is losing high frequencies; the second is interpolating higher frequencies than what the sampling rate of the input seismic traces can justify. The Nyquist sampling theorem explains the relationship between the sampling rate and the frequency of the measured signal. It simply states the sampling frequency (f_s) must be at least equal or greater than twice the highest frequency of the measured signal f_N, which means that the highest un-aliased frequency (also known as Nyquist frequency) is given by:

$$f_N = {}^{f_s}/_{2} \qquad (5.4)$$

To correctly handle the sampling aliasing, this implementation utilizes a band-limited interpolation using by default the Nyquist frequency associated to the sampling rate of the input data as frequency limit. This guarantees the migrated traces will not suffer from data-related temporal aliasing.

Although the sampling rate in the example shown in figure 62 is 2 milliseconds, the actual sampling interval along the diffraction hyperbola varies as a function of trace interval, velocity along the hyperbola and the diffraction dip. This causes what is called *migration operator aliasing* noise (Lumley et al. 1994; Abma et al. 1999; Bevc and Lumley 2001). The simplest method to reduce the operator aliasing effect is by limiting the operator dip. Limiting of operator dip results in only stacking samples up to certain dip where the sampling interval along the diffraction hyperbola is not much larger than the sampling interval of the samples along the seismic trace. The main drawback of this truncation is the removal of steeply dipping events from the migrated result, but it is definitely the fastest method to handle such artifacts.

The way this problem is handled in this implementation is by estimating the sampling interval along the diffraction hyperbola between each two adjacent traces, using velocity and geometry information, and recalculating a "local Nyquist frequency". The band-limited interpolations will then simply use this "local Nyquist frequency" as the band limit instead of the Nyquist frequency of the input seismic data. This process adds a significant overhead to the computation effort.

The term "true amplitude" migration means that the migration algorithm attempts to recover the reflection amplitude loss caused by geometric spreading so that the amplitudes represent the reflectivity (Lee et al. 2004). This is done by weighting the contribution of each trace to the imaging point. Implementing an exact amplitude weight function involves square roots of the cosine of the takeoff and emergence angles, and in-plane and out-of-plane spreading terms for every possible combination of source, receiver, and image point even for the relatively simple case of only vertically varying velocities (Dellinger et al. 2000). It also has to incorporate phase rotation when the wavefield energy encounters caustics (Zhang et al. 2000). The computation of such a weighting function is too expensive and dominates the total cost of the migration; but it also is not always beneficial as any error in migration velocity estimation will have significant effects on the calculation and yield possibly serious amplitude distortions of the migrated section.

Implementations of exact amplitude weighting functions are not practical given the large computational costs. Multiple cost effective estimations of the weighting functions have been developed to approximate the true theoretical functions. The weighting function algorithms mostly lead to fairly reasonable and comparable estimations of amplitude weight with a much smaller additional cost (Dellinger et al. 2000; Zhang et al. 2000; Jäger et al. 2003; Lee et al. 2004; Haibo et al. 2009). Based on to the work done by Dellinger et al. (2000) and followed by Zhang et al. (2000), we might be better off with a simplified amplitude weight using a *v(z)* medium than to try to implement an exact solution. Accordingly, the amplitude weight of each sample along the diffraction hyperbola in a shot-gather-depth migration is given by:

$$For\ 2D: \quad w = \frac{z}{v^2}\frac{1}{\sqrt{t_s * t_r}}\frac{t_s}{t_r} \qquad (5.5a)$$

$$For\ 3D: \quad w = \frac{z}{v^2}\frac{t_s}{t_r^2} \qquad (5.5b)$$

Where z is the depth of the imaging point, z is velocity, and t_s/t_r are respectively the time from the source to imaging point and from the imaging point to the receiver. Figure 63 shows how the amplitude weight changes with diffraction offset in a 2D example. The amplitude weight function shown here corresponds to an imaging point at a depth of 2700m below the source/receiver datum with a velocity of about 1700 m/s.

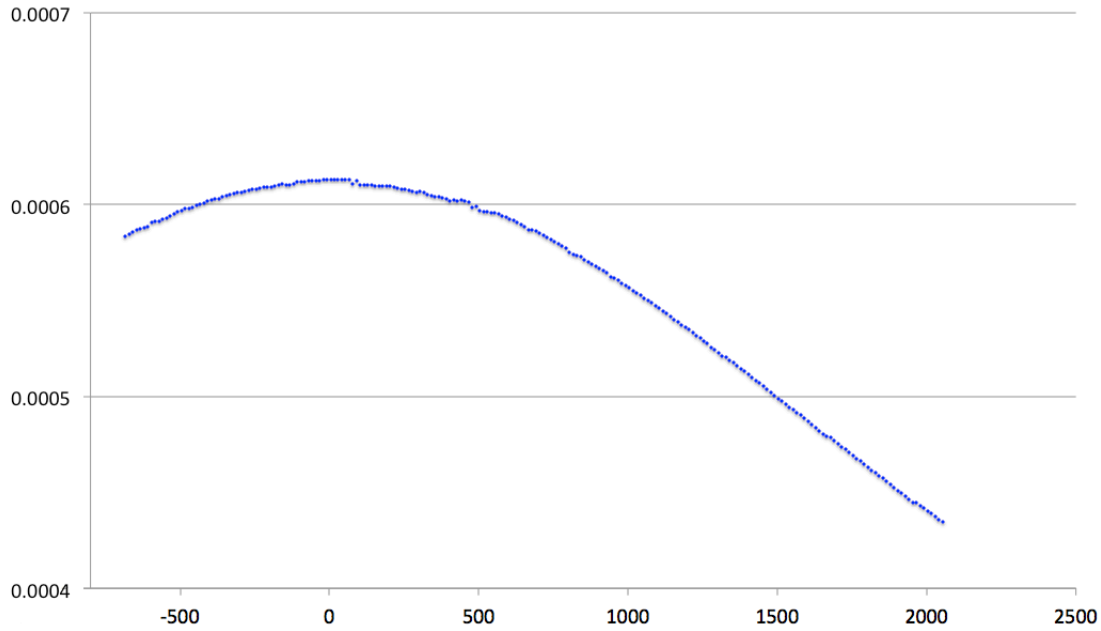

Figure 63 - Amplitude weight for a source gather depth migration as function of diffraction offset.

In order to test this pre-stack Kirchhoff depth migration, we will migrate a single trace on a shot gather. This is a very common tool to assess, validate, and compare different migration algorithm, as it easier to compare the migrated smiles rather than the whole section. Differences in the imaging quality in a seismic section are not solely related to the migration algorithm; they might be in fact just an artifact of the velocity model accuracy or of noise in the data.

5.4.1. 2D depth migration example

For this test, a single trace from an actual shot gather with 240 channels and 12.5 meters spacing was used and all the rest of the traces were zeroed. The trace to be used is in the middle of the gather to facilitate the comparison of the migration smiles. The migration results show the contribution of the single trace to the rest of the gather (Fig. 64).

The input data (Fig. 64a) is a seismic trace in TWT domain with no NMO correction applied to it; the migration process inherently corrects for the move-out. A velocity analysis was carried out on the original data to build a simple velocity model, including lateral velocity variations, which was then used for a pre-stack time migration followed by a time to depth conversion (Fig. 64b).

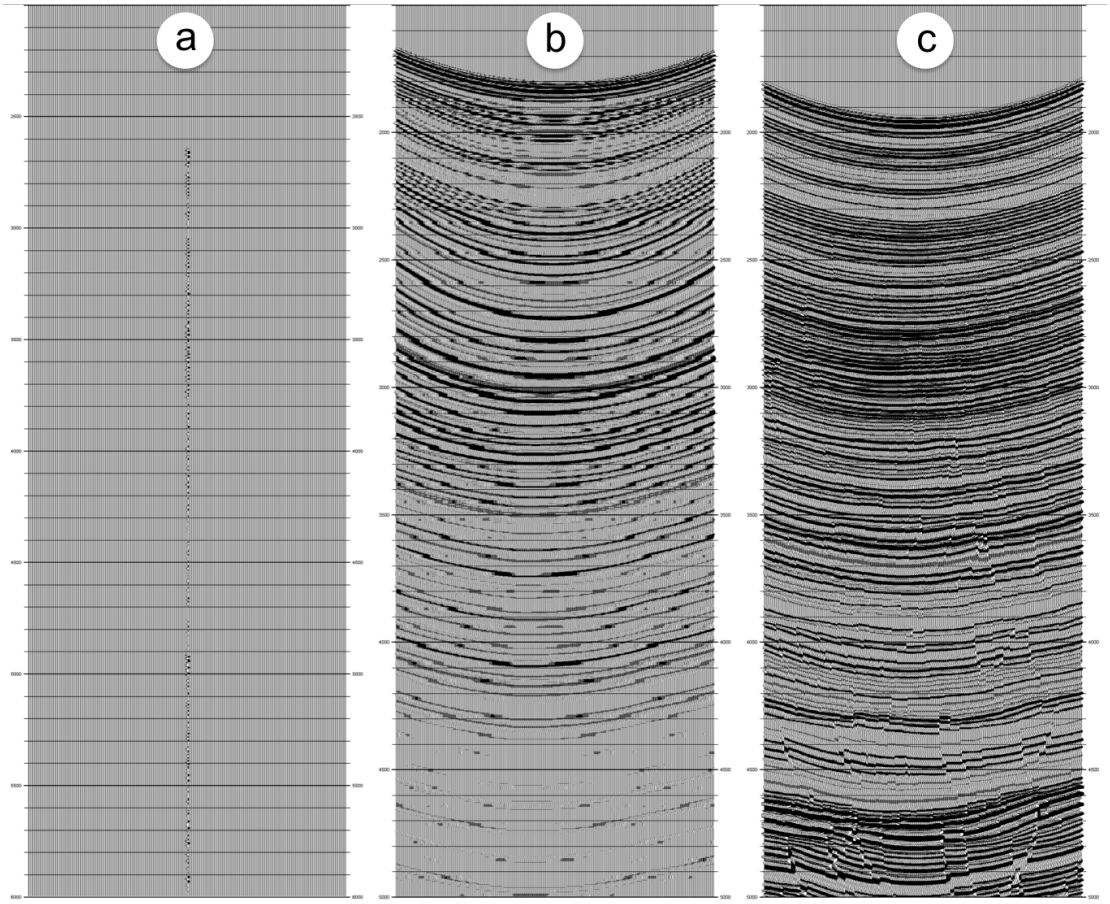

Figure 64 - 2D shot gather with a) a single live trace with two-way-time in the vertical access; b) pre-stack time migration of that trace followed by a time to depth conversion; and c) a pre-stack depth migration of the same trace. The vertical axis in b and c is depth. The horizontal axis in a, b, and c is the channel number.

The time to depth conversion was done trace by trace and was carried out using a single velocity function. For the depth migration (Fig. 64c), the Paraxial ray tracer discussed earlier in chapter 5.2 was used to compute the source/receivers travel-time tables using the exact same velocity model. The pre-stack depth migration algorithm used these travel-time tables to migrate the trace. Figure 64 illustrates clearly the superiority of depth migration over the time migration. In the depth migration case, the energy is summed over a more accurate diffraction hyperbola, and thus the migration smiles are more continuous and consistent. The depth migration also retains substantially more of the frequency content of the data; we can see much finer migration smiles, some of which did not even exist in the time migration. However, the depth migration with the paraxial travel-times has a drawback when the velocity model is not well estimated or suffers from severe discontinuities, which is the reason for the slicing-like effect we see in figure 64c. They are mostly present in the

lower part of the section and the multiple areas where the velocity analysis was not accurate enough.

5.4.2. 3D depth migration example

For 3D datasets, a shot gather consists of multiple receiver lines. The migration process will sum the energy along the hyperboloid diffraction surface going through all those receiver lines. In this example, a single trace was extracted from a 3D shot gather, by zeroing all traces but the trace in question just as in the previous example, and then migrated with the 3D pre-stack depth migration algorithm (Fig. 65).

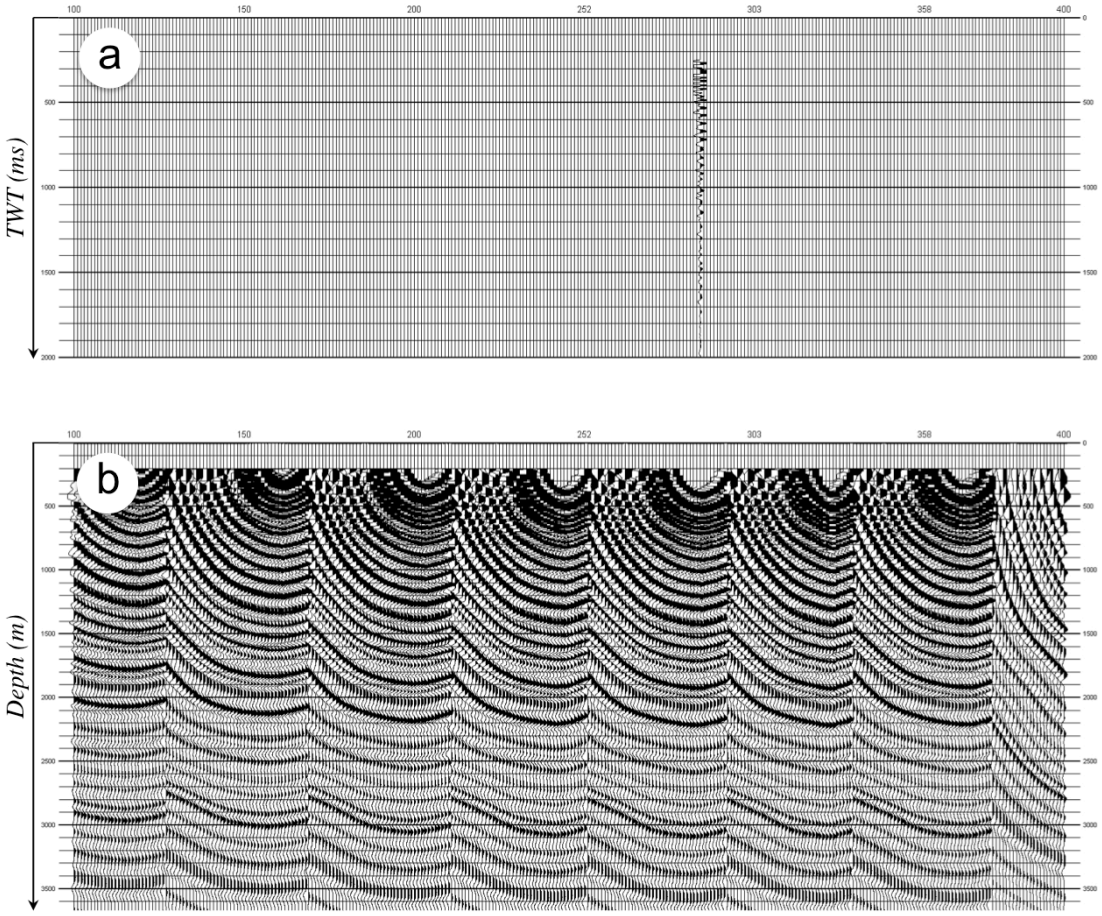

Figure 65 - 3D shot gather with a) a single unmigrated live trace, and b) a pre-stack depth migration of the same trace. The horizontal axis in both gathers is the channel number.

In this example the seismic grid is mostly regular except for a few gaps, which is one of the reasons why the migration smiles have some breaks and are not always smooth. The other

reason for discontinuities is simply because of the velocity structure. Compared to the migrated record in the 2D example, this one does not suffer from the slicing-like effect as the travel-times to construct the diffraction surfaces used in this migration were computed using the finite difference method rather than the paraxial ray tracing which can cope much better with discontinuities in the velocity structure as discussed in chapter 5.3.

5.5. Example of pre-stack depth migration of OBS data

The OBS data used in this example was acquired in the Gulf of Mexico and is the same data used in the positioning experiment (see Fig. 34). Velocity analysis was not performed; instead, a simple smooth velocity model was used to approximate the velocity structure of the sedimentary basin of the Gulf of Mexico area with velocities starting at 1500 m/s at the water/sediment interface and slowly increasing up to 3500 m/s at 5000 meters depth with a grid size of 50 meters. This velocity model is not accurate for imaging purposes, but it is sufficient for testing the migration algorithm.

Travel-time cubes were computed for the receiver and all sources using the "mute above source/receiver" option; this means that the migration algorithm will skip all imaging points above about 2000 m (the OBS instrument is located at a depth of 1962 meters). The travel-times were computed on a grid with a cell size of 100 meters.

The 3D pre-stack Kirchhoff depth migration was performed with a depth starting at zero, down to 5000 meters, with a depth increment of 3 meters, using the true amplitude weighting option.

The results of two migrated receiver gathers are shown in the figures 66 and 67.

The receiver gather shown in figure 66a illustrates a case where the sources are mostly to one side of the OBS location (similar to the streamer case). The migration (Fig 66b) enhanced the continuity of most of the existing events. Because the Kirchhoff migration scheme is in essence a smoothing filter, it did get rid of a considerable amount of incoherent noise seen in the data prior to migration. The yellow triangle in Figure 66b highlights the part of the data that suffered the most from the estimated smooth V(z) velocity model. It corresponds to large offsets and shallow depths. Figure 67 shows another

receiver gather before and after migration; in this case the sources are from both sides of the OBS instrument location.

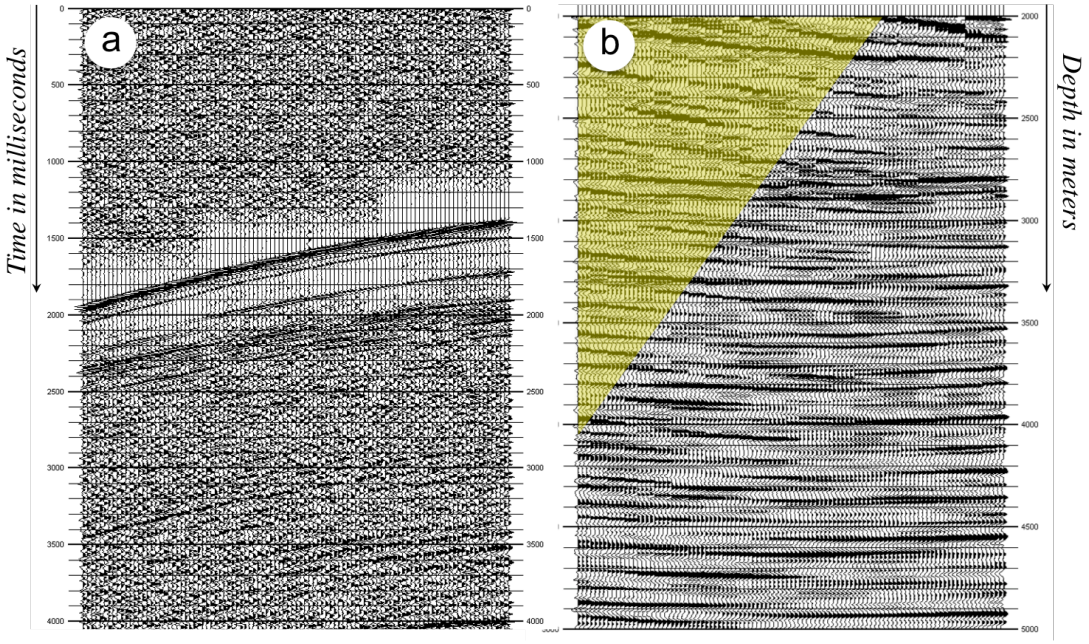

Figure 66 - OBS receiver gathers, a) unmigrated in time domain, b) 3D Kirchhoff pre-stack depth migration.

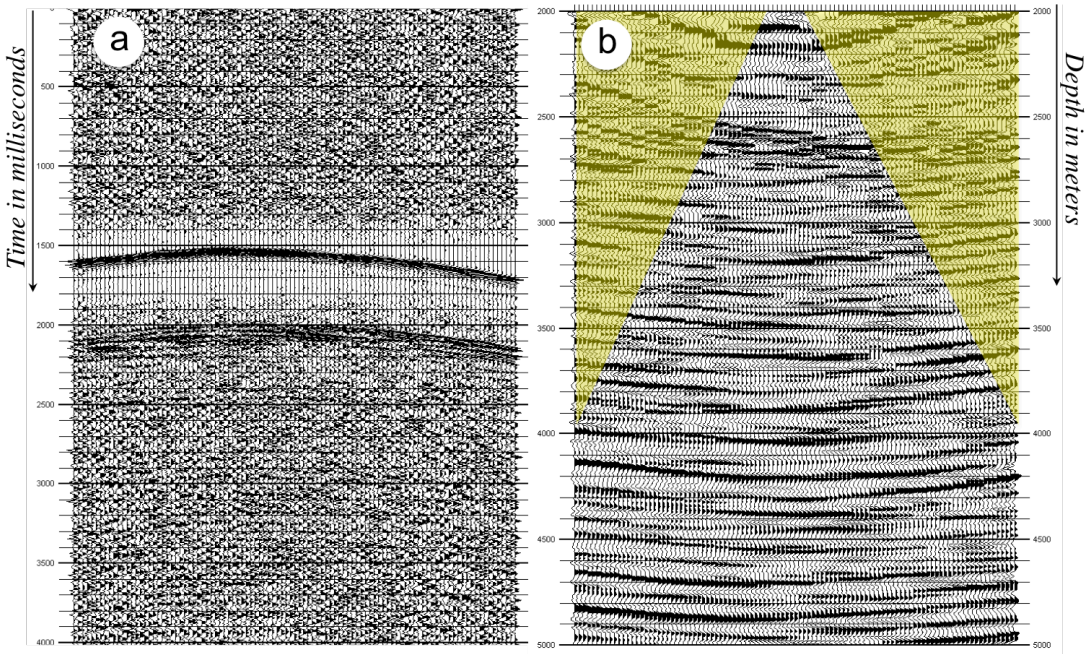

Figure 67 - OBS receiver gathers. a) Unmigrated in time domain, b) 3D Kirchhoff pre-stack depth migration.

In this case (Figure 67), the sources are shooting from both sides of the OBS (similar to land acquisition geometry). The only difference, compared to the example shown in figure 66, concerns the areas suffering the most from the erroneous velocity model; in this case they occur at both ends of the record (yellow triangles on Fig. 67b).

Longer offsets are more affected by the velocity model because the wavefront propagate through more lateral discontinuities to reach them. A correct velocity model will lead to accurate travel-time computation and thus all offsets but especially the longer offset data migrate more accurately.

5.6. Converted-waves

Until this point, we have been only migrating the P-waves energy from the OBS, which is still the primary method of hydrocarbon exploration. However, a primary reason for using OBS acquisition systems as discussed in chapter (1.2), is the capability to record S-waves energy. Multicomponent recording and analysis can generate complementary images when P-wave surveying fails, or reaches it limit. It has significant applications in the detection and monitoring of fluid content in the subsurface. In this section, we will introduce converted-wave exploration and processing.

In the context of hydrocarbon exploration, converted-waves refer to a particular conversion; a compressional P-wave propagating downward converting to a shear wave at the reflection point and propagating back upward (Fig. 68).

In figure 68, the incident angle and the reflection angle is the same in the P-wave reflection, but is different in the P-S converted wave case. Snell's Law describes this asymmetry:

$$\sin\theta/v_p = \sin\emptyset/v_s \qquad (5.6)$$

V_P and V_S are respectively P-wave and S-wave velocities. Generally, in consolidated sedimentary sections, the V_P / V_S ratio is approximately 2.0. As the Vs is less than Vp, the wave travels at a steeper angle on the upgoing path than the downgoing path. Due to unequal incident angles, the P-S conversion and P-P reflection points follow curved trajectories as shown previously in Figure 40.

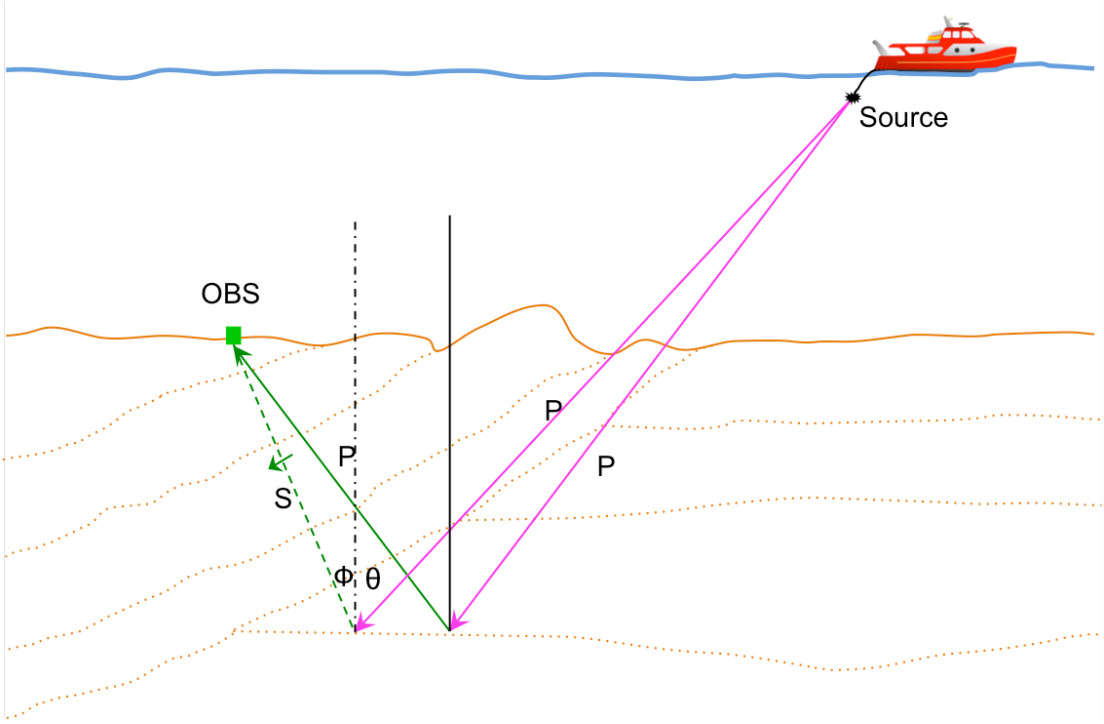

Figure 68 - A converted-wave (P-S) reflection at its conversion point compared to a pure P-wave reflection. The conversion point is shifted toward the receiver compared to the reflection point. Arrows show the senses of propagation.

The basis of any work with P-S exploration relies on a good estimation of shear wave velocity (Vs). One of the early ways to estimate Vs is by comparison of zero offset P-P and P-S reflection times. Once estimated, the analysis of Vp/Vs ratios can infer valuable information about lithology changes. Velocity analysis techniques are out of the scope of this thesis. We will assume all the velocity models used are pre-built.

P-S converted waves can be processed with similar processes as traditional P-P data. The input data in this case is the horizontal component seismic data. The same ray tracing or finite difference travel-time computation techniques are used with the P-wave velocity model to compute travel-time tables of the downgoing wavefield, and then with the S-wave velocity model to compute travel-time tables of the upgoing wavefield. The same implementation of the Kirchhoff migration is used to migrate the data.

Here we present results from P-P versus P-S migrations from literature, as we did not yet have access to data that could be migrated with our algorithm, which works both for P and S-wave data. Figure 69 shows a comparison of P-P section versus P-S section. This migration was done by Pedersen et al. (2010).

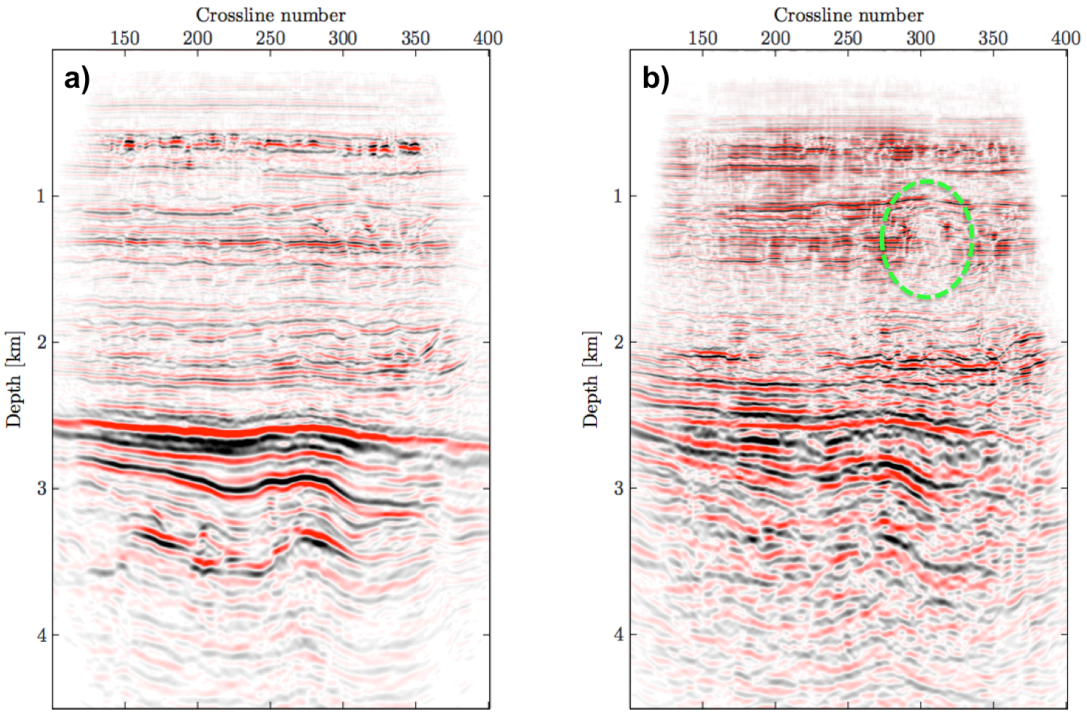

Figure 69 - A 2D section extracted from a 3D OBS data. a) 3D migrated using P-P energy; b) 3D migrated P-S energy; the green circle highlights discontinuous events that might be associated to fluid presence (modified from Pedersen et al. 2010).

Looking at the imaging results shown in Figure 69, we can conclude that the velocity model used in both migrations was well estimated because both images correlate well in depth. In general, both migrations delivered satisfactory results, but the P-P image has better reflector continuity, especially in the deeper part. The green circle highlights an area where the shear wave image shows a clear discontinuity, which might be associated to the presence of fluids.

In OBS acquisition projects, the aim is to produce two images of the subsurface, one using the P-P energy and the other is using the P-S energy, which will enable estimation of elastic parameters. The interpreter uses both for identifying and characterizing faults and areas with fluid content. In 4D seismic, monitoring the size of the discontinuous reflectors over time is used to estimate reservoir' fluid content evolution.

5.7. Conclusions

The migration of OBS data using the Kirchhoff method is best achieved via depth migration instead of time migration. The integrated depth migration tool implemented in the scope of this thesis is capable of handling OBS data as well as conventional streamer

and land data. For its calculation, velocity functions have to be interpolated into a uniformly sampled grid, extrapolated to cover all source/receiver positions, and smoothed to soften any sharp velocity contrasts. The paraxial ray tracing method was implemented for the 2D case, while for the 3D case a finite difference method was used to solve the eikonal equation and compute travel-times. The travel-times tables were then fed to the prestack Kirchhoff depth migration algorithm together with the prestack seismic data to run the migration. The migrated source gathers, or receiver gathers in the OBS case, have to be stacked in the CDP domain to build the migrated image.

For P-S imaging of OBS data the user has to build two velocity models: one with pressure wave velocity (Vp), and the other with shear wave velocity (Vs). Travel-times originating from source wave propagation through the model are to be computed using Vp, while those corresponding to the receivers are computed using Vs. The rest of the procedure is identical to the P-P imaging.

Chapter 6

Conclusions and future work

6.1. Main conclusions

In the scope of this thesis, it was possible to identify three main issues in the processing of 3D Node data: 1) random internal OBS clock drifts; 2) accurate OBS positioning; 3) computationally effective 3D prestack depth migration algorithms. These issues were investigated, new methods devised and dedicated software tools were developed and implemented on the SPW seismic processing software to tackle them. This allowed obtaining an integrated solution for the processing of 3D OBS data, starting from the data acquisition up to the final pre-stack depth migration. The main objectives of this thesis were therefore achieved. Very accurate OBS positioning can be obtained with the new algorithm developed, without the need for additional shooting surveys for positioning before the start of seismic acquisition, thereby saving a large amount of ship time and energy. Artifacts related to the random drift of the internal clock of the OBS can be corrected using the new tool developed in the scope of this thesis using the SPW software, therefore saving valuable data. A new processing step was also created and implemented in SPW to interpolate the velocity functions into a regular grid, extrapolate the velocity field coverage from only covering the CMP grid to covering the full range of sources/receivers locations, and to smooth the velocity field without altering the velocity structure, so that migration artifacts are reduced. The calculation of travel-time tables for more efficient migration computation was implemented with multithreading capabilities for both 2D and 3D cases. The computational efficiency for both Paraxial ray-tracing and finite difference wave equation solver algorithms was also improved in this new implementation. A Kirchhoff pre-stack depth migration step, which makes use of the computed travel-time tables, was implemented to produce migrated gathers which are then stacked on CDP domain to produce the final subsurface images. This implementation is versatile in the way that it is capable of migrating OBS data as well as conventional streamer and land data, migrating P-P energy as well as P-S energy, and is implemented with multithreading capabilities to take full advantage of a large verity of hardware with multiple processing cores. All software was implemented in C++ with object-oriented coding and using QT libraries for the user interface so that it is platform independent and can be run on Windows, Unix/Linux, Mac-OS, or other supported systems.

6.2 Complete workflow for pre-stack depth migration of 3D Node data

In this Section, a complete workflow for processing OBS data, from the time data is recovered through the final delivery of the migrated images is presented and briefly discussed. Each step (or group of steps of similar type) is presented in a separate paragraph.

6.2.1. Quality control

Quality control is an essential step in the acquisition and processing of all types of seismic data regardless of whether it is for reflection or refraction work. Malfunctioning or miscalibrated hydrophones/geophones may generate records with very high level of noise. If such data is processed together with good data, this often results in degrading severely the quality of the final image. In the case of Node acquisition, quality control should be carried out specially to check for poor coupling of OBSs to the sea bottom. In such a case, the OBS unit will not correctly sense the ground motion, and this can be easily seen on the geophone component. If the OBS unit is on a rocky bed, as opposed to soft sandy beds, the underwater current may cause the instrument to "vibrate" throughout the acquisition. Again, data suffering coupling issues should be pre-processed separately to avoid any contamination of the rest of the data.

Quality analysis techniques used for OBS data are exactly the same as techniques used with conventional seismic data; most often we want to compare either RMS amplitudes or average amplitudes between records, frequency content, and signal to noise ratios.

6.2.2. Clock drift correction

Once quality control of the acquired data is carried out, it is important to check if the acquired data is suffering from clock drift issues. This step only requires source positions, which are normally in the headers of the seismic data (otherwise they have to be loaded to the headers before the checking), and first arrival picks. The details of the implemented process proposed here to correct for clock drift are found in chapter 3.

6.2.3. OBS Positioning

Until this stage, the position of each OBS units is not known or at best vaguely known. The OBS positioning step allows joint inversion of source positions and time of direct arrivals to

accurately compute the position of each OBS unit. Once this is completed, geometry can be assigned to the data. Chapter 4 explains the details of the improved positioning process developed in the scope of this thesis.

6.2.4. Geometry and Binning

In the case of 3D OBS data, the source locations and the receiver location are already defined; the CDP locations are defined in the depth migration as the imaging points. A 3D bin grid is defined as the areal extent of the velocity model and the migration imaging space.

6.2.5. Filtering, amplitude correction, and deconvolution

Although OBS data is generally less noisy when compared to conventional seismic, filtering is still required to enhance the recorded signal and remove any undesired energy. The main source of noise in OBS data is related to the coupling, which is receiver related. Therefore, it is ideal to run the filtering on each receiver record separately.

As the wavefield spreads it loses energy; the same amount of energy is spread out over a larger surface/volume, a process known as spherical divergence. While the wave propagates, it also loses energy as some of it scatters or reflects back at different interfaces. Also, some energy is converted to other types of seismic energy such shear waves, body waves or refractions, and other suffers absorption and is converted into heat and fracturing. Amplitude correction steps are designed to compensate for the loss of energy and equalize the amplitude content.

The seismic recorded data can be thought of as a convolution of the earth reflectivity model with the source and the receiver signatures. Deconvolution usually involves building an inverse filter to remove the effects of the source and the receiver and more precisely recover the earth reflectivity sequence. Deconvolution effectively compresses the source wavelet in the recorded seismogram, attenuates reverberations and short-period multiples, and balances frequencies. Resolution is thereby increased which yields a more interpretable seismic section.

6.2.6. Velocity analysis

Velocity analysis is extremely important for the processing of all seismic data. It is of utmost importance to the imaging process. A poorly estimated velocity model leads to bad travel-times (whether they are computed with DSR equation, ray tracing or finite difference) and bad amplitudes (equation 5.5) producing a distorted or incorrect image of the subsurface.

For OBS data, NMO-based and time migration velocity analysis are not possible because of the asymmetry of the ray path, but other options can be used. Previous knowledge of the surveyed area is often the starting point for building a simple velocity model. Refining of the velocity model may be done with refraction analysis, tomographic solutions, or full waveform inversion or some combination of methods. These methods can build a highly accurate interval velocity model of the subsurface. The other simpler method but less accurate is by running a wave equation re-datuming to get a more symmetric raypath followed by the NMO-based or time migration velocity analysis, which will build a fair representation of RMS velocities that can then be converted to interval velocities using the Dix equation.

6.2.7. Travel time computation and Migration

Travel time computation should be run on the interval velocity model as function of depth. It should be run for all source locations on the P-wave velocity model, then for all receiver locations on the P-wave velocity model for P-P migration, and on S-wave velocity model for P-S migration. In all cases, the input velocity model should be slightly smoothed for use with ray tracing and Kirchhoff depth migration methods. The details of this process can be found in chapter 5 (5.2 and 2.3).

6.2.8. Stacking and final image production

Once all receiver gathers are migrated, they should be stacked over CDP locations, which by now represent the reflection point instead of the midpoint. The stacked section/volume represents the final depth image of the subsurface.

6.3. Future work

As future work on this topic we suggest:

(1) Testing the new algorithms developed in the scope of this thesis on a full 3D Node dataset released for this purpose by industry and further improve computational efficiency to handle large seismic datasets.

(2) Comparing the positioning results delivered by the multilateration method proposed here with the accurate positioning returned from ROV deployment and USBL systems, in order to further assess the method's accuracy and estimate associated uncertainties.

(3) Investigating the differences that may arise in the computation of the OBS depth values if RMS, median, or weighted average values are used instead of the standard average, and perform a statistical analysis of those variations.

(4) As concerns migration and migration-related algorithms, three main issues deserve further investigation: 1) restricting of travel-time tables by offset so as to reduce the associated file size; 2) the implementation of appropriate amplitude weighing functions for shear wave imaging since the current functions are more appropriate for pressure waves; 3) the development of an "interval depth velocity analysis tool" for both Vp and Vs.

References:

Abma R, Sun J, Bernitsas N (1999) Antialiasing methods in Kirchhoff migration. Geophysics 64:1783–1792.

Ao W, Zhao M-H, Qiu X-L, et al. (2010) The Correction of Shot and OBS Position in the 3D Seismic Experiment of the SW Indian Ocean Ridge. Chinese J Geophys 53:1072–1081. doi: 10.1002/cjg2.1577.

Bancroft, J. C. 2013 - Practical Understanding of Pre- and Post-Stack Migration: course manual. SEG Annual Meeting in Houston, TX.

Barr FJ, Sanders JI (1989) Attenuation of water-column reverberations using pressure and velocity detectors in a water-bottom cable. SEG Tech Progr Expand Abstr 1989 6:653–656. doi: 10.1190/1.1889557.

Ben-menahem A, Beydoun WB (1985) Range of validity of seismic ray and beam methods in general inhomogeneous media - General theory. Geophys J R Astron Soc 207–234.

Bevc D, Lumley D (2001) When is anti-aliasing needed in Kirchhoff migration ? Stanford Explor Proj Rep 80:1–9.

Beydoun WB, Keho TH (1987) The paraxial ray method. Geophysics 52:1639–1653.

Bouska J (2008) Advantages of wide-patch, wide-azimuth ocean-bottom seismic reservoir surveillance. Lead Edge 1662–1681.

Bucha V (2004) Ray tracing computations in the smoothed SEG / EAGE Salt Model. SEG Tech Progr Expand Abstr 1861–1864. doi: 10.1190/1.1845179.

Cerveny V (2001) Seismic ray theory. Cambridge University Press.

Cerveny V, Klimes L, Psencik I (1984) Paraxial ray approximations in the computation of seismic wavefields in inhomogeneous media. Geophys J R Astron Soc 89–104.

De Kok R (2012) Directions in ocean-bottom surveying. Lead Edge 415–427.

Dellinger JA, Gray SH, Murphy GE, Etgen JT (2000) Efficient 2.5-D true-amplitude migration. Geophysics 65:943–950. doi: 10.1190/1.1444790.

Domingo-perez F, Lazaro-galilea JL, Wieser A, et al. (2016) Sensor placement determination for range-difference positioning using evolutionary multi-objective optimization. Expert Syst Appl 47:95–105. doi: 10.1016/j.eswa.2015.11.008.

Etgen J, Gray SH, Zhang Y (2009) An overview of depth imaging in exploration geophysics. 74:WCA5–WCA17.

Flude JW (1942) Method and apparatus for subsurface mining. 1–6.

Gardner AT, Collins J a. (2012) Advancements in high-performance timing for long term underwater experiments: A comparison of chip scale atomic clocks to traditional microprocessor-compensated crystal oscillators. Ocean 2012 MTS/IEEE Harnessing Power Ocean. doi: 10.1109/OCEANS.2012.6404847.

Gazdag J (1978) Wave equation migration with the phase-shift method. Geophysics 13:1342–1351.

Gouédard P, Seher T, McGuire JJ, et al. (2014) Correction of ocean-bottom seismometer instrumental clock errors using ambient seismic noise. Bull Seismol Soc Am 104:1276–1288. doi: 10.1785/0120130157.

Gray SH (1986) Efficient traveltime calculations for Kirchhoff migration. Geophysics 51:1685–1688.

Gray SH, Etgen J, Dellinger J, Whitmore D (2001) Seismic migration problems and solutions. Geophysics 66:1622–1640. doi: 10.1190/1.1487107.

Gray SH, Marfurt KJ (1995) Migration from topography: improving the near-surface image. Can J Explor Geophys 31:18–24.

Haibo Z, Wubao F, Penggui J (2009) Prestack time migration from rugged surface topography. Beijing 2009 Int Geophys Conf Expo Beijing, China 225–225. doi: 10.1190/1.3603750.

Haines SS, Hart PE, Ruppel CD, et al. (2014) Cruise Report for P1 – 13 – LA , U . S . Geological Survey Gas Hydrates Research Cruise , R / V Pelican April 18 to May 3 , 2013 , Deepwater Gulf of Mexico. doi: 10.3133/ofr20141080

Imtiaz A, Nguyen B, Roberts M (2013) Joint inversion for ocean bottom node position and average water velocity along the shot line. 93rd Int. Expo. Annu. Meet. SEG. Houston, pp 4880–4884.

Jäger C, Hertweck T, Spinner M (2003) True-amplitude Kirchhoff migration from topography. 73th Int Expo Annu Meet SEG 909–912. doi: 10.1190/1.1818089.

Julian BR, Gubbins D (1977) Three dimentional seismic ray tracing. J Geophys 43:95–113.

Keho TH, Beydoun WB (1988) Paraxial ray Kirchhoff migration. 53:1540–1546.

Lamer KL, Hattom L, Gibson BS, Hsuej I (1981) Depth migration of imaged time sections. Geophysics 46:734–750. doi: 10.1190/1.1441212.

Lee S, King D, Lin S (2004) Efficient true-amplitude weights in Kirchhoff time migration. SEG Tech Progr Expand Abstr 1089–1092.

Leontovich MA, Fock LA (1946) Solution of the problem of propagation of electromagnetic waves along the earth's surface by the method of parabolic equation. J Phys USSR 10:13.

Liu Z, Bleistein N (1991) Velocity Analysis by Inversion. SEG Tech Progr Expand Abstr 1991 1230–1233. doi: 10.1190/1.1888709.

Lumley DE, Claerbout JF, Bevc D (1994) Anti-aliased Kirchhoff 3-D migration. SEG Tech Progr Expand Abstr. doi: 10.1190/1.1822760.

Mantilla Gaviria IA, Leonardi M, Balbastre-Tejedor J V., de los Reyes E (2013) On the application of singular value decomposition and Tikhonov regularization to ill-posed problems in hyperbolic passive location. Math Comput Model 57:1999–2008. doi: 10.1016/j.mcm.2012.03.004.

Mànuel A, Roset X, Del Rio J, et al. (2012) Ocean bottom seismometer: design and test of a measurement system for marine seismology. Sensors (Basel) 12:3693–719. doi: 10.3390/s120303693.

Moulin M, Klingelhoefer F, Afilhado A, et al. (2015) Deep crustal structure across a young passive margin from wide-angle and reflection seismic data (The SARDINIA Experiment) – I . Gulf of Lion ' s margin. Bull la Société Géologique Fr 186:309–

330. doi: 10.2113/gssgfbull.186.4-5.309.

Nowack RL (1992) Wavefronts and solutions of the eikonal equation. Geophys J Int 110:55–62.

Nowack RL, Aki K (1984) The two-dimensional Gaussian beam synthetic method: Testing and application. J Geophys Res 89:7797–7819. doi: 10.1029/JB089iB09p07797.

Oshida A, Kubota R, Nishiyama E, et al. (2008) A new method for determining OBS positions for crustal structure studies, using airgun shots and precise bathymetric data. Explor Geophys 39:15–25. doi: 10.1071/EG08005.

Panahi Shariat S, Alegria FC, Làzaro M, Rio J (2009) Time Drift of Ocean Bottom Seismometers (Obs). 2548–2553.

Panahi Shariat S, Manuel A, Ventosa S (2006) Stability and power consumption tests for time base selection of an Ocean Bottom Seismometer (OBS). Midwest Symp Circuits Syst 2:323–326. doi: 10.1109/MWSCAS.2006.382277.

Pedersen O, Ursin B, Helgesen H (2010) One-way wave-equation migration of compressional and converted waves in a VTI medium. Geophysics 75:237–248. doi: doi: 10.1190/1.3509466.

Podvin P, Lecomte I (1991) Finite difference computation of traveltimes in very contrasted velocity models : a massively parallel approach and its associated. Geophys J Int 105:271–284.

Qin F, Olsen KB, Luo Y, Schuster GT (1990) Solution of the Eikonal Equation by a Finite-Difference Method. SEG Tech Progr Expand Abstr 1990 1004–1007.

Sava P, Fomel S (1998) Huygens wavefront tracing : A robust alternative to ray tracing. SEG Tech Progr Expand Abstr 1961–1964. doi: 10.1190/1.1820324.

Robinson, E. A. (1983) Migration of geophysical data. Springer. p 208. ISBN: 0934634149.

Shiobara H, Nakanishi A, Shimamura H, et al. (1997) Precise Positioning of Ocean Bottom Seismometer by Using Acoustic Transponder and CTD. Mar Geophys Res 19:199–209. doi: 10.1023/A:1004246012551.

Schneider W a. (1978) Integral Formulation for Migration in Two and Three Dimensions. Geophysics 43:49. doi: 10.1190/1.1440828.

Thinon I, Matias L, Rehault J., et al. (2003) Deep structure of the Armorican Basin (Bay of Biscay): a review of Norgasis seismic reflection and refraction data. Bull la Société Géologique Fr 99–116. doi: 10.1144/0016-764901-103.

Thornburgh HR (1930) Wave-Front Diagrams in Seismic Interpretation. AAPG Bull 14:185–200.

Vetterling WT, Teukolsky SA, Flannery BP, Press WH (2002) Numerical Recipes in C The Art of Scientific Computing. Cambridge university Press.

Vidale JE (1988) Finite-difference calculation of travel times. Bull Seismol Soc Am 78:2062–2076.

Vidale JE (1990) three dimensions. Geophysics 55:521–526.

Vidale JE, Houston H (1990) Rapid calculation of seismic amplitudes. Geophysics 55:1504–1507.

Xu S, Lambar G, Noble M (2001) Common-angle migration : A strategy for imaging complex media. Geophysics 66:1877–1894.

Zhang Y, Gray S, Young J (2000) Exact and approximate weights for Kirchhoff migration. SEG Tech Progr Expand Abstr 1036–1039. doi: doi: 10.1190/1.1815561.

Zhenyue L (1993a) A Kirchhoff Approach to Seismic Modeling and Prestack Depth Migration. SEG Tech Progr Expand Abstr 888–891.

Zhenyue L (1993b) A Velocity Smoothing Technique Based on Damped Least Squares. CWP.